1970

Investigation of isobaric spin splitting in the giant resonance of zinc 64

Frederick Herold Schamber
Iowa State University

INVESTIGATION OF ISOBARIC SPIN SPLITTING IN THE GIANT RESONANCE OF ZINC 64

by

Frederick Herold Schamber

A Dissertation Submitted to the
Graduate Faculty in Partial Fulfillment of
The Requirements for the Degree of
DOCTOR OF PHILOSOPHY

Major Subject: Physics

Approved:

Signature was redacted for privacy.

In Charge of Major Work

Signature was redacted for privacy.

Head of Major Department

Signature was redacted for privacy.

Dean of Graduate College

Iowa State University
Of Science and Technology
Ames, Iowa

1970

PLEASE NOTE:

Some pages have small
and indistinct type.
Filmed as received.

University Microfilms

February 19, 1970

I hereby request that the changes listed below which I desire to make in the manuscript copy of the thesis submitted for the degree Doctor of Philosophy be approved.

Signature was redacted for privacy.

The abbreviations mev, mv, and kev appearing in the text of the thesis do not conform to the accepted conventions. These abbreviations should be written MeV, mV, and keV.

Approved:

Signature was redacted for privacy.
In Charge of Major Work

Signature was redacted for privacy.
Head of Major Department

Signature was redacted for privacy.
Dean of Graduate College

TABLE OF CONTENTS

CHAPTER I. INTRODUCTION

The giant resonance is a universal feature of all known photo-absorption cross sections. In poor resolution, the cross section for photon absorption in any nucleus is dominated by a single broad resonance with peak energy of roughly 20 mev for light nuclei and decreasing to about 10 mev for heavier nuclei. The main features of this resonance have been explained in terms of electric-dipole (E1) excitation of single nucleons between major shells. In view of the predominately single particle nature of the giant resonance excitation, the question of isobaric spin is clearly significant. Since neutrons and protons are distinguishable, on the one hand, the excitations involving neutrons and protons can be considered to be fundamentally different. On the other hand, if the coulomb interaction does not mix states significantly and since the nuclear potential is essentially charge independent, one need only speak of the excitation of a nucleon with isobaric spin t = 1/2 (projection t_z = 1/2 for a neutron and t_z = -1/2 for a proton), and the excitation is characterized by the isobaric spin quantum number of the excited configuration. The problem then is to determine which picture is most productive -- neutron and proton excitations, or excitation to configurations of definite isobaric spin. Since the total nuclear potential involves coulomb repulsion for protons and is therefore not completely charge independent, isobaric spin may not be a useful quantum number. The significant question then is the degree to which the giant resonance states can be characterized as pure isobaric spin configurations.

Although the formalism of isobaric spin (also known as isotopic spin,

or simply isospin) was set forth as early as 1937 (1) and was successfully applied to light nuclei ($A \lesssim 20$), it was generally conceded that the large coulomb potential for medium and heavy nuclei would result in sufficient configuration mixing to destroy the isobaric spin identity of excited levels.

It thus came as somewhat of a surprise when isobaric analog resonances were identified in 1961 in (p,n) reactions for nuclei as heavy as mass 93 (2). (In the isobaric spin terminology, levels of the same total isobaric spin T but different projection T_z in nuclei of the same atomic mass A, are said to be isobaric analogs. Such levels are members of an isospin multiplet and have identical spin, parity, and relative energy displacement, but will be displaced upwards by the coulomb displacement energy E_c in the "daughter" nucleus, with respect to the parent nucleus.) These results indicated that isobaric spin might indeed be a good quantum number for all nuclei and this notion has been confirmed for a large variety of nuclear excitations.

The situation that today exists is that the isobaric spin interpretation has become standard for a wide variety of nuclear phenomena, the study of isobaric analog resonances in particular being an accepted technique for inferring the level structure of otherwise inaccessible nuclei. In the case of photonuclear reactions, however, the applicability of the isobaric spin formalism has not been firmly established.

Isospin Selection Rules

It is well known that the electric dipole (E1) operator can only connect states differing by 0 or 1 unit of isobaric spin (but $0 \rightarrow 0$ is forbidden) (3). It is observed that the ground state of all nuclei have

$T_o = T_z$ (T_z = 1/2 (N-Z)) and dipole excitations are therefore restricted to population of levels for which $T = T_o$, $T_o + 1$. As observed by Fallieros, Goulard, and Venter (4), the giant resonance should then be split into two components, $T_< = T_o$ and $T_> = T_o + 1$ for all nuclei with ground state isospin $T_o \neq 0$, the latter component lying higher in energy.

Decay from the isospin components of the giant resonance must also obey the isospin selection rules; in particular, neutron or proton decay from levels with isospin T is allowed only to levels with isospin $T \pm 1/2$. Gamma decay may again proceed to levels with isospin = $T \pm 1$ (but $0 \rightarrow 0$ forbidden for E1 transitions).

When applied to the decay of the giant resonance levels, the isospin selection rules provide an experimental means of identifying the $T_<$ and $T_>$ giant resonance components. Figure 1 illustrates the application of the selection rules to a typical medium or heavy nucleus with $N \neq Z$; the relative spacing and position of the levels may vary considerably for a specific nucleus, but the situation indicated is illustrative of the important features. The centroids of the $T_<$ and $T_>$ resonances are indicated by cross-hatched regions -- the following discussion shall be limited to the effects of the energetic thresholds and isospin selection rules governing the decays of both components without consideration of the energy distribution of the two giant resonance components.

Below the (γ,p) threshold (e_1 region) no particle emitting reactions are possible, but above this threshold, either component can decay to the low lying $T_o + 1/2$ levels of the (Z - 1,N) residual nucleus. Just above the (γ,n) threshold (region e_3) neutron decay to the low lying $T_o - 1/2$ levels of the (Z,N - 1) residual nucleus is isospin allowed from the $T_<$

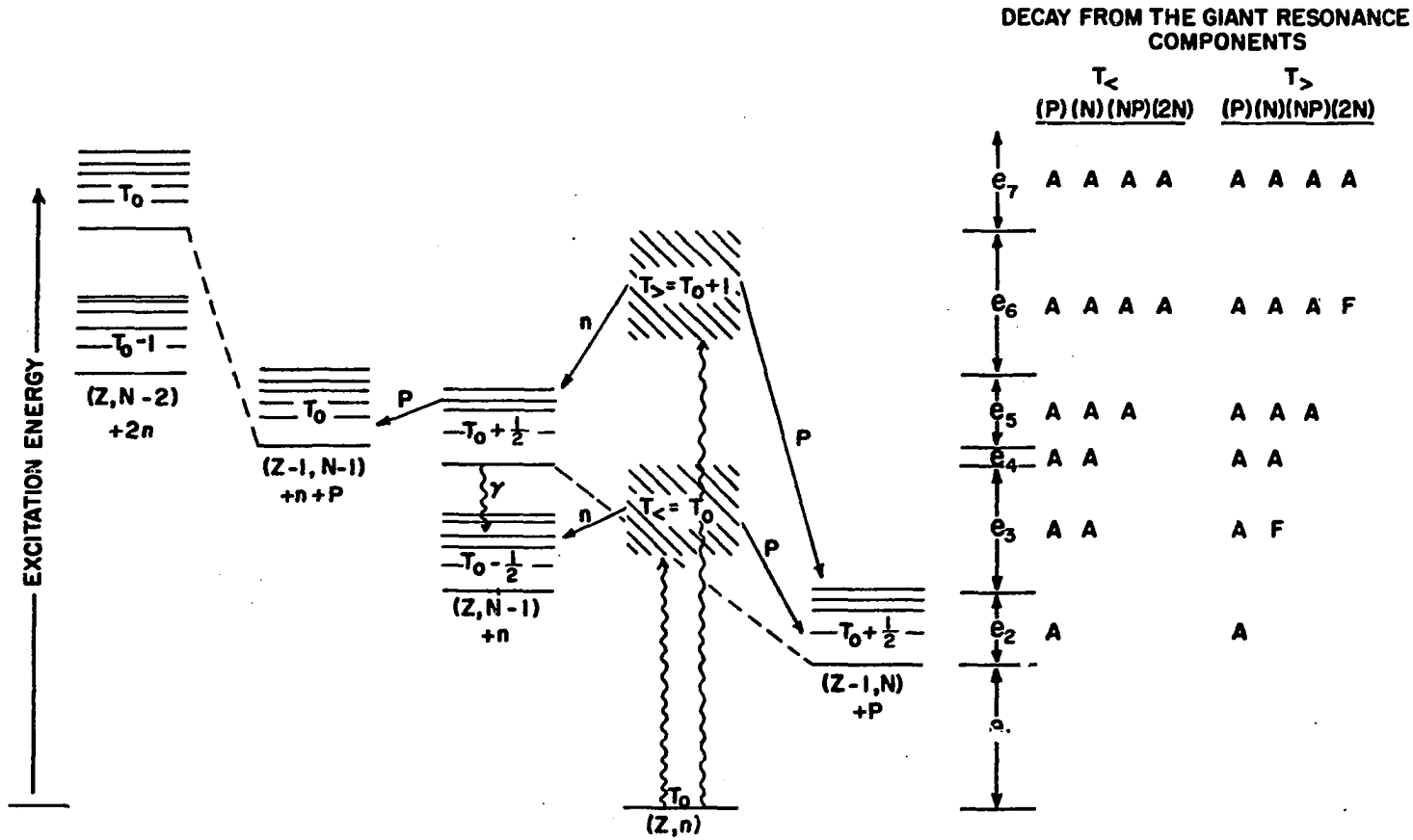

Figure 1. Application of isospin selection rules to a typical nucleus with ground state isospin T_o. e_1 to e_7 indicate the energy regions of interest. Energetically possible reactions are identified as A (isospin allowed) or F (isospin forbidden). Arrows indicate some of the isospin allowed decay processes. Isobaric analog levels are connected by broken lines. The predicted centroids of the giant resonance isospin components are indicated as cross-hatched regions.

component, but isospin forbidden from the $T_>$ component. Isospin allowed neutron decay from the $T_>$ component is not possible until the $T_o + 1/2$ excited levels in the neutron-residual nucleus become energetically available (regions e_4 to e_7); these levels are isobaric analogs of the $T_o + 1/2$ low lying levels of the proton-residual nucleus. For a typical medium weight nucleus, many or all of these analog levels are particle unstable (5), thus, as indicated in Figure 1, subsequent proton decay becomes energetically possible in region e_5 (above the (γ,np) threshold) and neutron decay in region e_6 (above the $(\gamma,2n)$ threshold). The low lying levels of the $(Z - 1, N - 1)$ nucleus have isospin = T_o and proton decay from the $T_o + 1/2$ excited levels is thus isospin allowed, however, neutron decay to the $T_o - 1$ low lying levels of the $(Z,N - 2)$ nucleus is isospin forbidden. In region e_7 the excited isospin = T_o levels become energetically available (analogs of the low lying levels in the $(Z - 1, N - 1)$ nucleus) and the $(\gamma,2n)$ reaction is then isospin allowed.

The point to be recognized in the above discussion is that there are energetic regions where the (γ,n) and $(\gamma,2n)$ reactions are isospin forbidden for the $T_>$ resonance. Thus one expects the (γ,p) or (γ,np) reactions to dominate the $T_>$ cross section in these regions. When the $T_>$ levels are largely concentrated in one of these regions, the isospin selection rules require that it proceed through the (γ,p) or (γ,np) reactions. Since no such restriction holds for the $T_<$ levels, this component should be seen primarily in the reactions favored by the coulomb barrier, namely the (γ,n) and $(\gamma,2n)$ reactions. Other reactions, such as $(\gamma,2p)$, $(\gamma,p2n)$, and (γ,α) are of course possible but due to the coulomb barrier are not expected to be sizeable.

Previous Experimental Investigations

The ratio of (γ,n) and (γ,p) strengths in self-conjugate nuclei is a sensitive measure of the isobaric spin purity of the giant resonance excitation (5). The comparison has limited applicability since Ca^{40} is the heaviest stable self-conjugate nucleus. A further difficulty in comparison of such strengths is that the cross sections are never measured simultaneously, and small differences in the absolute calibration of the results can obscure the interpretation of such ratios. Furthermore, although the measured ratios are generally consistent with relatively small isotopic spin impurity, it is difficult to take into account the many other factors (coulomb barrier, relative (γ,n) and (γ,p) thresholds, availability of levels in the residual nucleus, etc.) which affect the (γ,n) and (γ,p) strengths and it is thus not possible to conclusively ascribe the observed results to the validity of the isospin selection rules.

Experimental verification of the giant resonance splitting predicted for non-self-conjugate nuclei would constitute compelling evidence of the role of the isospin selection rules in the nuclear photoeffect. Most attempts to establish the existence of the $T_>$ component have been concerned with the single-proton channel. The motivation is that since the $T_>$ component is isospin allowed through this channel whereas the single-neutron channel is isospin forbidden, the $T_>$ component should manifest itself as a sizeable resonance in the (γ,p) or (p,γ_o) cross section.

Some of the efforts along this line have involved the comparison of (γ,p) and (γ,n) cross sections from earlier experiments (5,6). Such comparisons are not always meaningful however, since the available

measurements vary widely in absolute normalization, energy calibration, and resolution. Although such comparisons are interesting, the interpretational difficulties make it dangerous to draw definite conclusions.

Several attempts have been made to directly measure the $T_>$ component of the giant resonance of the (γ,p) and (p,γ_o) reactions. Axel et al. (7) observed a sharp resonance in the $Y^{89}(p,\gamma_o)$ cross section about 5 mev above the (γ,n) giant resonance, in good agreement with Fallieros prediction of the energy splitting (4). However, the strength of the resonance is much less than that predicted for the $T_>$ component. Shoda et al. (8) have measured the (γ,p_o) reaction for Sr^{88} and Zr^{90}. Again distinct resonances at 4-5 mev excitation above the (γ,n) giant resonance were observed, however, the strengths were again found to be less than predicted. The observation of definite resonances at the proper energies is encouraging, but it is disturbing that the measured cross section strengths are not in better agreement with predicted strengths.

A possible explanation for the lack of strength in the proton channel for these experiments is found when other isospin allowed channels are available. In particular, when the excited $T_o \pm 1/2$ levels in the neutron residual nucleus are available (region e_4 of Figure 1), a significant fraction of the $T_>$ strength can be expected to proceed through these levels. If these levels are particle stable, as for the lowest $T_o + 1/2$ level in Figure 1, they will then decay by gamma emission and the process is seen as an isospin allowed (γ,n) reaction. In the Zr^{90} case there is, in fact, seen to be a shoulder in the (γ,n) cross section above the major giant resonance peak (9,10) and this might account for some of the missing strength in the proton channel.

A recent measurement by Gellie (11) is very interesting in this respect. Gellie measured the (γ,n) cross section in Mo^{92} and observed a definite satellite resonance at about 3-5 mev excitation above the major resonance which he interprets as being due to isospin allowed neutron decay to the T = 9/2 levels in Mo^{91}. Credence is given to this interpretation by the fact that the (γ,n) + (γ,p) cross section for Mo^{100} (also measured by Gellie) indicates a satellite resonance at roughly the proper excitation, and this satellite is not seen in an earlier (γ,n) measurement with which he compares his result. Since the T = 9/2 levels are energetically available in Mo^{91} but the T = 17/2 levels in Mo^{99} are inaccessible, the respective (γ,n) and (γ,p) channels would indeed be expected to dominate the $T_>$ decay of these nuclei. The relative strength of the satellite peak can only be inferred by subtraction of the earlier measurement in the case of the Mo^{100} measurement and extrapolation of the "tail" of the major resonance peak in the Mo^{92} case, so this identification is suggestive but not conclusive.

The present status of the investigation of the photonuclear isospin effect can thus be briefly summarized: There have been a small number of experiments from which the existence of the $T_>$ component can be inferred on the basis of energy splitting in reasonable agreement with predicted values, but in none of these cases has the predicted strength of this resonance been unambiguously observed. It is encouraging to note that the results are consistent with an isobaric spin explanation (with suitable interpretation) but the overall evidence for photonuclear isobaric spin splitting in medium and heavy nuclei must still be regarded as tenuous.

The np Channel

For many medium heavy nuclei, the (γ,np) reaction is particularly interesting as a means of investigating the $T_>$ giant resonance component. As mentioned earlier in this chapter, for excitation energies between the (γ,np) threshold (or the occurrence of the $T_o + 1/2$ analog levels in the neutron-residual nucleus, whichever is higher) and the occurrence of the T_o levels in the $(Z,N - 2)$ nucleus (region e_6 of Figure 1) the $T_>$ (γ,np) process is isospin allowed and the $T_>(\gamma,2n)$ process is isospin forbidden. Not only is the (γ,np) reaction allowed for this component, but it can be expected to account for a sizeable fraction of the $T_>$ strength; since neutron decays are favored by the coulomb barrier, the $T_o + 1/2$ levels of the $(Z,N - 1)$ nucleus should be highly populated, then since particle emission is strongly favored over gamma emission these levels should decay almost exclusively by proton emission. When the energy levels are favorable (eg. the $T_>$ levels are primarily concentrated in region e_6 of Figure 1), the $T_>$ component should proceed primarily by the (γ,np) reaction.

Another important reason for considering the np channel is that it is generally not populated strongly by the $T_<$ component -- in most cases, the major part of the giant resonance ($T_<$ component) lies below the (γ,np) threshold. Thus, a resonance in the (γ,np) cross section is a first-order effect, whereas, the $T_>$ resonance is built on the tail of the $T_<$ resonance when observed by the (γ,n) and (γ,p) reactions.

Finally, it is to be noted and strongly emphasized, that the observed ratio of the $(\gamma,2n)/(\gamma,np)$ cross sections is a sensitive test of the reaction mechanism responsible for the (γ,np) cross section. This statement is justified by the following consideration: any reaction mechanism

which does not differentiate between neutrons and protons (or states of different isospin) should result in roughly equivalent (γ,np) and (γ,2n) strength. If anything, the (γ,2n) reaction is expected to dominate in a "statistical" model since the coulomb barrier retards proton emission. If, however, the (γ,np) cross section is observed to be significantly larger than the (γ,2n) cross section, it can be clearly inferred that the reaction mechanism is charge sensitive in a fundamental way. A charge sensitive reaction does not automatically imply isospin selectivity, but it does rule out statistical "evaporation" processes.

For the above reasons, the (γ,np) channel, which has not previously been systematically studied as an isospin sensitive reaction, shall in this experiment be examined for a medium weight nucleus. The actual measurement involves the simultaneous measurement of the (γ,n), (γ,np), and (γ,2n) reactions in Zn^{64}. In Chapter II, using recently published sum-rules, the quantitative features of the $T_>$ giant resonance are estimated for the Zn^{64} nucleus. Chapter III is devoted to experimental details of the yield curve measurements and Chapter IV treats the unfolding of the yield curves and discusses the resulting cross section curves. In Chapter V, the experimental results are compared with the isospin predictions and it is concluded that there is compelling evidence of isospin splitting of the giant resonance in this medium weight nucleus.

CHAPTER II. ISOSPIN SPLITTING OF THE ZN^{64} GIANT RESONANCE

Before proceeding to the application of the isospin selection rules to a specific nucleus, it is necessary to develop expressions from which the giant resonance component strengths and energy splitting can be estimated.

Quantitative Features of Isospin Splitting

The nuclear electric dipole (E1) operator is considered in the long wavelength approximation (photon polarization along the x axis)

$$D = e \sum_{i=1}^{Z} x_i = \sum_{i=1}^{A} q_i x_i \qquad (II.1)$$

where q_i is the charge operator, having eigenvalue 0 for neutrons and +e for protons. In isospin notation, this operator can be written as $q_i = (e/2)(1-T_{zi})$ where T_{zi} is the z component isospin matrix of the single particle isospin operator $\vec{T}_i$ and has eigenvalues +1 for neutrons and -1 for protons. Then

$$D = \sum_{i=1}^{A} (e/2)(1-T_{zi})x_i \quad . \qquad (II.2)$$

The first term corresponds to center of mass motion (Thomson scattering) and is irrelevant for the consideration of nuclear excitation. The second term is just the nuclear operator which generates E1 excitations and is the operator of interest. The cross section for E1 photon absorption resulting in transitions from isospin state T_a to state T_b is then

$$\sigma(T_a \rightarrow T_b, T_z) = \frac{4\pi^2 e^2}{\hbar c} \left| M_{ab} \right|^2 \qquad (II.3)$$

where

$$M_{ab} = \langle T_b, T_z | D | T_a, T_z \rangle = \text{the transition matrix element} \qquad (11.4)$$

and

$$D = -1/2 \sum_{i=1}^{A} T_{z\,i} x_i \qquad (11.5)$$

Since the electric dipole operator is a spherical tensor of rank 1 in isospin space, one then applies the Wigner-Eckart theorem to obtain

$$M_{ab} = (-)^{T_b - T_z} \begin{pmatrix} T_b & 1 & T_a \\ -T_z & 0 & T_z \end{pmatrix} \langle T_b \| D \| T_a \rangle \ . \qquad (11.6)$$

The reduced matrix element $\langle T_b \| D \| T_a \rangle$ does not involve T_z, all T_z dependence is now contained in the "3j" symbol.

The situation of interest is for excitation from the ground state for which $T_a = T_0 = 1/2(N-Z)$ to an excited state, then

$$\sigma(T_o \to T_o - 1, T_o) = 0 \qquad (11.7a)$$

$$\sigma(T_o \to T_o, T_o) = \left(\frac{T_o}{T_o + 1}\right) 4\pi^2 \alpha \left| \langle T_o \| D \| T_o \rangle \right|^2 \qquad (11.7b)$$

$$\sigma(T_o \to T_o + 1, T_o) = \left(\frac{1}{T_o + 1}\right) 4\pi^2 \alpha \left| \langle T_o + 1 \| D \| T_o \rangle \right|^2 \qquad (11.7c)$$

the latter two of which are the cross sections for the giant resonance $T_< = T_o$ and $T_> = T_o + 1$ components respectively. The ratio of the strengths is then

$$\frac{\sigma(T_o \to T_o + 1)}{\sigma(T_o \to T_o)} = (1/T_o) \frac{\left| \langle T_o + 1 \| D \| T_o \rangle \right|^2}{\left| \langle T_o \| D \| T_o \rangle \right|^2} \qquad (11.8)$$

and it is seen that the partition of the physical cross section is determined by the purely geometrical factor $1/T_o$, and a dynamic factor involving the reduced matrix elements. The geometrical factor alone indicates a good deal about the expected trend of $T_<$ and $T_>$ strengths; considering only the geometrical factor we anticipate that for $T_o = 0$ nuclei (self-conjugate nuclei) the $T_>$ component is everything; for $T_o = 1/2$ (e.g. C.13) the $T_>$ component is larger than the $T_<$ component; as the neutron excess increases the $T_>$ component decreases (for Pb^{208}, $1/T_o = 1/22 \cong 5\%$). This is not the whole story, however, since the dynamic factor is also important. This latter factor is model dependent and must be calculated for the specific nuclear situation.

Note that for $T_o = 0$ equation II.7b gives $\sigma(0 \to 0) = 0$ even though the matrix element is in general non-zero. This is the origin of the selection rule that forbids $0 \to 0$ transitions. The more general rule $\Delta T = 0, \pm 1$ holds for transitions of all multipolarities (3) and thus holds even if other transitions (e.g. M1 and E2) are involved in the giant resonance excitation.

Energy splitting

The average resonance energy is found from

$$\bar{E} = \frac{\int \sigma(\omega)\, d\omega}{\int \sigma(\omega)/\omega \; d\omega} = \frac{\sigma_{int}}{\sigma_{-1}} \qquad (11.9)$$

where σ_{-1} is the inverse-energy-weighted or "bremsstrahlung weighted" cross section, and σ_{int} is the usual integrated cross section.

In a recent article by Leonardi and Rosa-Clot (12) there is outlined a method by which these cross sections can be simply related to nuclear model calculations for given isospin. Leonardi and Rosa-Clot separate the

total bremsstrahlung weighted cross section into isoscalar, isovector, and isotensor parts, thereby obtaining expressions for the isoscalar, isovector, and isotensor radii ($\alpha = \frac{e^2}{\hbar c}$)

$$\frac{1}{3}r_s^2 = \frac{1}{(2\alpha\pi^2)} \int \frac{d\omega}{\omega} J \tag{11.10a}$$

$$\frac{1}{3}r_v^2 = \frac{1}{(2\alpha\pi^2)} \int \frac{d\omega}{\omega} L \tag{11.10b}$$

$$\frac{1}{3}r_t^2 = \frac{1}{(2\alpha\pi^2)} \int \frac{d\omega}{\omega} N \tag{11.10c}$$

where J, L, and N are linear combinations of the reduced cross sections

$$J = \frac{2T+3}{3(2T+1)}\sigma_{T+1} + \frac{1}{3}\sigma_T + \frac{2T-1}{3(2T+1)}\sigma_{T-1} \tag{11.11a}$$

$$L = -\frac{2T+3}{3(2T+1)(T+1)}\sigma_{T+1} + \frac{1}{2T(T+1)}\sigma_T + \frac{2T-1}{2T(2T+1)}\sigma_{T-1} \tag{11.11b}$$

$$N = -\frac{1}{2(2T+1)(T+1)}\sigma_{T+1} + \frac{1}{2T(T+1)}\sigma_T - \frac{1}{2T(2T+1)}\sigma_{T-1} \tag{11.11c}$$

The reduced cross sections σ_{T+1}, σ_T, σ_{T-1} appearing in equations 11.11 are defined by

$$\sigma_{T+\Delta T} = 4\pi^2\alpha\left|\langle T+\Delta T \| D \| T\rangle\right|^2 \tag{11.12}$$

and by comparison with equations 11.7, the physical cross sections

$$\sigma(T_o \to T_o, T_o) = \frac{T_o}{T_o+1}\sigma_{T_o} \tag{11.13a}$$

$$\sigma(T_o \to T_o+1, T_o) = \frac{1}{T_o+1}\sigma_{T_o+1} \tag{11.13b}$$

are defined in terms of the reduced cross sections. Note that σ_{T-1} is not observable from dipole excitation. r_s, r_v, and r_t are known as the isoscalar, isovector, and isotensor radii respectively and are defined by

$$r_s^2 = 3/2 \left\langle T, T_z \left| \sum_{ij} x_i x_j \, (\vec{T}_i \cdot \vec{T}_j) \right| T, T_z \right\rangle \tag{11.14a}$$

$$r_v^2 = \frac{3}{2T_z} \left\langle T, T_z \left| \sum_i x_i^2 \, T_{zi} \right| T, T_z \right\rangle \tag{11.14b}$$

$$r_t^2 = \frac{3}{2T_z^2 - \frac{2}{3}(T+1)T} \left\langle T, T_z \left| \sum_{ij} x_i x_j \, \frac{1}{4} [T_{zi} T_{zj} + T_{zj} T_{zi} - \frac{2}{3} (\vec{T}_i \cdot \vec{T}_j)] \right| T, T_z \right\rangle . \tag{11.14c}$$

Eliminating σ_{T-1} from equations 11.11a,b, and c one obtains the forms

$$\sigma_T - \sigma_{T+1} = (T+1)[(2T-1)N + L] \tag{11.15a}$$

$$T\sigma_T + (2T+3)\sigma_{T+1} = - (T+1)[2TL - 3J] \tag{11.15b}$$

and finally

$$\sigma_T = \frac{1}{3}(2T+3)(2T-1)N + J + L \tag{11.16a}$$

$$\sigma_{T+1} = J - TL - \frac{T}{3}(2T-1)N \quad . \tag{11.16b}$$

By application of the relations for the physical cross sections, (equations 11.13) and using the definitions of equations 11.10, one obtains expressions for the $T_<$ and $T_>$ bremsstrahlung weighted cross sections in terms of the isoscaler, isovector, and isotensor radii.

Leonardi and Rosa-Clot also derive the relations

$$A_s = \frac{1}{2\pi^2\alpha}\int J d\omega \tag{11.17a}$$

$$A_v = \frac{1}{2\pi^2\alpha}\int L d\omega \tag{11.17b}$$

$$A_t = \frac{1}{2\pi^2\alpha}\int N d\omega \tag{11.17c}$$

which are isoscalar, isovector, and isotensor expectation values defined in terms of the [H,D] commutators and anticommutators. Using equations 11.13, 11.16, and 11.17 the $T_<$ and $T_>$ integrated cross sections are then also defined. (The above notation is that of Leonardi and Rosa-Clot (12).)

One then obtains, using the identity of equation 11.9

$$\bar{E}_T = \frac{3[A_s + A_v + 1/3(2T+3)(2T-1)A_t]}{r_s^2 + r_v^2 + \frac{1}{3}(2T+3)(2T-1)r_t^2} \tag{11.18a}$$

$$\bar{E}_{T+1} = \frac{3[A_s - TA_v - T/3(2T-1)A_T]}{r_s^2 - Tr_v^2 - \frac{T}{3}(2T-1)r_t^2} \tag{11.18b}$$

for the mean component energies. The isotensor terms r_t and A_t drop out when $T = 1/2$, but must be considered for all other $T \neq 1/2$. It can be shown that $r_t = 0$ if there is no correlation between excess neutron pairs; in other words, $r_t = 0$ for an independent particle model (6). In order to estimate the isoscalar and isovector radii the approximation is made that all nucleons can be thought of as having the same radius, namely the mean charge radius of the nucleus, $R_o = 1.2A^{1/3}$fm. Then

$$r_s^2 = \frac{3}{2}\left\langle T,T_z\left|\sum_{ij} x_i x_j(\vec{T}_i\cdot\vec{T}_j)\right|T,T_z\right\rangle \cong \frac{1}{2}R_o^2\left\langle T,T_z\left|\sum_{ij}(\vec{T}_i\cdot\vec{T}_j)\right|T,T_z\right\rangle$$

$$= 2R_o^2 T(T+1) \tag{11.19a}$$

where we have averaged over photon polarizations ($\langle x_i^2 \rangle = R_o^2/3$) and used the fact that $\frac{1}{4}\sum_{ij}(T_i \cdot T_j)$ is the nuclear total-isospin operator with eigenvalue T(T+1). In the same manner one obtains

$$r_v^2 = \frac{3}{2T_z}\left\langle T,T_z \middle| \Sigma x_i x_i T_{zi} \middle| T,T_z \right\rangle = (1/2T_z)R_o^2 2T_z = R_o^2 \qquad (11.19b)$$

and the ratio

$$\gamma = r_v^2/r_s^2 = \frac{1}{2T(T+1)} \quad . \qquad (11.19c)$$

Using the estimates of Leonardi and Rosa-Clot for isoscalar and isovector terms (neglecting exchange forces) one obtains the ratio

$$\beta = A_v/A_s = \frac{-2}{3}\frac{T_z}{A} = \frac{-2}{3}\frac{T}{A} \quad . \qquad (11.19d)$$

The treatment of the A_t term is somewhat ambiguous; since $r_t^2 = 0$ in this approximation it is reasonable to assume that $A_t = 0$ to the same approximation (note that both $r_t^2 = 0$ and $A_t = 0$ if N = 0 and since σ_T, σ_{T+1}, and σ_{T-1} are inherently positive, $r_t^2 = 0$ would imply that N = 0). The ratio is then obtained for the component energies

$$\frac{\bar{E}_{T+1}}{\bar{E}_T} = \frac{(1-T\beta)}{(1+\beta)}\left(\frac{1+\gamma}{1-T\gamma}\right) \cong \left(\frac{1+\frac{2}{3}\frac{T^2}{A}}{1-\frac{2}{3}\frac{T}{A}}\right)\left(\frac{1+\frac{1}{2T(T+1)}}{1-\frac{1}{2(T+1)}}\right) \quad . \qquad (11.20)$$

As a check, we apply equation 11.20 to the Zr^{90} nucleus (T = 5) and obtain $\bar{E}_{T+1} / \bar{E}_T \cong 1.35$; using $\bar{E}_T$ = 16 mev (from the (γ,n) giant resonance) the estimate is $\bar{E}_{T+1} \cong 21.5$ mev, which is in good agreement with Fallieros estimate of 21 mev (4). Since the approximations involved in equation 11.20 are highly model dependent, it would be foolish to assume that such an approximation is indeed applicable to all nuclear systems. In the past

there has been a tendency to state that the splitting is roughly 1/2 - 1 mev per excess neutron; this is probably a direct consequence of the fact that for the special case of Zr^{90}, Fallieros obtained an estimate of ΔE = 5 mev, or about 1/2 mev per excess neutron, and this was the earliest calculation of this type. From the complicated T dependence of equations II.18 it can easily be seen that such a simplification is not warranted. The important point to recognize is that the amount of splitting is not expected to vary linearly with T, rather the splitting energy will be quite sensitive to the details of the nuclear configuration. The validity of all estimates, such as equation II.20, is then dictated by the validity of the nuclear model employed. In the present case, the assumption has been made that an independent particle model is valid; if nuclear correlations or exchange forces are important, the approximation will be erroneous.

Applying equation II.20 to Zn^{64}, the case of interest in this experiment (A = 64 and T = 2), gives $\bar{E}_3/\bar{E}_2 \simeq 1.4$. Using $\bar{E}_2$ = 18 mev then yields $\bar{E}_3 \simeq 25$ mev or about 7 mev energy difference.

Partition of cross section strength

In a recent article by O'Connell (13) a sum rule is given which relates the bremsstrahlung weighted cross sections $\sigma_{-1}(T)$ and $\sigma_{-1}(T+1)$. This sum rule can also be obtained using the formalism of Leonardi and Rosa-Clot. Briefly, using equations II.10, II.13, and II.15a one obtains an expression for the (physical) bremsstrahlung weighted cross sections in terms of the isovector and isotensor radii, which is the sum rule of O'Connell (here stated in the notation of Leonardi and Rosa-Clot)

$$\sigma_{-1}(T) - T\sigma_{-1}(T+1) = \frac{2\pi^2\alpha}{3}\left[(2T-1)Tr_t^2 + Tr_v^2\right] \quad . \tag{11.21}$$

Again it is assumed that $r_t^2 = 0$ (independent particle model) and using $r_v^2 = R_o^2 \cong 14A^{2/3}$mb and using the sum $\sigma_{-1} = \sigma_{-1}(T) + \sigma_{-1}(T+1)$ where σ_{-1} is the total inverse cross section one obtains

$$\frac{\sigma_{-1}(T+1)}{\sigma_{-1}} \cong \frac{1}{(T+1)}\left[1 - T\left(\frac{2\pi^2\alpha}{3}\right)\frac{R_o^2}{\sigma_{-1}}\right] \tag{11.22}$$

which can then be evaluated if a suitable estimate of σ_{-1} is available. For the case of a harmonic oscillator, one uses a resonance energy of $42A^{-1/3}$ and from the dipole sum rule, the total integrated cross section is given as 60NZ/A mev-mb so that $\sigma_{-1} \cong .36A^{4/3}$mb. Clearly the harmonic oscillator is not a good approximation since $42A^{-1/3}$ gives a resonance energy of about 10 mev for medium weight nuclei. A more realistic estimate can be obtained by comparison of existing data; empirically one estimates $\sigma_{-1} = .16A^{4/3}$mb (6), which will result in a smaller ratio.

Applying equation 11.22 to the Zn^{64} nucleus one obtains an estimate of $\sigma_{-1}(T+1)/\sigma_{-1} = 16\%$ using the empirical estimate of σ_{-1}, or 25% using the harmonic oscillator value. Since the remaining strength must be due to the $T_<$ component one then obtains $\sigma_{-1}(T+1)/\sigma_{-1}(T) = 19\%$ or 33%. Using equation 11.9 the ratio of the integrated cross sections is then found to be

$$\frac{\sigma_{int}(T+1)}{\sigma_{int}(T)} = \frac{\sigma_{-1}(T+1)}{\sigma_{-1}(T)}\frac{\bar{E}_{T+1}}{\bar{E}_T} = 27\% \text{ or } 47\% \quad .$$

It is important to emphasize that both estimates involve several model dependent quantities. In the second case, the patently unphysical harmonic oscillator estimate was used, in the first, an empirical estimate of σ_{-1}

was used but r_v^2 and r_t^2 are still assumed from an independent particle model.

Applying equation II.22 to the Zr^{90} case as a check, one obtains a value $\sigma_{int}(T+1)/\sigma_{int}(T) \cong 13\%$ for the harmonic oscillator estimate but using the empirical estimate one obtains a ratio which is approximately zero.

A somewhat different approach can be used to find the ratio of the integrated cross sections directly; using equations II.13, II.16, II.17, and II.19d one obtains the form

$$\frac{\sigma_{int}(T+1)}{\sigma_{int}(T)} = \frac{1}{T}\frac{(1-T\beta)}{(1+T\beta)} = \frac{(1+\frac{2T^2}{3A})}{T(1-\frac{2T}{3A})} \qquad (II.23)$$

which gives a ratio of about 25% for Zr^{90} and about 53% for Zn^{64}. This latter form again assumes an independent particle model but has the advantage of consistency with equation II.20 for the energy splitting -- it is noted that equation II.23 is in fact just the ratio of the integrated cross sections which was used to obtain equation II.20. This form also gives a result for Zr^{90} which is consistent with the ratio of $\cong$ 25% as obtained by Fallieros (4).

It is clear that the several estimates of the partition of component strength are not consistent although the O'Connell sum rule when used with the harmonic oscillator value of σ_{-1} does agree reasonably well with the result obtained using II.23. For the purposes of this experiment, it is perhaps best to assume that the above cross section ratio estimates merely describe the gross range of values which might be expected from an isospin model. Certainly, the above results would imply that the $T_>$ component of

Zn^{64} should account for something like 20-40% of the total integrated cross section; allowing latitude for the approximations involved, an experimental value in the range of 10-50% of the total integrated cross section would not be a direct contradiction of the model.

Application to Zinc 64

The general ideas of isospin allowed and isospin forbidden decay channels have been developed in Chapter I for an arbitrary nucleus and equations suitable for estimating the quantitative features of isospin splitting in a single particle model have been developed in the previous section and have been applied to Zinc 64. The intent of this experiment as indicated in the first chapter, is to compare the strength of the (γ,np) channel in a suitable nucleus with as many of the other channels as are possible. The Zn^{64} nucleus is an attractive candidate for this study since the (γ,n), (γ,np), and $(\gamma,2n)$ reactions all result in positron emitting residual nuclei and it is thus possible to simultaneously measure these three products by the activation method, the three positron components being detected by a simple annihilation-gamma coincidence scheme and separated by halflife. Thus, Zn^{64} is experimentally feasible for this study and it is now appropriate to consider the behavior predicted by the isospin interpretation.

Availability of the (γ,np) channel

The energy relations in the Zn^{64} situation are indicated in Figure 2; all energy levels are indicated in terms of excitation energy from the Zn^{64} ground state. The $T_<$ and $T_>$ resonance centroids are indicated at about 18 mev and 25 mev respectively, the first energy is known from other

Figure 2. Predicted T = 2 and T = 3 components of the Zn^{64} giant resonance, showing the decay modes allowed by the isospin selection rules. Solid lines represent known levels, broken lines represent isobaric analog levels expected to exist in this energy region and do not correspond to specific known levels. The lowest T = 5/2 level in Zn^{63} is particle stable and can decay only by gamma rays.

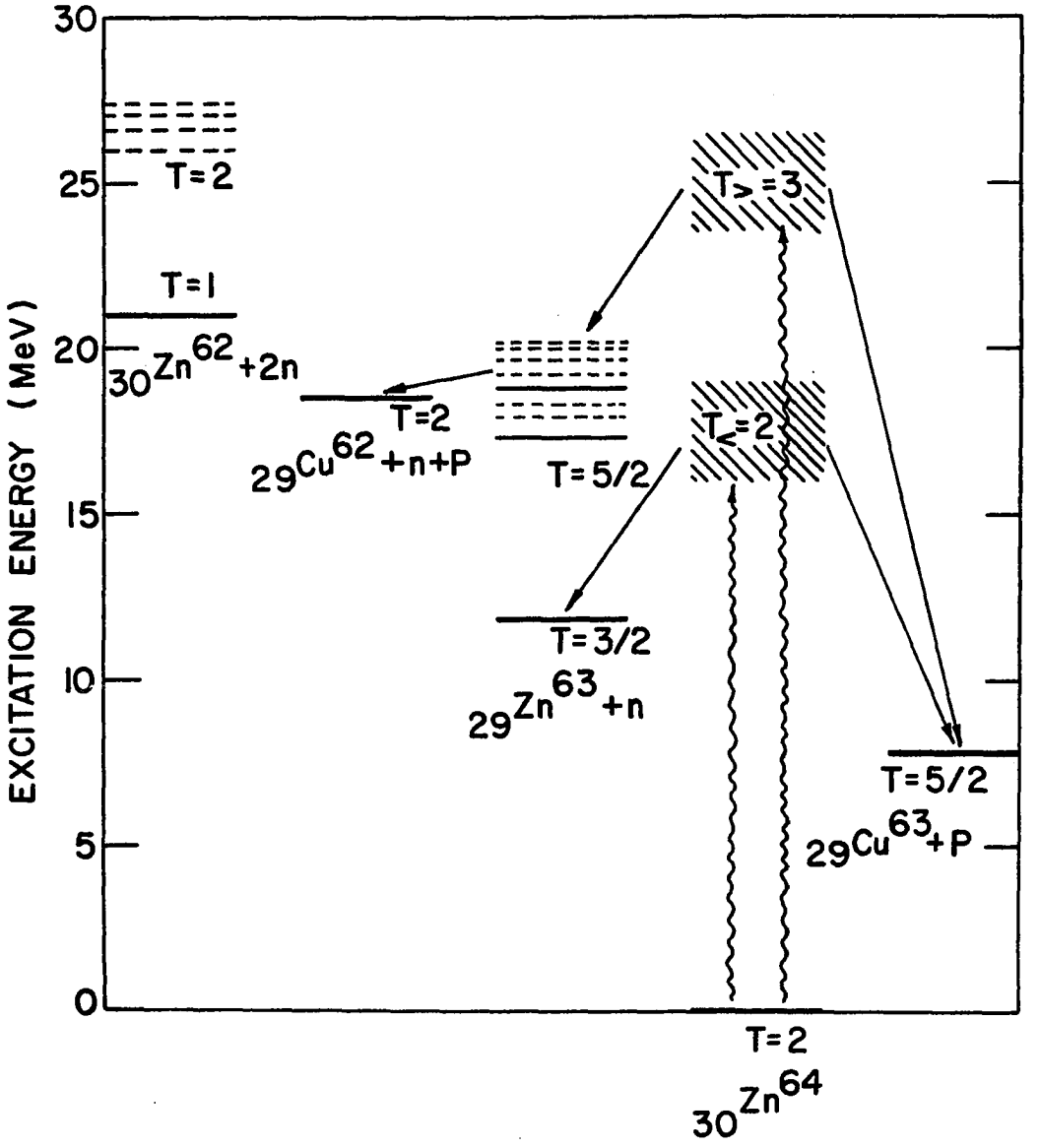
EXCITATION ENERGY (MeV)
30
25
20
15
10
5
0
T=2
T=1
30Zn62+2n
T=2
29Cu62+n+P
T=5/2
T=3/2
29Zn63+n
T>=3
T<=2
T=5/2
29Cu63+P
T=2
30Zn64

experiments and the $T_>$ mean energy was estimated from equation II.20.

There are two known T = 5/2 analog levels in Zn^{63} occurring at 5.42 and 6.8 mev respectively (14). (These are isobaric analogs of the Cu^{63} ground state and 1.547 mev level respectively.) Relative to the Zn^{64} ground state, the first of these analog levels can be reached for excitation energies in excess of 17.28 mev (Zn^{64} (γ,n) threshold = 11.86 mev) and thus is particle stable since the (γ,np) threshold is 18.55 mev. This T = 5/2 level will thus decay via gamma de-excitation and $T_>$ decays to this level are thus seen as isospin allowed (γ,n) reactions. The other T = 5/2 analog level occurs at 18.7 mev excitation energy relative to the Zn^{64} ground state and is thus proton unstable. There are undoubtedly other T = 5/2 analog levels occurring above 18.7 mev (indicated by broken lines in Figure 2) and these are also proton unstable. The threshold for the $(\gamma,2n)$ reaction occurs at 21 mev and so neutron decay from the excited Zn^{63} levels is energetically possible for excitation energies greater than 21 mev, however, the low lying Zn^{62} levels are T = 1 and neutron decay to these levels is therefore isospin forbidden. The T = 2 excited states (analogs of the low lying Cu^{62} levels) are estimated to become available at about 26 mev and are indicated by broken lines in Figure 2. (This estimate is based upon the expression for the symmetry energy given by Jänecke (15); $\Delta E_{sym} = 144(T+1)/A$, and for A = 62, T = 1 one obtains $\Delta E_{sym} \cong 4.7$ mev). The $(\gamma,2n)$ reaction is thus isospin allowed for excitation energies in excess of about 26 mev.

In summary, if isospin is a good quantum number, the $T_>$ component of the Zn^{64} giant resonance is expected to decay to the T = 5/2 excited levels in Zn^{63}; for excitation energies of less than 18.55 mev these levels can

only decay by gamma-dexcitation; for energies of 18.55 to 26 mev these levels should decay primarily by proton emission; for energies in excess of 26 mev neutron emission is isospin allowed. On the basis of the expected energy of the $T_>$ component, the (γ,np) process should thus dominate the $T_>$ cross section.

Relative strengths

The relative strength of the $T_>$ component has been estimated using equations 11.22 and 11.23; estimates of the integrated cross section ratio are $\sigma(T_>)_{int}/\sigma(T_<)_{int}$ = 27-53%. Despite the broad range of values included by this estimate, the range implies $T_>$ strength adequate for consideration of the predicted isospin effects. Since the (γ,np) channel should be the most favored channel for $T_>$ reactions (assuming the estimated energy splitting) and since the $T_<$ strength should be nominal in this channel, even as little as 10% of the $T_<$ strength should be quite apparent in the (γ,np) cross section.

Again, it is to be emphasized that the ratio of (γ,np) to $(\gamma,2n)$ strength is highly significant in this measurement. Although considerable (γ,np) strength might be predicted from a statistical model, the $(\gamma,2n)$ reaction is favored by the coulomb barrier above 21 mev and within a few mev above the $(\gamma,2n)$ threshold can be expected to dominate any two-nucleon evaporation process. The isospin prediction, on the other hand, predicts that the (γ,np) cross section is near maximum at 25 mev, which is 4 mev above the $(\gamma,2n)$ threshold. The relative strength and energetic behavior of the (γ,n) and $(\gamma,2n)$ cross sections is thus an important criterion by which to judge the applicability of the isospin interpretation.

Experimental considerations

As has been remarked earlier, the Zn^{64} nucleus is an obvious candidate for this study since three of the important reactions can be observed simultaneously with a relatively simple experimental arrangement. Since Zn^{64} is the dominant isotope in natural zinc (48.9%) and only one other isotope, Zn^{66} (27.8%) can produce positron emitting photoproducts, it is thus possible to use natural zinc targets for the experiment. Furthermore, the halflives of the three activities of interest are well separated ($Zn^{63} \cong 38$ min., $Cu^{62} \cong 10$ min., $Zn^{62} \cong 9$ hr.) and thus the components may be separated cleanly. Some experimental difficulties are encountered due to the mother-daughter decay scheme of the Zn^{62} - Cu^{62} pair and the presence of the 12.82 hour Cu^{64} activity ($Zn^{66}(\gamma,np)Cu^{64}$), but these difficulties are not intractable.

It is seen that the features of importance in this measurement are the relative amplitudes and overall shape and positions of the resonances for the reactions Zn^{64} (γ,n), (γ,np), and $(\gamma,2n)$; little importance need be attached to the existence of possible fine structure in the cross sections. It is thus sufficient to perform a low resolution ($\cong$ 1 mev energy increment) activation measurement of the photo-absorption cross sections. In the following chapter, the experimental criteria of importance in such a measurement are considered, and the actual measurement is described in detail.

CHAPTER III. MEASUREMENT OF THE YIELD CURVE

Statement of the Measurement Problem

The cross section for a photonuclear reaction is not directly observable, but it can be derived from quantities which are directly observable. It is the purpose of this section to determine precisely what measurements must be performed and what criteria are important in these measurements.

Relation of cross section to yield

The cross section for a nuclear reaction is related to the instantaneous reaction rate by

$$dN_{react}(k) = nI(t,k,\theta)\sigma(k) \qquad \text{III.1}$$

where $\sigma(k)$ = cross section for photon energy k,

$N(k)_{react}$ = total number of reactions which occur in the sample for photon energy k,

$I(t,k,\theta)$ = instantaneous beam intensity (the number of photons of energy k at time t and into angle θ),

and n = the total number of target nuclei in the photon beam.

Integrating over the bombardment time (0 to T) and the area (A) of the sample in the beam, and then dividing by the area A, one obtains

$$N(k)_{react} = n_s\sigma(k)d(k) \qquad \text{III.2}$$

where

$$d(k) = \int_0^A dA \int_0^T dt\, I(t,k,\theta) = \text{the number of photons impinging with energy k.} \qquad \text{III.3}$$

$n_s = n/A$ is the number of nuclei per unit area of sample in the beam.

In the case of a monochromatic photon beam, equation III.2 defines the cross section measurement in terms of the measurement of d(k) and the reaction rate $N(k)_{react}$. For a bremsstrahlung beam, the photon spectrum is not monochromatic but rather a continuous spectrum of photon energies is produced, ranging from zero to E_p, the bremsstrahlung peak energy. Thus for a bremsstrahlung beam, the observed number of reactions is the integral of equation III.2 over the bremsstrahlung spectrum

$$N(E_p)_{brem} = n_s \int_0^{E_p} \sigma(k) d(k) dk \qquad \text{III.4}$$

where $N(E_p)_{brem}$ is the number of reactions observed for a bremmstrahlung beam with peak energy E_p. It is convenient to define the measured "dose" $D(E_p)$

$$D(E_p) N(E_p,k)_{exp} = d(k) \qquad \text{III.5}$$

where $N(E_p,k)_{exp}dk$ is the number of photons in the experimental beam with energy in the range k to k + dk, which impinge on the sample, per unit of dosemonitor response. Equation III.4 now becomes, with this definition

$$Y(E_p) = \frac{N(E_p)_{brem}}{D(E_p)} = n_s \int_{E_T}^{E_p} N(E_p,k)_{exp} \sigma(k) dk \quad . \qquad \text{III.6)}$$

The lower limit of the integral is now taken to be E_T the threshold for the reaction under consideration. $Y(E_p)$ is the usual photonuclear yield function which is, by definition, the number of reactions per unit dosemonitor response for an incident bremsstrahlung beam of peak energy E_p.

Equation III.6 is the fundamental statement of the cross section measurement for bremsstrahlung radiation since it states the relationship of the experimentally measurable quantities (number of reactions and dose) to the cross section. In the statement of equation III.5 it was explicitly assumed that $N(E_p,k)_{exp}$ can be determined. In practice, it is very difficult to measure the spectrum of a bremsstrahlung beam and the usual practice is to redefine equation III.6 in terms of $N(E_p,k)$, an idealized spectrum.

$$N(E_p,k)_{exp} = \frac{f_s(k)N(E_p,k)}{F_M(E_p)} \qquad (III.7)$$

$f_s(k)$ is a function which corrects the ideal spectrum for the distortion of the bremsstrahlung beam at the target nucleus. Thus $f_s(k)$ corrects for absorption and scattering of photons in the sample and in any material ahead of the sample. $F_M(E_p)$ is a function which normalizes $N(E_p,k)$ to the monitor response. The idealized spectrum $N(E_p,k)$ is taken to be the Schiff integrated-over-angles bremsstrahlung spectrum (16,17,18) which has been used extensively in the past. The dosemonitor response function $F_M(E_p)$ is written as the product of several factors

$$F_M(E_p) = \phi(E_p)A(E_p)B(E_p) \qquad (III.8)$$

where

$\phi(E_p)$ = area under the bremsstrahlung spectrum
= (total energy onto the sample)/(photons in beam),

$A(E_p)$ = monitor response = (dosemonitor response)/(energy into dosemonitor),

and $B(E_p)$ = sample transmission = (energy into monitor)/(energy onto sample).

$\phi(E_p)$ is calculated from $N(E_p,k)$, the ideal spectrum, $A(E_p)$ is the calibration curve for the monitor and must be determined, and $B(E_p)$ is the sample attenuation and must also be measured for the experimental arrangement.

Yield measurement for an activation experiment

In many cases, such as the Zn^{64} situation, it is much simpler to measure the decay of radioactive nuclei than to detect the reactions by a direct method. This general method, the "activation" method, is quite straightforward, but thought must be given to the actual measurements which will be used to calculate the yields.

Separation of components

Photonuclear excitation of a nucleus typically occurs through several reactions and not all of these are of equal interest. An activation experiment immediately eliminates those reactions which proceed to stable nuclei; further elimination is obtained if the counting apparatus is designed to be sensitive to only a single mode of decay. In the present case, for example, it is possible to limit the observed decays to those listed in Figure 3 merely by the choice of a coincidence counting apparatus, sensitive only to positron emiting decay modes. For a nucleus such as Zinc, however, there are several positron emitting reaction products and it is necessary to separate the residual nuclei by analysis of the positron decay curve. An additional complication in the case of Zinc is that two of the reaction products (Zn^{62},Cu^{62}) are coupled by "mother-daughter" decay such that radioactive Cu^{62} can be created either by the (γ,np) reaction or indirectly by decay from Zn^{62} created by the $(\gamma,2n)$ reaction.

A fairly extensive mathematical treatment of the general multi-

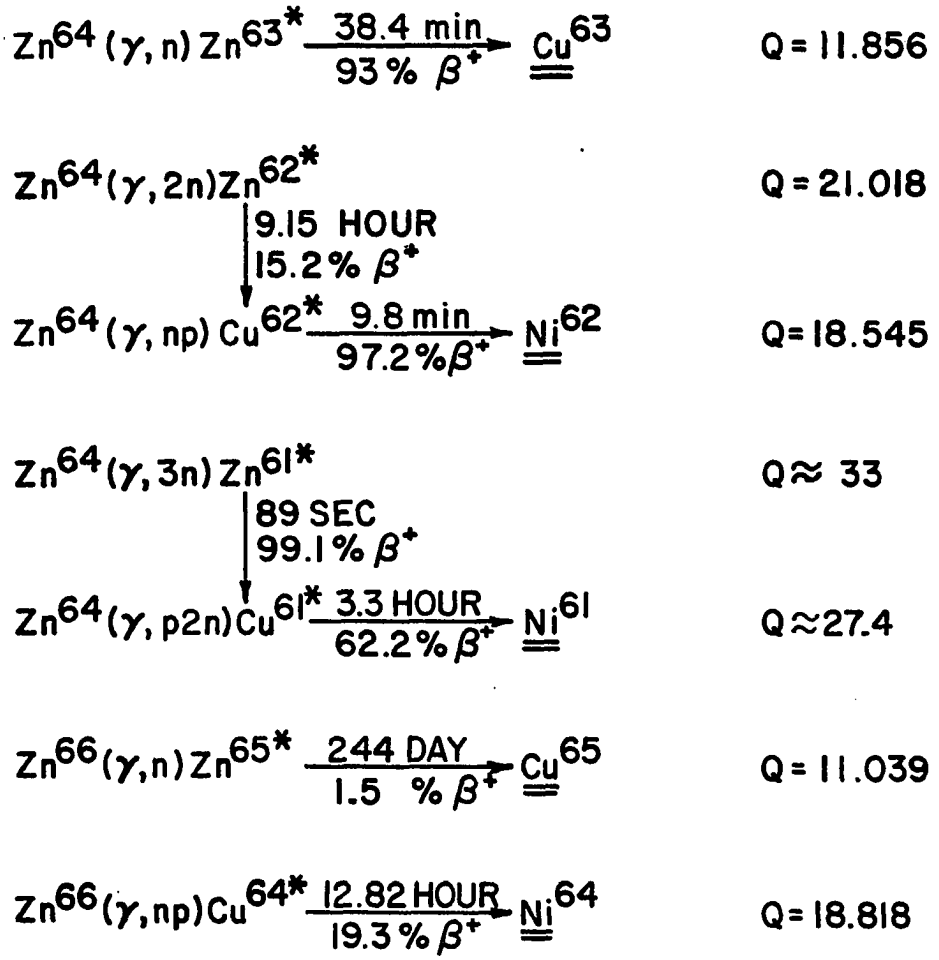

Figure 3. Photonuclear reactions in zinc which result in positron emitting residual nuclei. The halflives and positron branching ratios are taken from references 14, 19, and 20, the thresholds are taken from reference 21. The $Zn^{64}(\gamma,3n)$ and $Zn^{64}(\gamma,p2n)$ thresholds are inferred from the $Zn^{64}(\gamma,T)$ threshold.

component radioactive system is included as Appendix A and the application to the Zinc yield measurements is merely stated here:

1) If the decay curve for the system is measured, using suitable counting intervals, it is possible to perform a "least-squares" fit to the counting data, to obtain fitted coefficients A_i with uncertainties ΔA_i. (A_i is the "amplitude" of the component with halflife T_i.)

2) The radioactive decay of nuclei during finite irradiation times can be accommodated by the computation of a "corrected dose" D_c^i for each radioactive component. For suitably small time increments, all such corrected doses can be calculated, to good approximation, from a set of "dose increments" (dose accumulation over a time interval) spanning the entire bombardment time.

3) The fitted coefficients A_i can be related in a definite way to the number of radioactive nuclei present at end of bombardment, N_i, and appropriate statistical uncertainties ΔN_i can also be determined. In the normal case, A_i and N_i are proportional with a constant factor of proportionality; in the case of mother-daughter decay, the N_i representing direct photonuclear production of the daughter-state is also coupled to the mother-state coefficient by a term which involves corrected doses.

4) The photonuclear activation yield, Y_i, for the i^{th} reaction is then determined from

$$Y_i = N_i/D_c^i \qquad \text{(III.9)}$$

which is proportional to the absolute reaction yield as defined by equation III.6. The factor of proportionality involved is the same for all reactions and all bremsstrahlung energies.

The measurement of the yield for a given bremsstrahlung energy then requires only two experimental data: a set of dose increments measured over the entire activation period, and a set of measured counts accumulated during suitably chosen counting intervals which define the joint decay curve of the reaction products following bombardment. In addition, the analysis of the experimental data requires knowledge of the halflife and fractional positron emission for each reaction product; these physical constants are given in the literature (cf. Fig. 3) or, in the case of the halflife, might also be determined from the measured decay curves.

Reliability of the measurement

The overall reproducibility of a yield measurement is characterized both by the precision and the accuracy of the measurement. The precision of the yield is a measure of the uncertainty in the results due to random error and the accuracy is a measure of the deviation from the "true" yield due to systematic error. Although all sources of error, other than those arising from strictly statistical considerations, can be ultimately related to environmental and technical aspects of the measurement and could thus be considered to be systematic, it is most useful to define systematic errors to be those errors which result in reproducible distortion of the shape or relative amplitude of the yield curve (a yield curve is defined to be a

set of yield measurements determined for discrete bremsstrahlung energies). In the present case, an absolute cross section measurement is not intended and it is sufficient to measure the relative yields for each of the reactions; each of the yield curves is to be proportional to the "true" bremsstrahlung yield for that reaction by the same constant of proportionality. Thus, only those factors which result in non-proportional results will be considered to be sources of error.

Random error For any complex experimental configuration, there are a large number of sources of systematic error with a definite time dependence. To be exact, most time-dependence effects are associated with environmental factors (variations in line voltage, room temperature, atmospheric pressure, etc.) and "aging" effects (slippage of alignment brackets, aging of electronic components, abrasion of the samples, etc.), both of which result in apparent variation with time. In the first instance the effect is a time-dependent fluctuation, in the second, the effect is observed as a "drift" with time. In either case, the result of such time-dependent error is to increase the deviations between successive measurements. Furthermore, by randomizing the experimental procedure (in practice the energy sequence is randomized) it is ensured that time-systematic errors of either type will be observed as random (uncorrelated with respect to energy) deviations in the yield curve. Finally, even though the error sources are not known in detail, it is possible to eliminate the effect of long-term fluctuations and drifts by applying time-dependent corrections to the data. Such corrections can be obtained from independent measurements of the various system responses throughout the experiment or, in some cases, from the time-correlation of the yield deviations themselves. The important

point is that experimental errors which have a definite time dependence, whether corrected for or not, will appear only as random error if the experimental procedure is suitably randomized with respect to time.

The statistical nature of the radioactive decay process is a basic source of random error in all activation experiments. Since nuclear decay obeys Poisson statistics, the uncertainty in the measurement of N counts is known to be $N^{1/2}$. The same rule roughly pertains for a complicated system where several halflife components are involved; the uncertainty ΔN_i in the number of radioactive nuclei initially present, N_i, decreases towards the limiting value $N_i^{1/2}$ for well separated halflives and a "well determined" decay curve. In the present experiment, the statistical uncertainty in the coefficients of the 9.8 min (Cu^{62}) and 12.2 hour (Zn^{62}) components from a single measurement were typically .4% and .2% respectively for the optimum experimental configuration (the uncertainty for the 38 min (Cu^{63}) component was about an order of magnitude smaller). Since the total random error can be no smaller than the statistical contribution, it is sufficient to require that random error from experimental sources be limited to a few tenths of a percent or less. Since random error is by definition not reproducible, the random error of the measurement can be further reduced by performing many measurements at each energy and using the average yields.

Systematic error The systematic errors of concern are those which have a functional dependence on the bremsstrahlung energy or which might destroy the proportionality of the various reaction yields. There is a systematic error due to approximation of the corrected doses and the error decreases with increasing halflife so that this is a possible source of non-proportionality. Such error was determined to be less than .03% for

all dose quantities and is thus completely negligible. Since both the dosemonitor response and the measured counting rate increase strongly for increasing bremsstrahlung energy, non-linearity of either the dosemonitor or the counting system (count rate dependence) can lead to energy-dependent distortion of the yield. Non-linearity of the dosemonitor response will lead to an energy-dependent error which is more or less proportional for all reactions, but rate-dependence of the counter will distort the shape of the decay curve and thus may result in non-proportional distortion of each yield curve as a function of halflife. In addition, experimental distortion of the bremsstrahlung spectrum can occur as a function of peak energy. The accuracy of the measured results cannot be deduced from the deviations of the yields and can only be inferred by the comparison of independent experiments. Since inaccuracy in the halflife valves used in the experimental analysis could lead to systematic error in the determination of the several reaction yields, it is desirable both to determine the halflives from the experimental data, and to perform the experiment in such a way that systematic halflife errors will lead to observable deviations in the data. The latter objective can be realized most easily by observing that varying the bombardment time will vary the fraction of radioactive nuclei in the sample due to each reaction; the reproducibility of the yields for significantly different bombardment and counting times is thus a sensitive test of the analysis. Also, since the total counting rate increases strongly with bombardment time, distortions due to counter rate-dependence will also be apparent.

Experimental Technique

In the preceding section the measurement problem was considered and the required measurements were stated. In this section, the actual measurements will be described and special care will be taken to isolate those factors which might affect the reliability of the measurement.

Samples

The zinc samples used in this experiment were 16 gram discs 3 cm in diameter by 1/8 inch in thickness and were machined from natural zinc of 99.9% purity. The thickness of the samples corresponds to about one/sixth of a radiation length (about 12 gm/cm^2 for natural zinc) so the bremsstrahlung spectrum is not significantly distorted in passing through the samples. A sample attenuation curve was measured and is the $B(E_p)$ of equation III.8. The attenuation curve rises smoothly from a value of .914 at E_p = 10 to a maximum of 9.22 at 23 mev and then declines slowly to a value of .921 at 40 mev.

Thirty samples were used so that reasonably long times could be allowed for the long activities to decay away between activations. The set of samples was found to be very uniform in all dimensions, but normalization runs were performed to obtain appropriate corrections. The "sample normalization factors" calculated from these runs (designated the NORM runs) were all very near to unity (the extreme values being .982 and 1.010) and were determined to better than .3% precision.

Each sample was marked with an orientation dot on the perimeter. Although the samples were measured to each be flat within .001 inch or better, care was taken to always align the orientation marks with corresponding marks on the beam sample holder and counter trays to ensure

consistent sample geometry.

Activation

The geometry of the sample activation, or bombardment, is indicated in Figure 4. Electrons from the I.S.U. 70 mev synchrotron are incident on a thin tungsten target, and the resulting bremsstrahlung passes through the wall of the acceleration chamber, is collimated, and then strikes the zinc sample. Most of the bremsstrahlung beam passes through the sample and strikes an NBS type P2 ionization chamber. The very weak current output of the ionization chamber is integrated by charging a capacitor using a Cary model 31 vibrating reed electrometer. The voltage across the capacitor, which is proportional to the total dose, is measured by a Hughes model 5000A digital voltmeter whose output can be read to the SDS 910 computer. A discharge solenoid which can quickly discharge the integration capacitor is also interfaced to the computer so that the ionization chamber can be zeroed on command.

Energy control The energy control system for the Iowa State University synchrotron has been discussed in some detail previously(22) and past experience indicates that energies are reproducible to within 10 kev. The energy calibration for this experiment was performed several months earlier, but midway through the experiment the absolute energy calibration was checked by measurement of the sharp break which occurs at 17.27 mev in the O^{16} (γ,n) O^{15} yield curve and agreement was obtained within the accuracy of the measurement (approximately 30 kev). A subsequent measurement several weeks after the experiment also indicated no change in the energy calibration. On this basis, it is quite safe to assume that the uncertainty in the bremsstrahlung peak energy for this experiment is

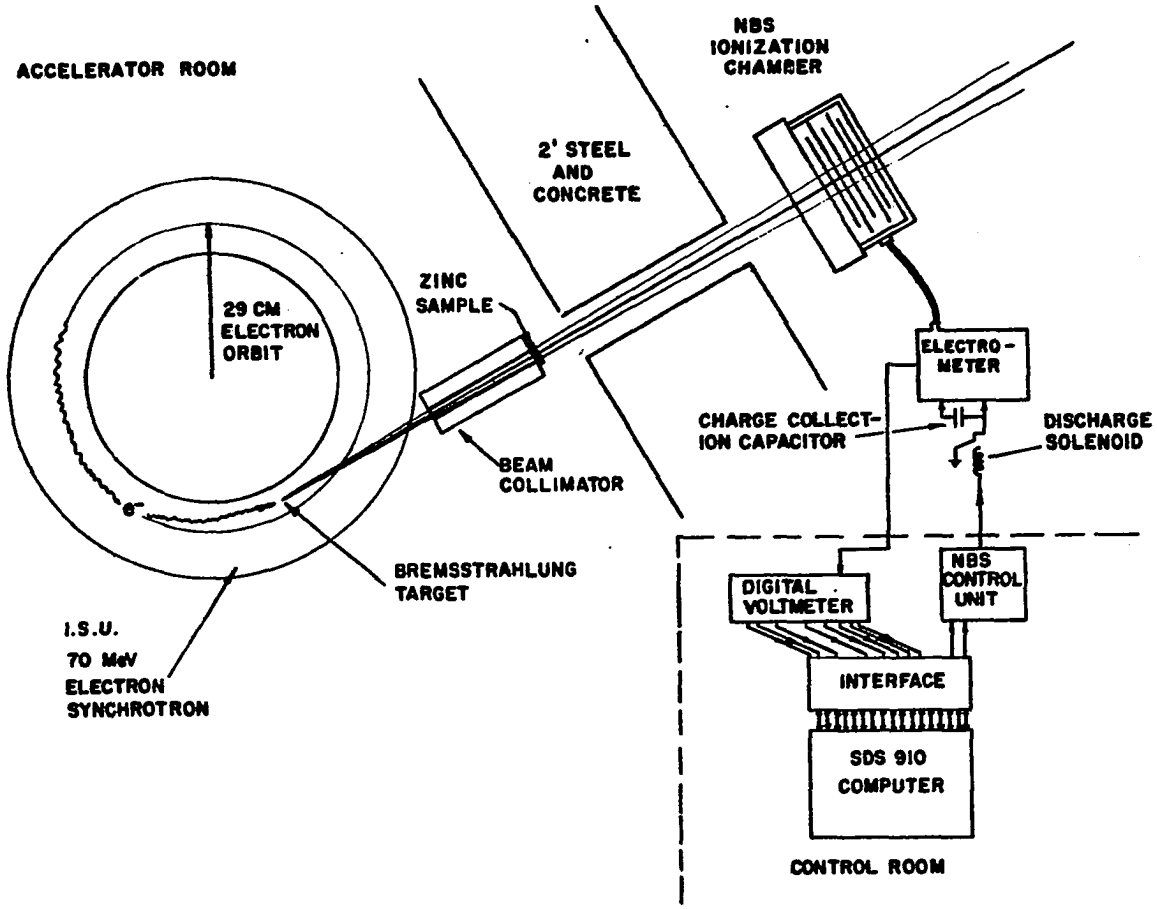

Figure 4. Bombardment geometry and dosemonitor system.

negligible with respect to the resolution required.

Beam geometry The eventual unfolding of equation III.6 for the cross section requires knowledge of the bremsstrahlung spectrum $N(E_p,k)$; since this function depends on the mean angle and solid angle which the sample subtends with respect to the bremsstrahlung target, it is important that beam geometry be consistent. This was ensured by carefully centering the collimator on the beam axis using the standard photographic and "copper cross" methods. The beam axis was carefully located by the latter method for energies of 20, 25, and 40 mev and was found to remain centered to within 1/32 inch or better at the front of the collimator. The collimated beam diameter at the sample position was about 7/8 inch so that the beam was entirely eclipsed by the samples and the solid angle subtended by the samples was thus constant. Care was also taken to ensure that the tapered interior walls of the collimator converged at the bremsstrahlung target in order to minimize possible spectrum distortion arising from scattering from the walls. A thick concrete and steel wall protects the ionization chamber from scattered photons which might give rise to spurious dose measurement.

Ionization chamber calibration The ionization chamber used for this experiment is a slightly modified version of the standard P2 ionization chamber which was developed and calibrated at the National Bureau of Standards and for which a calibration curve is given (23). The chamber used differs from the standard NBS chamber only in that it has been hermetically sealed and is maintained under a positive pressure of dry nitrogen in order to minimize fluctuations due to variations in atmospheric pressure and humidity. The modified chamber has been calibrated against a replica

of the standard NBS chamber and a calibration curve is known for the modified chamber; this calibration curve is the set $A(E_p)$ of Equation III.8. For the present, it is not necessary to worry about the absolute calibration of the monitor and the term "dose" will be used to refer to the voltage measured by the digital voltmeter.

Dosemonitor accuracy Frequent dosemonitor checks were performed during the experiment. The measurements were performed by inserting a standard ionizing source of strontinum 90 into a bracket attached to the NBS chamber; the electrons penetrate a thin foil window and simulate the ionization of electrons from bremsstrahlung. The monitor check consists of measuring the average rate of charge accumulation and standard deviation for a large number of 2 second time intervals. The standard deviations gave no indication of any nonlinearity of the dosemonitor response, but rather were consistent with the very small random error associated with the uncertainty in the reading of the least significant (.001 volt) digit of the digital voltmeter. Since the experimental doses typically range from a few volts to several hundred volts this error is negligible; moreover, since this is a random error it will tend to cancel out of the dose increments when the corrected dose equation is computed. A plot of the dosemonitor checks indicated a small and slow drift over the course of the experiment so that monitor response never changed appreciably during a bombardment; corrections for the drift were applied in the final analysis. Daily measurements of the charge leakage indicated a small and quite constant leakage corresponding to a dose gain of .01 volt/hour. A leakage this small should have negligible effect on the yields except possibly for very low energies or very low beam intensities. The leakage was also

corrected for in the final analysis.

Positron detection

The positron activity of the bombarded samples was measured in three separate detection assemblies, here referred to as "counting houses". Figure 5 indicates the configuration for one house. Each counting house consists of a pair of identical scintillation detectors mounted within a lead shield. The activated sample is placed between the detectors so that the back-to-back gamma rays from the positron annihilation enter the detectors simultaneously. Detector output pulses corresponding to energies below the .511 mev annihilation line are eliminated by EGG T100A discriminators and the logic output pulses from the two discriminators associated with a house are routed to an EGG C104 coincidence unit. The coincidence output pulses, corresponding to a positron annihilation, are counted by Darcy/TSI model 1535 dual 100 mc scalers from which the accumulated counts may be read to the SDS 910 computer upon command. The computer interface to the scalers also allows the 3 scalers to be zeroed upon command.

Detector geometry Each of the dual detectors in a counting house is composed of a 3 x 3 in. NaI(Tl) scintillation crystal in optical contact with an EMI 9531B (3 inch) photomultiplier tube and an emitter-follower preamplifier circuit to amplify the phototube currents. The detectors are mounted so that there is a separation of about 3/16 inch between the cases of the scintillation crystals. Since the samples are much smaller than the crystals, the solid angle for detection is nearly 4π and the detection efficiency is not highly dependent on the precise position of the sample. During counting, the samples are held securely on a sample tray by a spring loaded clip and the entire tray is then slid

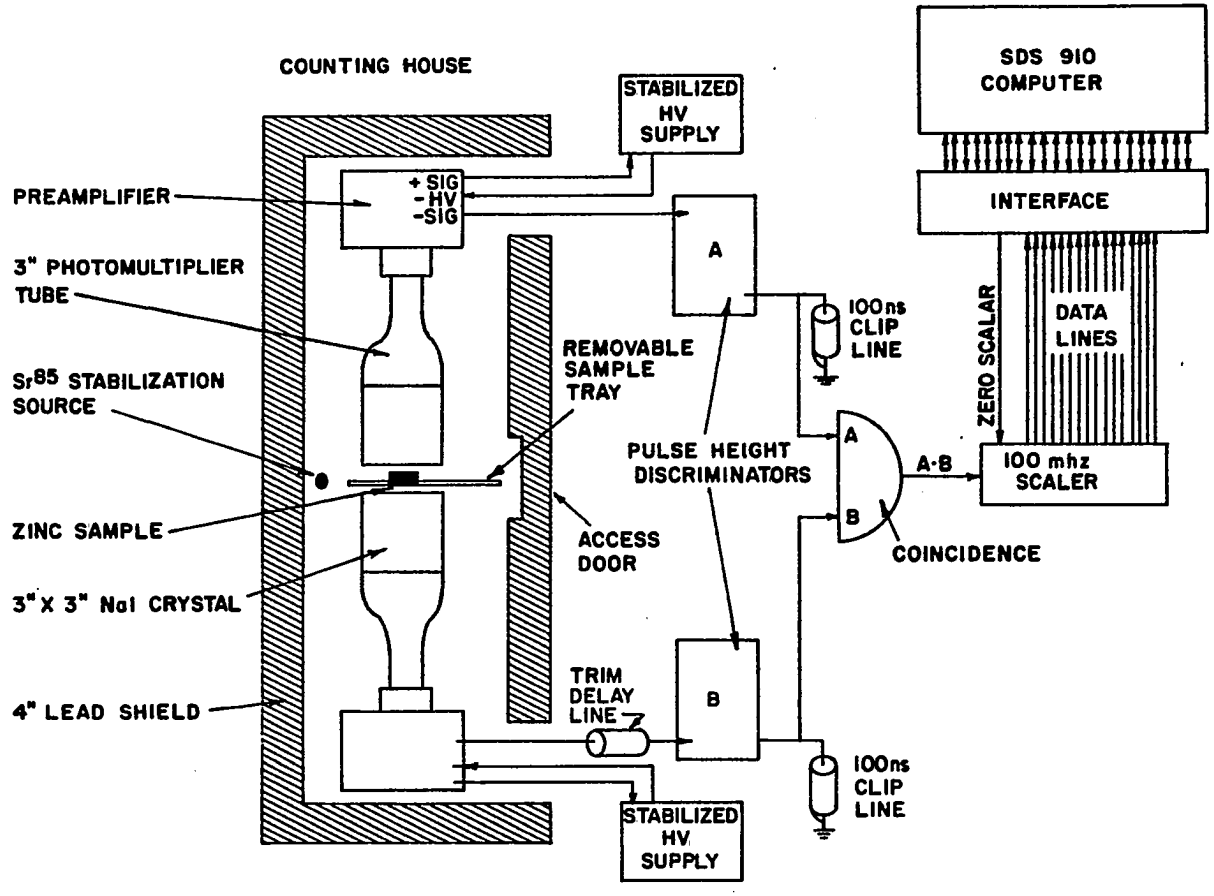

Figure 5. Counting house geometry and associated electronics (one of three is shown).

into guides which position the tray so that the sample is between the detectors. Previous experience with this counter arrangement indicates that reproducible positioning of the samples is not a problem so long as reasonable care is taken.

Detector normalization No serious attempt was made to adjust the geometries of the three counting houses to obtain identical counting efficiencies, so it was necessary to compute normalization factors. The house normalization factors were determined from the normalization (NORM) runs to a precision of about .2%. Houses 1 and 3 were normalized to house 2 and had normalization factors of .9702 and 1.1784 respectively. The differences in the normalization factors appear to arise primarily from differences in the detection geometry and the quality of the NaI crystals, rather than from differences in the associated electronics, since the efficiencies are quite insensitive to interchange of electrical components.

Energy discrimination The phototube high voltages were adjusted until the .511 mev annihilation line from Na^{22} was about 300 mv in the pulse spectrum from each detector. The discrimination thresholds were then individually adjusted so that the cutoff fell in the minimum of the valley between the annihilation peak and the Compton peak. Locating the threshold in a minimum of the spectrum and a linear part of the discriminator range helps to ensure that small changes in the analog pulse heights and discrimination levels will not give rise to large count rate variations. Actually energy discrimination for this experiment is not very critical since, by virtue of the coincidence requirements on the pulses, a change in discrimination level can only alter the positron detection efficiency but cannot introduce spurious counts from other parts of the gamma ray spectrum.

Coincidence timing The deadtimes of the discriminators were set by a capacitive delay network and were roughly 1 μs for each of the units. The output pulses were, however, clipped to 200 ns with shorted 50 ohm delay lines in order to minimize accidental coincidences. Short delay lines were added to the analog signal lines as necessary to correct for small differences in signal line length and circuit response. It was verified that the average arrival times for the coincidence pulses at the coincidence units were matched to within 10 ns and the timing jitter was only about 60 ns, so that the 200 ns coincidence resolving time is more than adequate.

Gain stabilization The high voltage for each of the detectors is supplied by a CRL type 1001B Spectrastat gain stabilized high voltage supply. These supplies stabilize the gain of the detectors by adjusting the high voltage for the system in such a way that a selected peak in the spectrum is maintained at constant amplitude. For this experiment the Spectrastats were locked-in on the .511 mev annihilation line, and a synthetic stabilization line was provided to prevent the Spectrastats from drifting off the peak when the positron activity was low. A weak Sr^{85} source was mounted adjacent to each detector pair to serve this purpose. The single .514 mev gamma ray produced by Sr^{85} is sufficiently close in energy to the .511 mev line to maintain the gain stabilization, yet its presence is not apparent in the coincidence counting rate. Counter checks were performed throughout the experiment and drift of the counting system amounted to only a few tenths of a percent per week; these drifts were probably dominated by drifts in the gain stabilization circuitry. The yields were corrected for counter drift in the final analysis.

Count rate dependence Dependence of detector efficiency on counting

rate is potentially dangerous for activation experiments since counting rates will increase with bombardment energy and such count rate dependence can thus introduce a distortion to the shape of the yield curve. There are three sources of such rate dependence:

1) Gain shift. Measurements of gain shift indicated a small but definite upward shift of the spectrum for increased counting rates. This gain shift amounts to a shift of about 10% of the full width at half maximum of the annihilation peak for the maximum counting rates encountered in this experiment. This effect is probably due to saturation of the pulse transformer which is used to invert and amplify the analog pulses used by the Spectrastats. All other circuits, from the phototube to the scalers, are direct-coupled and thus should not be susceptible to such effects.
2) Accidental coincidences. There is a finite probability that two physically independent gamma rays can be detected within the coincidence resolving time of the system and thus be erroneously counted as a coincidence event. This effect is obviously proportional to the coincidence resolving time and increases the observed coincidence counting rate.
3) Deadtime. If two events occur too closely together in time they cannot be distinguished and the second event is not counted. The minimum amount of time which must occur between successive events is referred to as the deadtime of the circuit. For this experiment, the discriminators

determined the deadtime for the entire system.

The last two effects will be collectively referred to as "slope" corrections since they affect the slope of the decay curve; they are considered in some detail in Appendix B where it is shown that the correction for both accidentals and deadtime is roughly proportional to the square of the observed counting rate. The observed counting rate-dependence was apparently dominated by the slope corrections and a set of satisfactory correction factors was determined; this point will be discussed later in this chapter. The required slope correction to the counting rates was never more than 2%.

The MULTIFACTORY routine

In the previous section the general problem of activity separation was discussed. In the present experiment, the 9.15 hour Zn^{62} activity presents the major practical difficulty since separation of this activity requires counting times on the order of one day. Since only three counting houses are available it would be possible to measure only about 3 yield points per day if each activated sample were to be counted continuously for the required 18-27 hours. Not only is such a procedure very impractical from a time standpoint, but it is also unnecessary since the major factor required for the separation of the long activity is that the shape of the decay curve be well determined; this can be accomplished with a fairly small number of counting intervals spaced throughout the decay curve and a good measurement of the background.

The procedure which was actually used for this experiment involved "interleaved counting" where each measured decay curve is made up of a number of counting segments which interleave with two or three other decay

curves in other stages of their development. Since the statistical validity of the results are not appreciably degraded if the counting intervals are appropriately chosen, this procedure actually improves the overall reliability of the experiment because more measurements can be performed within the available time.

In order to operate an interleaved counting experiment, it is necessary to maintain very careful control of all experimental timing. A computer program, designated as the MULTIFACTORY routine, was specially written to control all timing and data accumulation aspects of this experiment. A description of the MULTIFACTORY routine is included in Appendix C.

Counting schedule for a run

Three different run configurations were used for this experiment. The timing relationships are depicted in Figure 6. Each vertical column represents a "cycle" made up of 8 "phases". A phase is the basic block of time which MULTIFACTORY uses to schedule its activities, thus each phase can be labelled by a single type of activity, which may however be subdivided into smaller subintervals. A new run is begun in each house during each cycle with runs being initiated in houses 1, 2, and 3 during phases 0, 1, and 2 of the cycle. Note that the cycles of a run configuration interleave such that one and only one of the cycles involve counting during a given phase.

Precount phase Each run sequence begins with a precount phase (phase zero). The precount phase is made up of a single SC (Standard Count) and a single BG (Back Ground) count. During the SC interval, a standard source of Na^{22} is placed in the house and counted for a preset number of seconds. Since the standard source is quite active (about 5000 counts/sec) satisfactory statistics were obtained even for a two minute counting

Figure 6. The three time sequences used in this experiment. Each vertical column represents one cycle of eight phases. Shaded phases represent periods of counting activity. The counting phases are summarized in Table 1. The phase sequence shown is appropriate for counting house 1, the sequences for houses 2 and 3 are initiated in absolute phases 1 and 2 respectively. The LONG and SHORT maps are used for interleaved counting. Further details are included in the text and Appendix C.

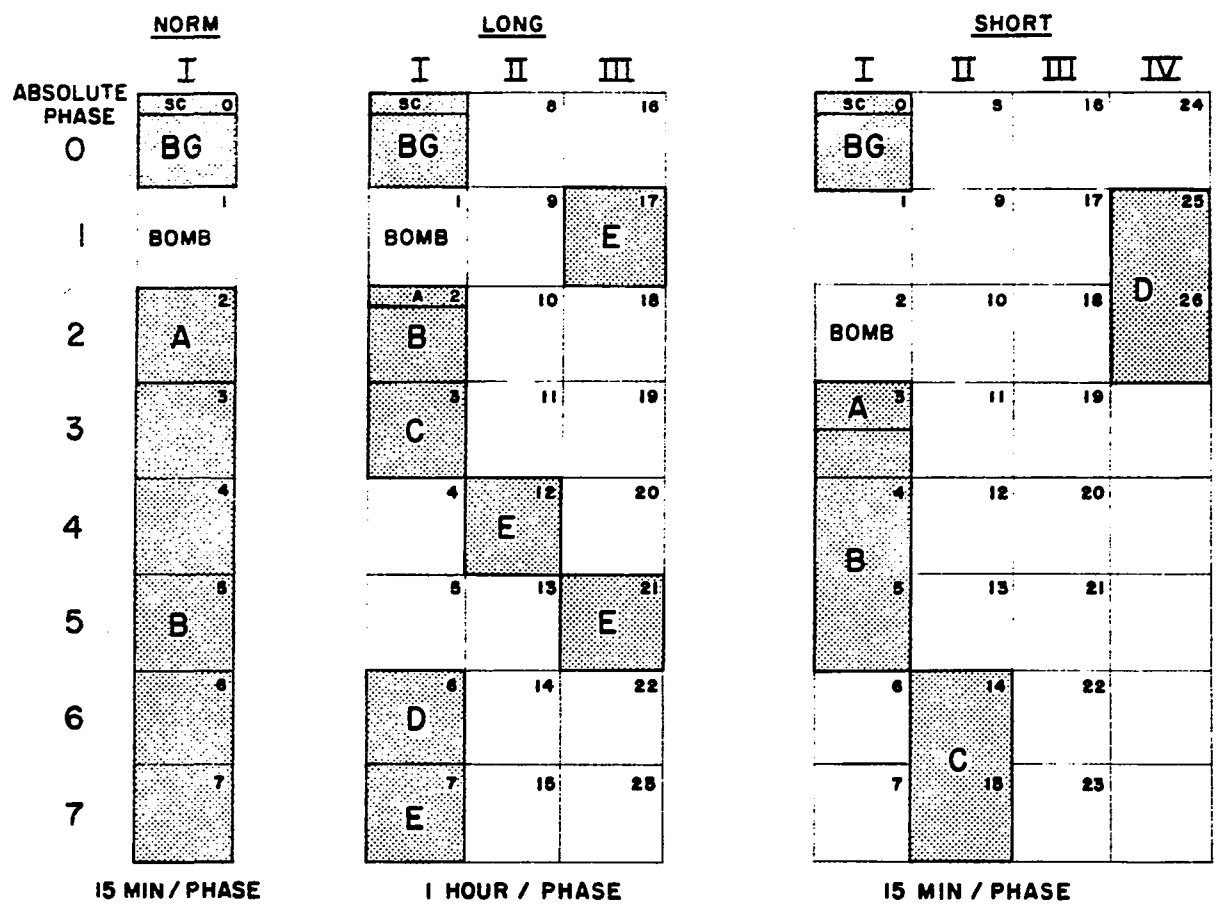
NORM
I
ABSOLUTE PHASE
SC 0
BG
1
BOMB
2
A
3
4
B
5
6
7
15 MIN / PHASE
LONG
I
II
III
SC
BG
8
16
1
BOMB
9
17
E
A 2
B
10
18
C
3
11
19
4
E
12
20
5
13
21
E
D
6
14
22
E
7
15
23
I HOUR / PHASE
SHORT
I
II
III
IV
SC 0
BG
5
16
24
1
9
17
25
D
26
2
BOMB
10
18
A
3
11
19
4
B
12
20
5
13
21
6
14
C
22
7
15
23
15 MIN / PHASE

interval. The SC measurements are used to determine the drift of the counting system. The BG count is another single counting interval, usually of much longer duration than the SC count, during which the "cool" sample is placed in the counting house and the residual background activity is measured. The BG count is the basis of the so called "infinite point" used in the least-squares fit.

Bomb phase During the bomb phase the precounted sample is placed in the synchrotron beam and irradiated. Actually, a variable length "wait" time precedes the bombardment and a 60 second "dash" time follows the bombardment so that the length of the actual bombardment is not the same as the length of the phase. During the bombardment, the computer reads the dose every two seconds and computes the corrected doses for the halflives specified. The dose increments are also output for a time interval which is an intergral number of the basic read times. Since the measured doses between 10 and 40 mev vary by more than two orders of magnitude, the linear range of the dose monitor had to be very wide to ensure meaningful increment measurements at low energy. The range of the dose monitor system was effectively extended to infinity by discharging the integration capacitor whenever the dose monitor achieved two thirds of the total linear range. The beam injection was gated off during this rescaling procedure so that no error in the dose measurement could occur.

Count sequence The count sequences are made up of groupings of A, B, C, D, E counting "blocks". Each of the blocks can be described by; 1) the length of a counting interval, 2) the number of such counting intervals to be performed, and 3) the length of a possible wait following the last counting interval. (The wait is generally taken to be zero unless a

sample change is necessary). Special precautions were taken to ensure accurate timing; it is estimated that timing errors should never exceed an extreme value of 1 millisecond.

Run configurations

The configuration parameters for the three types of runs are summarized in Table 1 and each type is discussed briefly below.

NORM runs These runs were performed in order to obtain the sample and house normalization factors. All NORM runs were made with 40 mev bremsstrahlung and since only the (γ,n) and (γ,np) yields were used to calculate the normalization factors, short bomb and count times were suitable. Each sample was run 4 times and the samples were counted in the same house each time; the averages of the yields from these runs were used to calculate the sample normalization factors. An additional 15 runs were performed with each sample rotated to the next house relative to its usual usage; these runs were used, together with the sample normalization runs, to obtain the house normalization factors.

LONG runs These runs provided the main body of information about the $Zn^{64}(\gamma,2n)$ process. Three yield curves, each consisting of at least one data point at each energy, comprise the LONG runs. The energies were selected at random for each yield curve in order to minimize systematic errors. Since 80 hours elapsed between successive bombardments of a sample, residual background rates were quite low for this series. The final six runs of this series were performed using samples of natural non-active copper of high purity and of the same dimensions as the zinc samples. These six samples were bombarded at 16 mev and were used to obtain a better determination of the Cu^{62} halflife.

Table 1. Summary of run configurations

	NORM	LONG	SHORT
Phase	15 min	60 min	15 min
Bombardment	12 min	58 min	9 min
Total Run Time	2 hrs	24 hrs	8 hrs
Runs/Day	36	9	36
Actual Time Counting	85 min	395 min	99 min
Dose Interval	Read every 2 secs Punched every 10 secs	Read every 2 secs Punched every 10 secs	Read every 2 secs Punched every 6 secs
SC	2 min	10 min	2 min
BG	10 min	44 min	10 min
Counting Sequences	A - 15 x 1 min B - 14 x 5 min	A - 12 x 30 secs B - 27 x 2 min C - 11 x 5 min* D - 12 x 5 min E - 5 x 11 min* *followed by 5 min for sample change	A - 14 x 30 secs B - 18 x 2 min C - 14 x 2 min* D - 7 x 4 min* *followed by 2 min for sample change
Number of Counting Intervals	29	82	53
Energies	40	10 - 40 mev in 1 mev steps	10 - 40 mev in 1 mev steps
Run Numbers	25-162	163-326	327-496

SHORT runs The SHORT run sequence of 3 yield curves was included to ensure that systematic errors associated with long bombardments and long counting intervals were not being mistaken for physical processes. Both the (γ,n) and (γ,np) activities were well determined by this counting configuration but neither the span of the counting, the amount of long activity created in such short bombardments, nor the determination of the background

was suitable for reliable measurement of the long-lived components. For each yield curve, at least two data points were taken for each energy from 18 to 25 mev and at least one point was measured at every other energy. Again, the energy sequence for a yield curve was randomized.

A 40 mev yield was measured roughly every sixth run for the LONG and SHORT run sequences as a convenient check of the overall system stability. These runs were included with the other runs for the analysis.

Data Reduction

The preceding sections of this chapter have discussed the data measurements necessary to determine the yield function. This section shall be concerned with the procedure by which the accumulated data was analyzed in order to calculate the yields for the three reactions of interest.

Procedure

The data accumulated by the MULTIFACTORY routine was processed by internal subroutines as well as being output on punched paper tape. The on-line calculations of MULTIFACTORY involved a four component least squares fit to the "slope corrected" data using halflives of 9.8 min., 38.4 min., and 9.15 hour, plus a background component. The corrected doses were also computed, the mother-daughter corrections applied, and the yields were typed as part of the on-line output. The MULTIFACTORY computations were primarily intended as a means of monitoring the experimental results, and an analysis routine, designated the PMF routine, was employed for the final analysis. The PMF routine was written for the Iowa State University IBM 360/65 computer, and it was possible to store the data from all 471 runs comprising this experiment on a direct access device so that corrections could be conveniently performed based upon the previous history of a sample;

this was especially useful for treatment of background and residual activity. It will become evident that the PMF refit was extremely useful since it allowed the data to be corrected for various second-order effects not possible to treat in the MULTIFACTORY routine, but it is notable that the essential experimental conclusions could have been obtained directly from the MULTIFACTORY analysis. A major advantage of the PMF refit is that it allowed the parameters of the analysis (halflives, slope corrections, etc.) to be altered at will, and thus it was possible to optimize these parameters by testing several trial values. Furthermore, since the essential features of the results were ultimately found to be quite insensitive to the precise values of these parameters and the details of the fitting process, a high degree of confidence in the validity of the analysis has been achieved.

A somewhat more complete description of the PMF routine is included in Appendix C, and the salient features of the general analysis technique will only be summarized here:

1) Errors. The statistical errors of all fitted quantities are computed from the uncertainties ΔA_i of the fitted coefficients A_i. In particular, for each computed N_i (number of radioactive nuclei at end of bombardment) an associated uncertainty ΔN_i is computed.
2) Corrected doses. The corrected doses for each activity are recomputed by PMF for the current halflife value. A correction for the small, observed dosemonitor "leakage" is also included in this calculation.
3) Weighting. An iterative procedure is used to obtain realistic weights for the least squares analysis. This

method is found to eliminate the known inaccuracy of the least-squares technique for data obtained with low counting rates (few counts in an interval).

4) Background treatment. In order to separate the long-lived activities from background rates, the measured sample background (obtained from the BG counts) is included as part of the data in the fit. Two methods are employed; both give equivalent results when used separately and the two were used together in the final analysis. The first method, called the "infinite point" method, involves including the "precounted" background (BG measurement prior to activation) as a data point obtained at "infinite" counting time. When used in this manner, the BG count is corrected for residual activity resulting from prior activation. The second method, known as the "next-point" method, involves the inclusion in the decay curve data of the BG measurement for the next run using this sample. By either method, a fitted background value is obtained as a component of the complete decay curve.

5) Residual activity correction. The fitted coefficients of each activity are corrected for the amount of this activity which remained from the previous activation of the sample. The uncertainty in this extrapolated correction is included when computing the error of each of the corrected results.

6) Slope correction of the counts. A slope correction (correction for rate-dependence of the counter) is applied to all counting data prior to fitting.

7) Halflife fitting. An iterative feature is included in PMF to allow any of the halflives to be "freed" to be fitted for their best value. The uncertainty of the fitted halflife value is also computed.

Determination of halflives

The Cu^{62} halflife is given in the literature (14) as 9.8 min. but the reported values are clustered at 9.75 min. and 9.92 min. with no error overlap. In order to determine this halflife more closely, six copper samples were activated as mentioned in Section B. Activation at 16 mev was chosen because this is below the threshold for all positron emitting reactions in copper except for the $Cu^{65}(\gamma,n)$ Cu^{64} and $Cu^{63}(\gamma,n)$ Cu^{62} reactions. The former produces a 12.92 hour activity which is not difficult to separate from the 9.8 min. activity. An additional advantage of the low bombardment energy is that the counting rates are low, so possible bias due to improper slope correction is negligible. The halflife fitting feature of PMF was employed to fit for the Cu^{62} halflife and an average of 582.5 ± 0.6 secs. ($9.71 \pm .01$ min.) was obtained. The uncertainty quoted is derived from the standard deviation about the average but this also agrees well with the uncertainty which PMF assigned to the fitted values. To ensure that there was no bias from the 12.82 hour halflife, the Cu^{62} fit was performed with the Cu^{64} halflife held fixed at 12.82 hour and repeated with it as a free halflife in the fit. The results were equivalent. The Cu^{64} halflife was also fitted from these data and gave an average value of $12.7 \pm .2$ hour

which is consistent with the value quoted in the literature (14).

A one-free-halflife fit was also made to the LONG run data for energies of 14 - 17 mev in order to determine the Zn^{63} halflife. All runs were discarded for which the previous bombardment energy was greater than 29 mev, and the remaining eight runs averaged to 38.45 ± .05 min. This is in agreement with the value of 38.40 ± .05 min. determined by Goss, et al (24). It was found that a halflife of 38.40 min. tended to cause the (γ,np) and $(\gamma,2n)$ yields below the 21 mev reaction thresholds to come in negative and positive respectively, but that both yields converged towards zero for larger values. A Cu^{62} halflife of 38.44 min. seem to be consistent with the data, as it gives proper threshold behavior, and was thus used in the fit.

Determination of slope correction constants

The approximation given in Appendix B was used to estimate the slope correction constants (counting rate correction factors) using rough measurements for each of the houses. The actual slope correction constants (α) used in the fit were determined empirically by fitting the 40 mev runs with several trial values of the slope constant. It was found that both the LONG and the SHORT (γ,np) yields increase as the slope constant is made more negative, as expected. Since the initial counting rates are much larger for the former, the yields for the LONG runs increase much faster with α than do the SHORT run yields, and there is found to be an α for each house for which the average LONG run yield is equal to the average SHORT run yield. The slope correction constants were thus chosen to be that value of α which resulted in a consistent (γ,np) yield for a house. It was also found that the (γ,np) yields for the three houses are equal for the constants

determined in this way and that these constants also tended to result in a minimum χ^2. The most striking indication of the validity of this method of determining the slope correction is the observation that the standard deviations of the LONG and SHORT yields, considered separately, were also minimized for these values. It should be noted that to avoid possible interference by 89 sec. Zn^{61} activity (from the Zn^{64} $[\gamma,3n]$ reaction) the first six points of each run were omitted from the fit.

The estimated values and the empirically determined values of the slope correction constants are given in Table 2. The two sets of values are really in quite good agreement considering the uncertainty of the constants used in the estimates. It might be significant that the final correction factors are all smaller than the estimates since the count-rate gain shift (discussed in the preceding section) would require a positive correction constant and would therefore decrease the total correction.

Table 2. Slope correction constants

HOUSE	Estimated	Used in PMF
1	-1.6×10^{-6}	-0.5×10^{-6}
2	-2.4×10^{-6}	-1.95×10^{-6}
3	-3.3×10^{-6}	-2.07×10^{-6}

Identification of significant activities

Until this point, attention has been directed to the three activities which result from the $Zn^{64}(\gamma,n)$, (γ,np) and $(\gamma,2n)$ reactions; namely 38.4 min. Zn^{63}, 9.71 min. Cu^{62}, and 9.15 hour Zn^{62}. Referring to Figure 3 it is seen that this is an oversimplification since other reactions, particularly from the Zn^{66} isotope, can be expected to contribute. Attention shall now

be directed to these activities, with regard to their approximate magnitude and importance to the analysis. For clarity the term "positron yield" shall be used when necessary to indicate that the yield has not been corrected for the fraction of positron activity.

244 day Zn^{65} The 244 day halflife of Zn^{65} is so much longer than the other halflives that this activity was treated as part of the sample background and no attempt was made to separate it from the natural background. An estimate of the counting rate contributed by the $Zn^{66}(\gamma,n)$ reaction can be made on the basis of the measured yield for the $Zn^{64}(\gamma,n)$ reaction. It can be estimated that for a one hour bombardment at 40 mev, the counting rate should never be increased by more than .01 counts/second. The measured background counting rates were on the order of 1 count/second and determined, at best, to about $\pm$ .02 counts/second. Since the background contribution due to the Cu^{65} activity was not significant in relation to the precision of the background determination, it was completely ignored in all calculations.

12.82 hour Cu^{64} The Cu^{64} activity can be expected to be a problem in the separation since the halflife is quite close to that of Zn^{62} (9.15 hour). An estimate of the size of the Cu^{64} contribution can be made by assuming that the $Zn^{64}(\gamma,np)$ and the $Zn^{66}(\gamma,np)$ reactions have the same yield, then by including the relative isotopic abundance of Zn^{64} and Zn^{68} (48.9% and 27.8% respectively) and the fractions of positron activity (97.2% and 19.3% respectively) it is estimated that the measured Cu^{64} positron yield should be reduced to about 10% of the Cu^{62} positron yield. Since the $Zn^{64}(\gamma,2n)$ yield is measured to be about 25% of the $Zn^{64}(\gamma,np)$ yield, it can be seen that the Zn^{62} and Cu^{64} activities could compete on

about an equal basis although, as will be seen shortly, the Cu^{64}/Cu^{62} positron yield ratio is actually somewhat smaller than 10%.

3.3 hour Cu^{61} A surprising amount of 3.3 hour activity was found to be present in the LONG run decay curves for energies above about 35 mev. The Cu^{61} activity is observed to be of nearly the same magnitude as the Cu^{64} activity, but since the halflife is considerably shorter, it does not cause as much difficulty in the separation of the "long" activities as the Cu^{64} activity does.

89 second Zn^{61} Although several attempts were made to detect the 89 second activity from Zn^{61}, no unambiguous evidence of such an activity was ever observed. The implication is that little, if any, of the 3.3 hour Cu^{61} activity is from the $Zn^{64}(\gamma,3n)$ reaction. On the basis of the average fit of 25 runs at 40 mev it is estimated that the $Zn^{64}(\gamma,3n)$ reaction accounts for 15% ($\pm$ 10%) of the observed 3.3 hour activity at 40 mev. The uncertainty in the above result is a direct consequence of the smallness of the 89 second activity with respect to the counting rates. Since the 89 second activity has negligible effect on χ^2 and the other coefficients of the fit, it has been neglected in this analysis.

Separation of long activities

From the preceding it can be seen that only 5 activities contribute to the decay curve: 9.71 min. Cu^{62}, 38.44 min. Zn^{63}, 3.3 hour Cu^{61}, 9.15 hour Zn^{62}, and 12.82 hour Cu^{64}. The first two activities are very well resolved and are easily fitted from the data. The last three activities are all of about the same order of halflife and the problem remains to separate these three long-lived activities in order to determine the 9.15 hour Zn^{62} yield.

It was found that whenever a 6 component fit (the above 5 activities plus background) was attempted on the LONG data, the uncertainty in the separation of the long activities was quite sizeable, as might be expected. It was possible however, to draw a smooth curve through the positron yield points for each activity, which seemed to be consistent with the spread of values. (Note that the large number of 40 mev runs helped to determine the end-point of the curve.) Since the corrected dose depends only on the dose increment data, it can be computed unambiguously for any activity of any run and thus, given the positron yield, the contribution of a given activity to the decay curve of a run can be computed. In this manner, the smoothed Zn^{62} positron yield was subtracted from the decay curve data (following application of the slope corrections) and a 4 component fit was performed to obtain a smoothed Cu^{64} positron yield curve. When the smoothed Cu^{64} positron yield points were plotted, it was noted that the $Zn^{64}(\gamma,np)$ yield curve was a reasonably good approximation to the $Cu^{64}(Zn^{66}[\gamma,np])$ data if shifted upwards in energy by about 2.9 mev and multiplied by a factor of .048. This was done and the Cu^{64} positron yield curve was then subtracted from the data and a smooth Cu^{61} positron yield was obtained. Finally, the smooth Cu^{64} and Cu^{61} positron yields were both subtracted from the data and a 3 component fit was performed to obtain the final $Zn^{64}(\gamma,n)$, (γ,np) and $(\gamma,2n)$ yields.

It should be pointed out that the procedure described above is quite subjective, in that, for the Cu^{64} correction especially, the data would allow for a considerable variation in the size and shape of the subtracted yield curve. The method did, however, appear to be reasonably unambiguous with respect to the amplitude of the $Zn^{64}(\gamma,2n)$ yield since the Zn^{62}

activity was measured to be about five times as large as the Cu^{64} activity. It is estimated that the systematic error in the $Zn^{64}(\gamma,2n)$ yield curve due to this method of correction should be no more than about 3% in the region of 30 to 40 mev and negligible in the 21 to 25 mev region. It is unfortunate that such a correction procedure is necessary, but as will be seen in the next chapter, the interpretation of the results is not notably impaired by this difficulty. It should be emphasized that the measurement of the $Zn^{64}(\gamma,n)$ and (γ,np) yields are not affected to any significant degree by these long halflife corrections.

It must also be emphasized that the use of the scaled and shifted $Zn^{64}(\gamma,np)$ yield curve for the Cu^{64} correction should not be construed as a statement that the two yield curves were measured to be identical, merely that within the rather broad limits of the measurement, the shape of the $Zn^{64}(\gamma,np)$ yield curve is consistent with the $Cu^{64}(Zn^{66}[\gamma,np])$ positron yield data. It can be quite definitely stated that the Cu^{64} yield is rising strongly in the 27 to 30 mev region and there is little reason to doubt that the Cu^{64} activity is indeed negligible below 24 mev.

It must furthermore be stated that the parameter of 4.8% is merely the ratio which seemed to give the best fit to the Cu^{64} yield curve. This ratio of 4.8% is the ratio of the "true" $Zn^{64}(\gamma,np)$ yield to the Cu^{64} "positron" yield. When isotopic abundances and fractions of positron emission are included, the above ratio is multiplied by a factor of $(1.0/0.193) \times (.489/.278) = 9.12$ so that the ratio of the $Zn^{66}(\gamma,np)$ yield to the $Zn^{64}(\gamma,np)$ yield is about 44%. Due to the large amount of interference between the 9.15 hour and 12.82 hour activities there is a considerable

amount of latitude in the Cu^{64} yield, so that this ratio could be as high as 60%, but it would be difficult to justify a larger value.

CHAPTER IV. EXPERIMENTAL RESULTS

In Chapter III, the determination of the cross section was related to the measurement of yield curves for the reactions and the actual yield curve measurements were described. In this chapter the final analysis of the yield curves will be described and the resulting cross sections presented.

Proceeding in the manner of Penfold and Leiss (18), equations III.6 and III.7 are conveniently combined in the form

$$y(E_p) = \int_{E_T}^{E_p} N(E_p,k)S(k)\,dk \qquad (IV.1)$$

where

$$y(E_p) = F_M(E_p)Y(E_p) = \text{the reduced yield} \qquad (IV.2)$$

and

$$s(k) = \sigma(k)f_s(k)n_s = \text{the reduced cross section.} \qquad (IV.3)$$

In the present case, care was taken to ensure that the bremsstrahlung spectrum was not appreciably distorted by the experimental geometry so that $f_s(k)$ is approximately unity and $s(k)$ can therefore be taken to be proportional to $\sigma(k)$ to good approximation. In the remainder of this discussion, since the absolute cross section is not of concern, it shall be assumed that $s(k) = \sigma(k)$ and no further mention of $s(k)$ shall be made.

Because the photonuclear yield is actually measured at discrete bremsstrahlung peak energies E_j (E_j = 10,11,...,20 mev) it is natural to replace the integral of equation IV.1 by a summation over discrete energies

$$y(E_i) = y_i = \sum_{j=1}^{i} N_{ij}\sigma_j \qquad (IV.4)$$

where

$$\sigma_j = \frac{1}{\Delta E} \int_{k_j - \Delta E}^{k_j} \sigma(k)\,dk \qquad (\Delta E = 1 \text{ mev}) \qquad (IV.5)$$

is the average of the cross section for the photon energy interval $k_j - \Delta E$ to k_j and N_{ij} is the number of photons in the bremsstrahlung spectrum in the same interval, for bremsstrahlung peak energy E_i.

Preparation of the Yield Curves for Least Structure Analysis

In this laboratory, it has been the practice to solve equation IV.1 for the interval-averaged cross section by the "least structure" method of Cook (25). The least structure solution requires the reduced yields y_i and their associated uncertainties d_i. The method of least structure will be discussed in the following section and the determination of y_j and d_j from the data will be considered at this point.

A general purpose computer routine, designated the APU routine is used to convert the "raw" fitted data from the experiment to the reduced yields y_i and errors d_i suitable for least structure analysis. The house normalization factors, and "time-dependent" corrections (corrections for counter and dose monitor drift) are applied as part of the APU analysis. An additional small correction for the so-called "betatron dose" is also applied to the (γ,n) corrected doses. The reduced yields y_i are formed from the measured yields $Y_i = N_i/D_c^i$ (number of radioactive nuclei at end of bombardment divided by corrected dose) by multiplying by $F_M(E_i)$, the dose monitor response function of equation III.8. The average reduced yield $\bar{y}_i$ is computed for each energy E_i and the associated uncertainty $\bar{d}_i$ is computed as

$$\bar{d}_i = (S_i^2 + \epsilon \bar{y}_i^2)^{1/2} \quad , \qquad (IV.6)$$

where S_i is the RMS statistical uncertainty (computed from the ΔN_i associated with each N_i from the least squared fit) and $\sqrt{\epsilon}$ is a constant representing the average fraction of "experimental" error for the yield curve. A brief description of the APU routine, the method of applying the aforementioned corrections, and the calculation of the yield errors is included in Appendix C.

For purpose of analysis, the data was grouped into several sets to obtain several independent reduced yield curves for each reaction. Hereafter, the reduced yield curves averaged from a particular set of input data will be referred to simply as a "yield curve" and the associated set of total errors, computed as above, as the "curve error"; collectively, the term "curve" will be used to designate the complete set of data being analyzed, and of course, such a curve includes data specific to one reaction. For brevity, curves averaged from only the LONG run data shall be designated as "L" curves, those from the SHORT run data as "S" curves, and those including both LONG and SHORT run data as "T" (total) curves.

The ordinary (not monitor corrected) yield curves are shown in Figure 7 and the reduced yield curves (monitor corrected) are displayed in Figures 8, 9, and 10. In each case, only one curve for the reaction is shown since all curves agreed within errors. Error bars are not indicated since they are considerably smaller than the dimensions of the plotted points. An additional curve, designated as the $(\gamma,2n+x)$ curve is also shown in Figures 7 and 10. This curve was obtained in the same manner as the $(\gamma,2n)$ curve except that the estimated contributions from 12.8 hour $Cu^{64}(Zn^{66}[\gamma,np])$ and

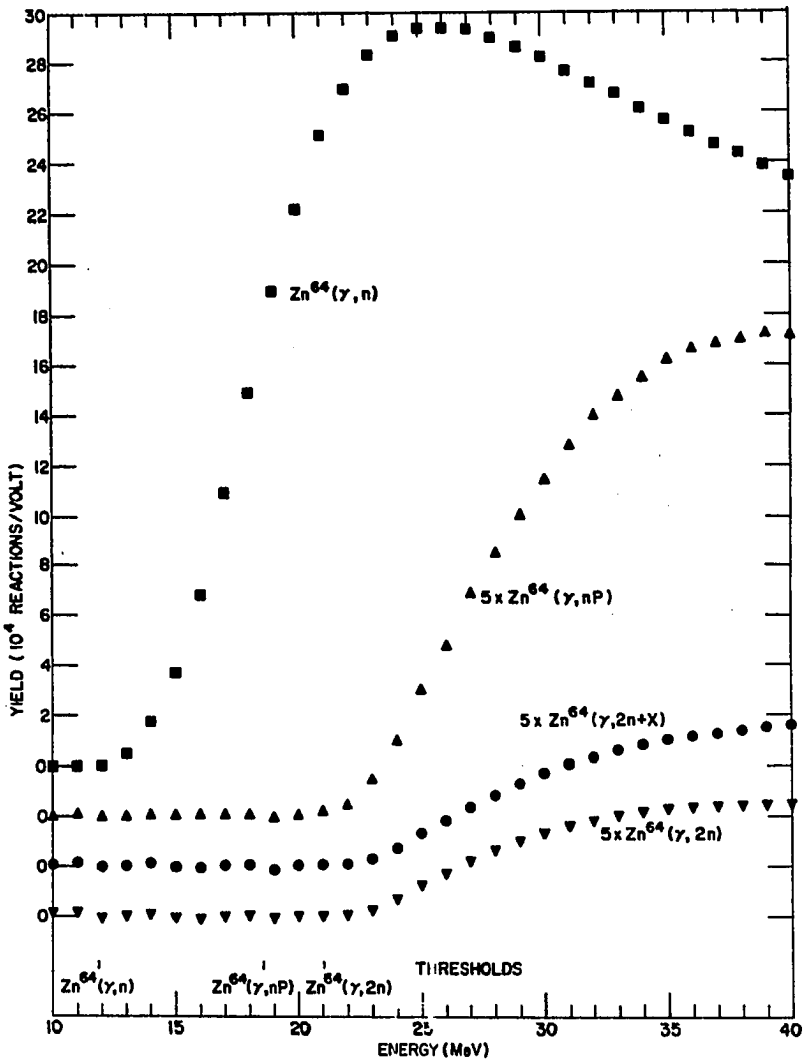

Figure 7. Yield curves for the measured reactions. The (γ,n) curve is drawn to the indicated scale, the other curves are scaled by a factor of 5 relative to their measured values. The curve labeled $(\gamma,2n+x)$ is the $(\gamma,2n)$ curve obtained without subtracting the competing long activities.

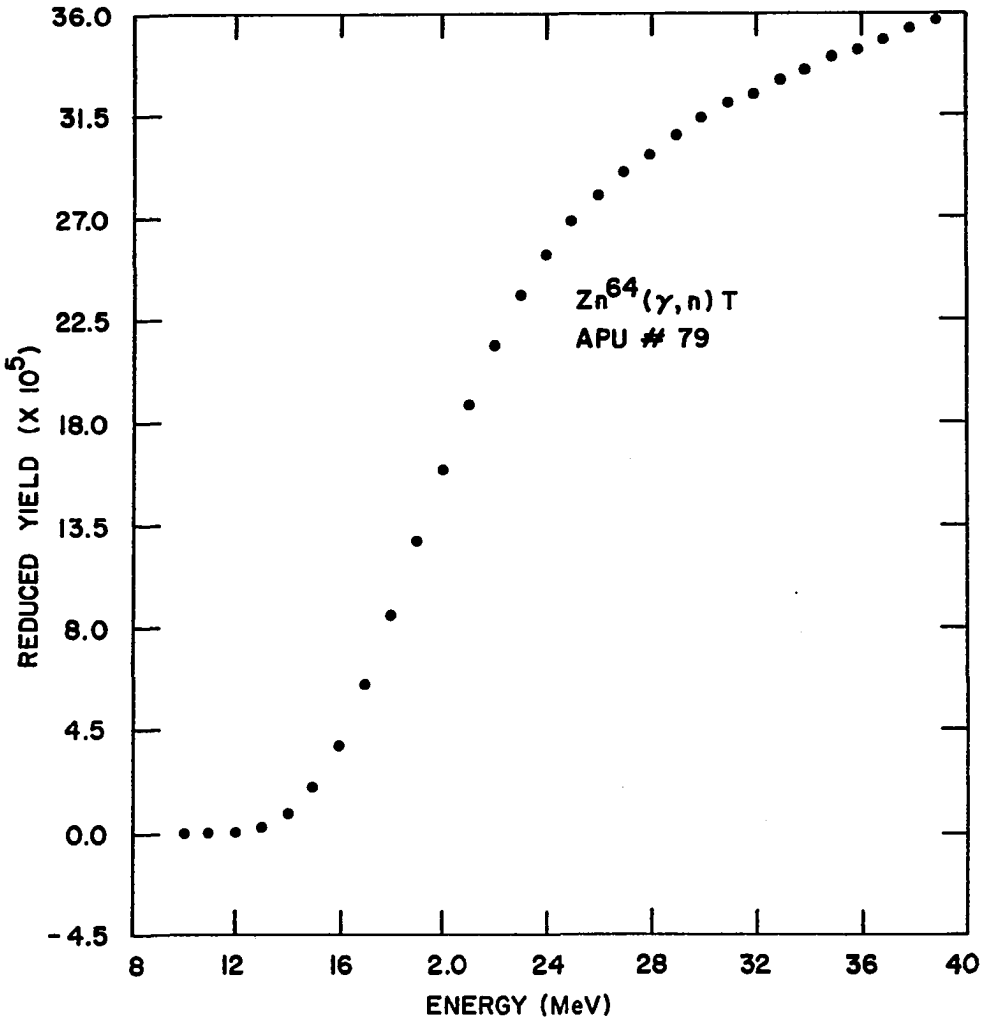

Figure 8. The reduced yield points for the $Zn^{64}(\gamma,n)$ reaction using all data.

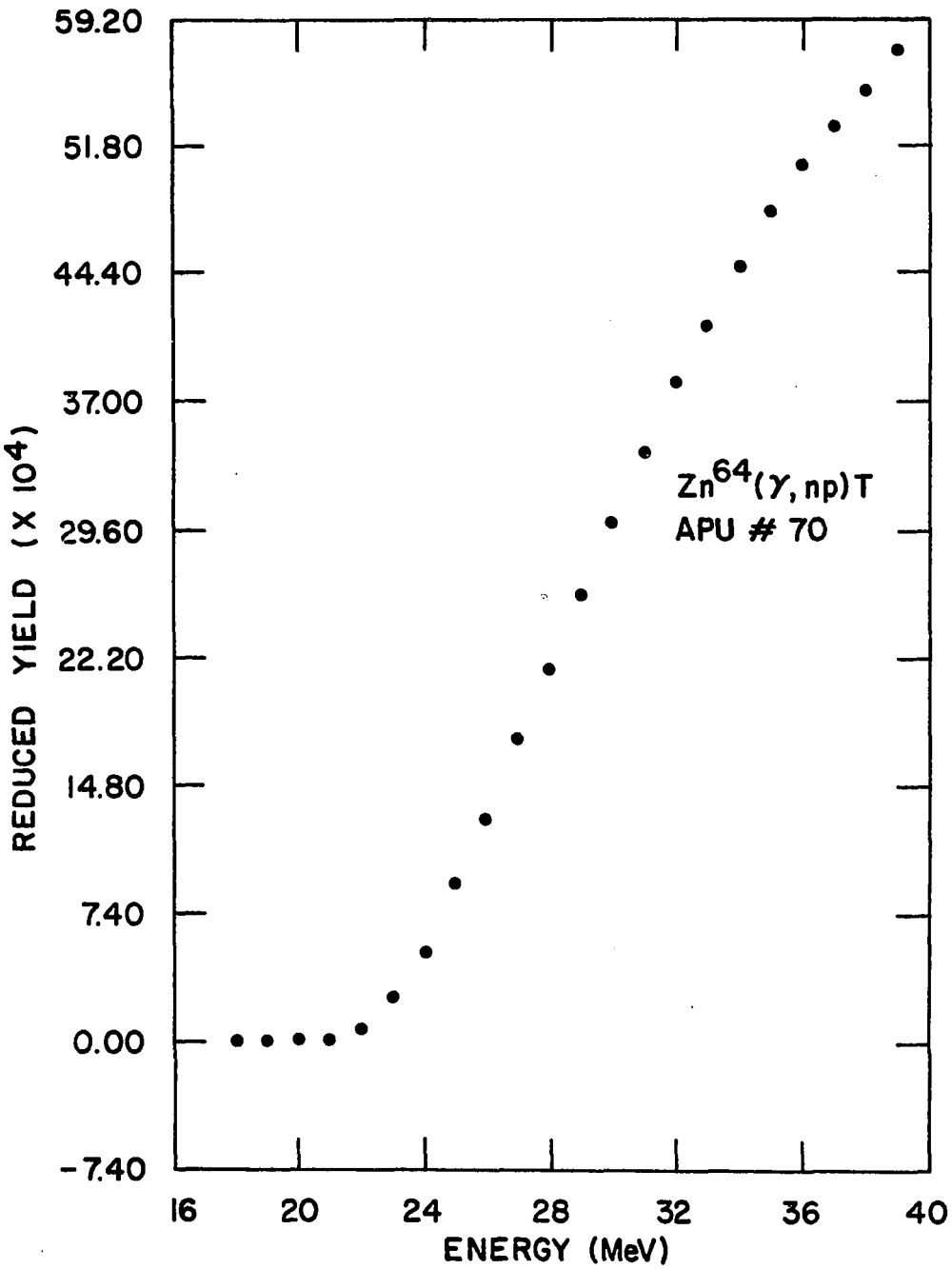

Figure 9. The reduced yield points for the $Zn^{64}(\gamma,np)$ reaction using all data.

Figure 10. The reduced yield for the $Zn^{64}(\gamma,2n)$ reaction using data from the LONG configuration only (cf. Table 1 and Figure 6). The $(\gamma,2n+x)$ curve includes contributions from competing long-lived activities and is indicated as a broken line.

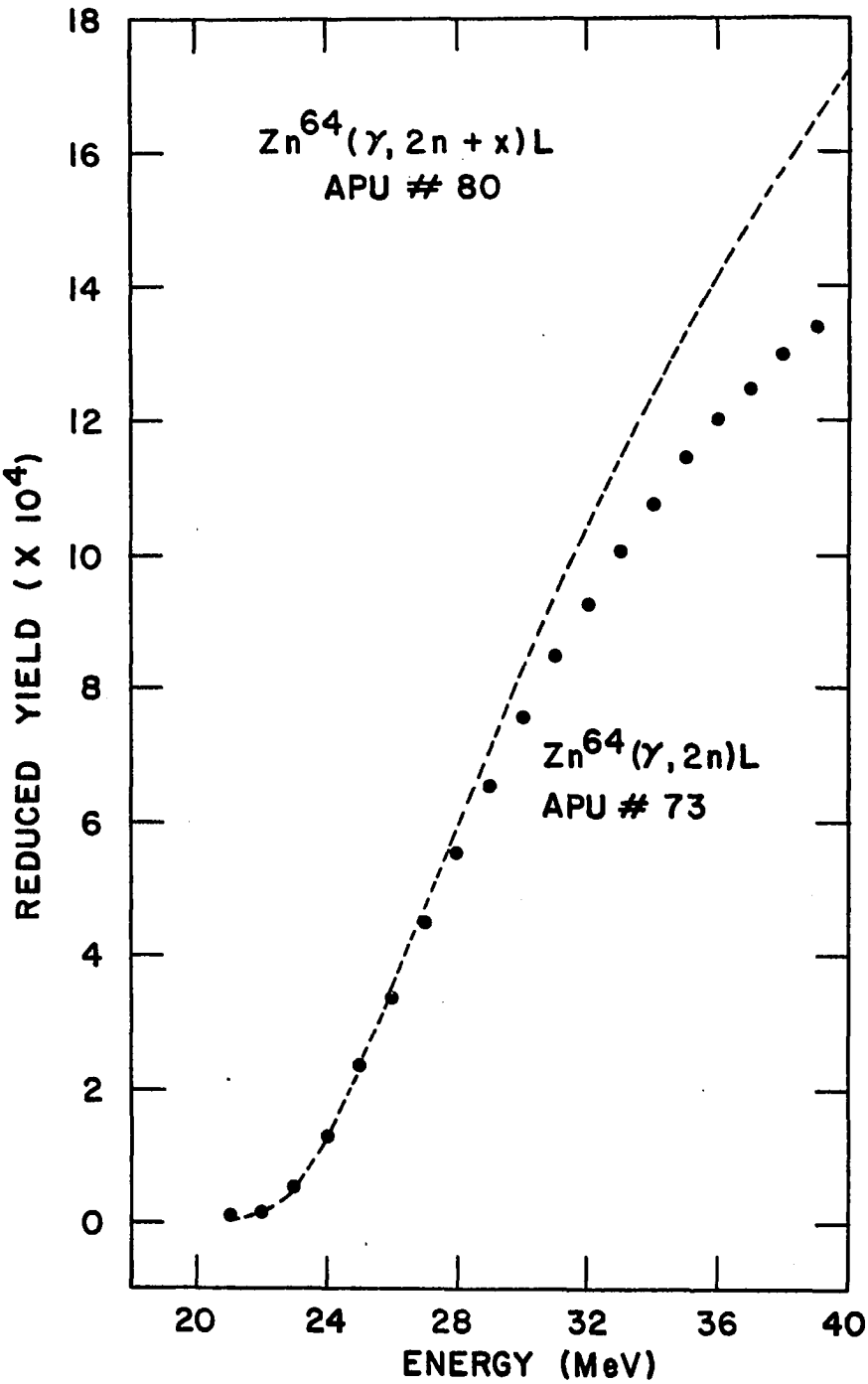
$Zn^{64}(\gamma, 2n + x)L$
APU # 80
$Zn^{64}(\gamma, 2n)L$
APU # 73
REDUCED YIELD (X 10^4)
ENERGY (MeV)
0
2
4
6
8
10
12
14
16
18
20
24
28
32
36
40

3.3 hour $Cu^{61}(Zn^{64}[\gamma,p2n])$ were not subtracted prior to fitting. Since this curve thus includes the contributions due to all long-lived activities, it can be considered as an extreme upper limit on the $(\gamma,2n)$ yield.

It was necessary at the onset to discard a small number of runs due to definite experimental errors (equipment failure, operator error, etc.) but a certain number of runs were included for APU analysis which were questionable because of suspected difficulties. On the basis of large deviations from the average (γ,n) yields, some of these runs were then eliminated. Altogether, a total of 43 of the 334 runs comprising the LONG and SHORT sequences were eliminated prior to the final analysis. All of the eliminated runs were associated with known or suspected experimental difficulties and no runs were eliminated solely on the basis of large deviations. The same runs were eliminated when preparing the curves for each of the reactions.

For the final analysis, only the 18 to 40 mev runs and 21 to 40 mev runs were used in the preparation of the (γ,np) and $(\gamma,2n)$ curves respectively. Least structure solutions utilizing all energies (10 to 40 mev) were initially obtained for each reaction and did not differ from the final results.

Table 3 summarizes the curves of interest. The quantity $\sqrt{\epsilon}$, as previously stated, is a measure of the fractional experimental error for all runs in a curve. The quantity $\overline{\delta}$, computed analagously to $\sqrt{\epsilon}$, is a measure of the average fractional total error (both statistical and experimental) for any run included in the curve. The quantity Q is a rough estimate of the average ratio of curve error to yield and is given by $Q = \overline{\delta}/m$ where m is the number of individual curves averaged to obtain the final curve. It

Table 3. Summary of reduced yield curves for this experiment

Reaction	$Zn^{64}(\gamma,n)$			$Zn^{64}(\gamma,np)$			$Zn^{64}(\gamma,2n)$		$Zn^{64}(\gamma,2n+x)$
Curve[a]	L	S	T	L	S	T	L	S	L
Number of runs	155	136	291	112	130	242	99	108	100
Lowest energy (mev)	10	10	10	18	18	18	21	21	21
$\sqrt{\epsilon}$[b]	.33%	.32%	.34%	.35%	.20%	.30%	.56%	7.6%	.38%
$\overline{\delta}$[c]	.34%	.36%	.37%	.59%	.55%	.59%	.64%	8.1%	.46%
Q[d]	.2%	.2%	.15%	.34%	.31%	.24%	.37%	4.7%	.26%
APU identification number	76	77	79	71	72	70	73	75	80

[a] L and S curves consist of data from LONG and SHORT configurations respectively. (Configurations are summarized in Table 1.) T curves contain all data.

[b] Average experimental error for individual runs included.

[c] Average total (experimental plus statistical) error for individual runs included.

[d] Estimate of average curve error (total error of average yields).

will be recalled that for the LONG and SHORT run sequences three separate curves (at least one run at each energy) were obtained. All of the 40 mev runs (roughly every sixth run) are included in the curves. It should be noted that for both the (γ,n) and (γ,np) reactions, $\sqrt{\epsilon}$ is roughly the same for the L, S, and T curves. If the LONG and SHORT yields for either of these reactions had differed significantly, the $\sqrt{\epsilon}$ associated with the T curve would be considerably larger than for either of the separate analyses since $\sqrt{\epsilon}$ is a measure of the average yield deviation beyond the uncertainty due to statistics.

Least Structure Solution of the Cross Sections

The solution of equation IV.4 for the interval averaged cross section values σ_j involves the solution of n linear equations in n unknowns. Various methods have been employed to obtain such solutions, typical of which are the "photon difference method" (26) and the method of Penfold and Leiss (18) (Penfold, Leiss method). The basic problem involved in the solution of equation IV.4, by any method, is that for high energies (especially above the giant resonance) differences between adjacent yield values are usually not a great deal larger than the uncertainties associated with the yields. As a result, the solutions obtained from direct solution of equation IV.4 tend to oscillate violently above the major resonance and it is difficult to distinguish physically significant structure from statistical oscillations in the solution. A method of "least structure" solutions of equation IV.4 has been developed by B. C. Cook of this laboratory and has been employed in several previous photonuclear experiments (22,27,28). The least structure method has been treated elsewhere (25) and the present discussion will be confined to a brief statement of those considerations

relevant to the interpretation of the results of this experiment.

For a given set of input data, there are an infinite number of "smoothed" σ_j solutions of equation IV.4; as the name implies, the method selects that solution which has "least structure". For a given "smoothing parameter" (λ) there is computed a unique solution of equation IV.4 which also minimizes a "structure function". The amount of local smoothing is dictated by the uncertainties of the yield data, thus, for a given λ more structure is allowed where the yield curve is well defined than is allowed where the data is more poorly defined. The proper amount of smoothing can be estimated by using equation IV.4 to calculate the "true" yields implied by a given set of σ_j, solutions. These can be compared with the measured yields and should typically agree within the known uncertainties in the yield measurement. Thus, there is a criterion by which to judge when a solution is properly smoothed.

In practice, a computer program, known as the CLSR routine, is used to compute the least structure solutions. Trial values of λ are specified and the routine repeatedly solves for least structure solutions, estimating new values of λ as necessary, until a solution of desired smoothness is obtained.

It may be noted that λ effectively defines the "resolution" of the solution, that is, the minimum width of any local structure is determined primarily by λ. Thus, solutions obtained from equivalent yield data sets are best compared when analyzed with the same λ, even though such solutions may be over or undersmoothed for either data set.

The least structure cross sections for this experiment are given in Figures 11 to 15. Each of the cross sections was analyzed from the yield curve data summarized in Table 3 and is identified for reference. For

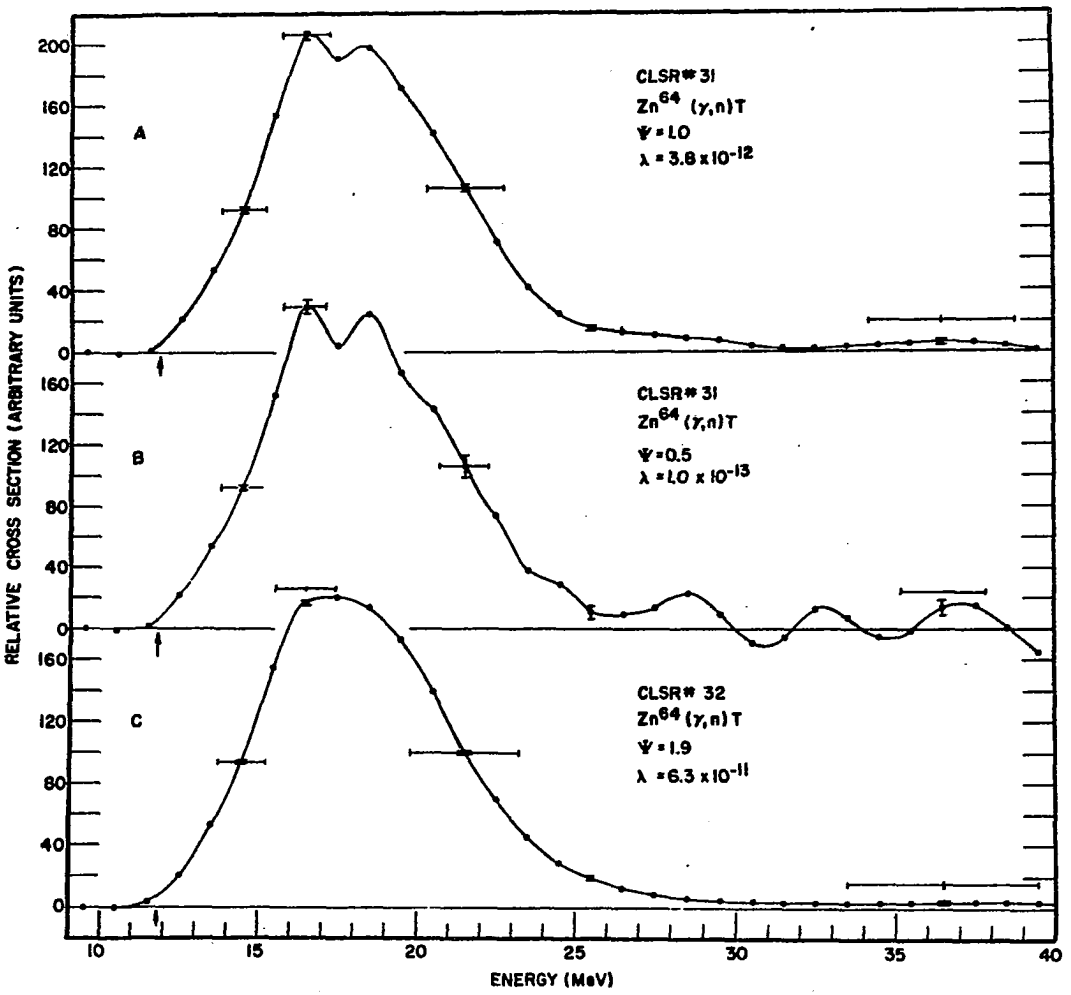

Figure 11. $Zn^{64}(\gamma,n)$ cross sections using all data. (a), (b), and (c) represent normally smoothed, undersmoothed, and oversmoothed analyses of the same data.

Figure 12. Oversmoothed analyses of the $Zn^{64}(\gamma,np)$ cross sections. (a) using all data, (b) using LONG (open circle) and SHORT (full circle) data only (the LONG and SHORT configurations are summarized in Table 1). The broken curve is the curve of 12a included for reference.

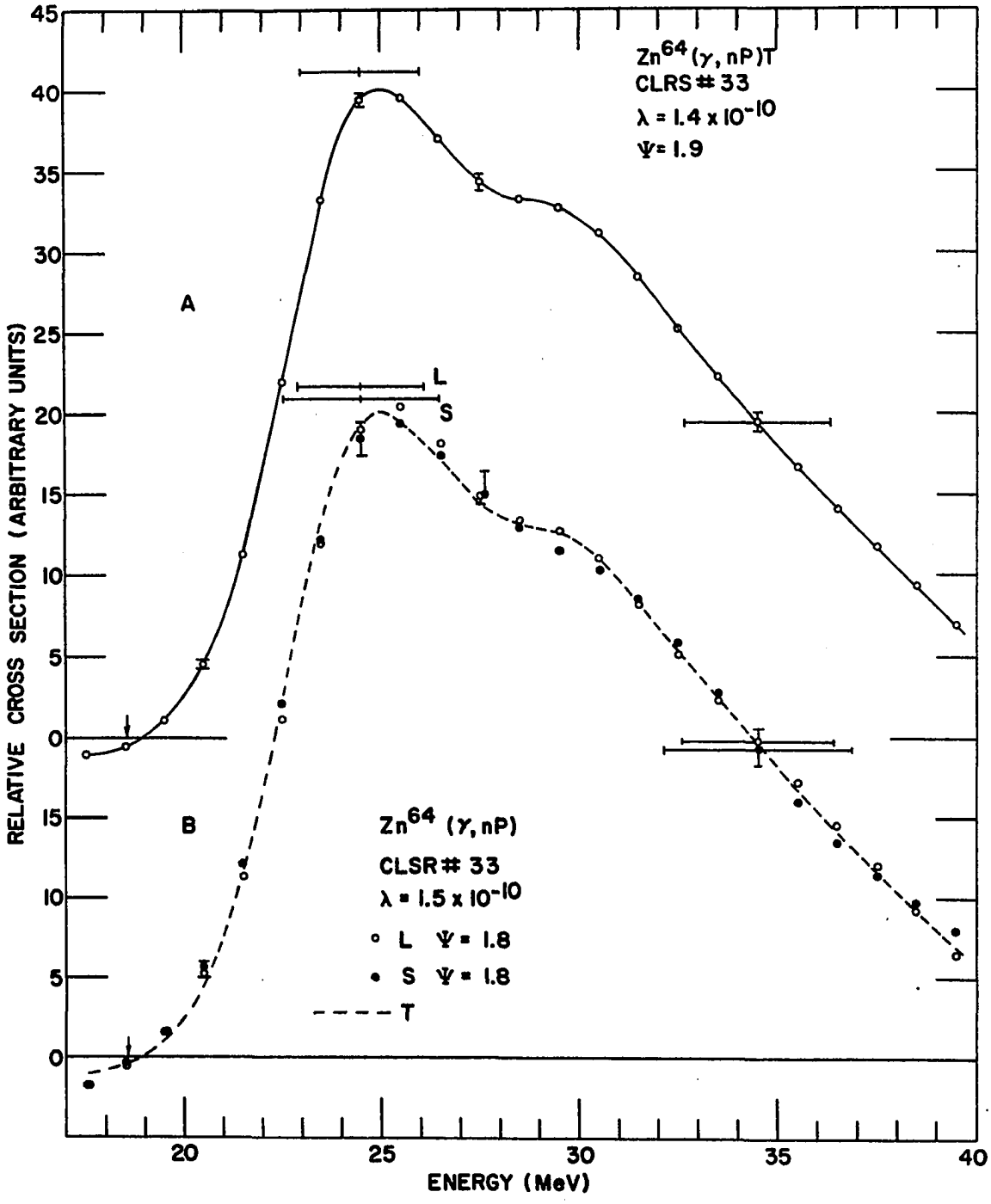
$Zn^{64}(\gamma, nP)T$
CLRS # 33
$\lambda = 1.4 \times 10^{-10}$
$\Psi = 1.9$
A
L
S
B
$Zn^{64}(\gamma, nP)$
CLSR # 33
$\lambda = 1.5 \times 10^{-10}$
○ L $\Psi = 1.8$
● S $\Psi = 1.8$
---- T
RELATIVE CROSS SECTION (ARBITRARY UNITS)
ENERGY (MeV)
45
40
35
30
25
20
15
10
5
0
15
10
5
0
20
25
30
35
40

Figure 13. $Zn^{64}(\gamma,np)$ cross section curves obtained for the same smoothing parameter with several data groupings. (a) the normally smoothed curve using all data. The broken line is the curve of Figure 12a included for reference. (b) Separate undersmoothed analyses of the LONG and SHORT run data. The large statistical errors in the SHORT run data do not allow good resolution above 25 mev. (c) Three independent curves analyzed from composites of the LONG and SHORT run data. The L(2)+S(2) curve is oversmoothed for this value of λ, the other curves are undersmoothed. The LONG and SHORT configurations are summarized in Table 1.

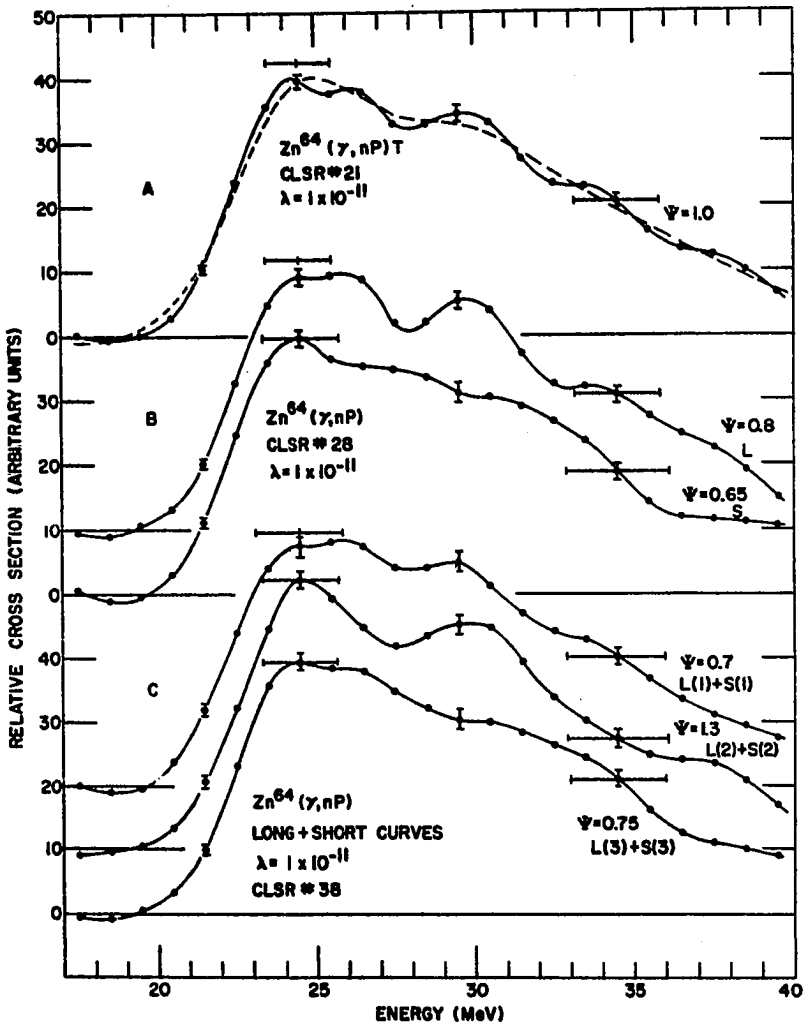
RELATIVE CROSS SECTION (ARBITRARY UNITS)
ENERGY (MeV)
A
Zn^{64} (γ, nP) T
CLSR#21
λ = 1 x 10⁻¹¹
Ψ=1.0
B
Zn^{64} (γ,nP)
CLSR#28
λ = 1 x 10⁻¹¹
Ψ=0.8
L
Ψ=0.65
S
C
Zn^{64} (γ,nP)
LONG + SHORT CURVES
λ = 1 x 10⁻¹¹
CLSR#38
Ψ=0.7
L(1)+S(1)
Ψ=1.3
L(2)+S(2)
Ψ=0.75
L(3)+S(3)

Figure 14. Cross section curves for the $Zn^{64}(\gamma,2n)$ reaction. The full circles indicate the cross section obtained when the competing Cu^{61} and Cu^{64} activities are subtracted from the data. Open circles indicate the results with no correction. Only the LONG configuration data (1 hour bombardment and 20 hour count) has been used. (a) over-smoothed, (b) normally smoothed.

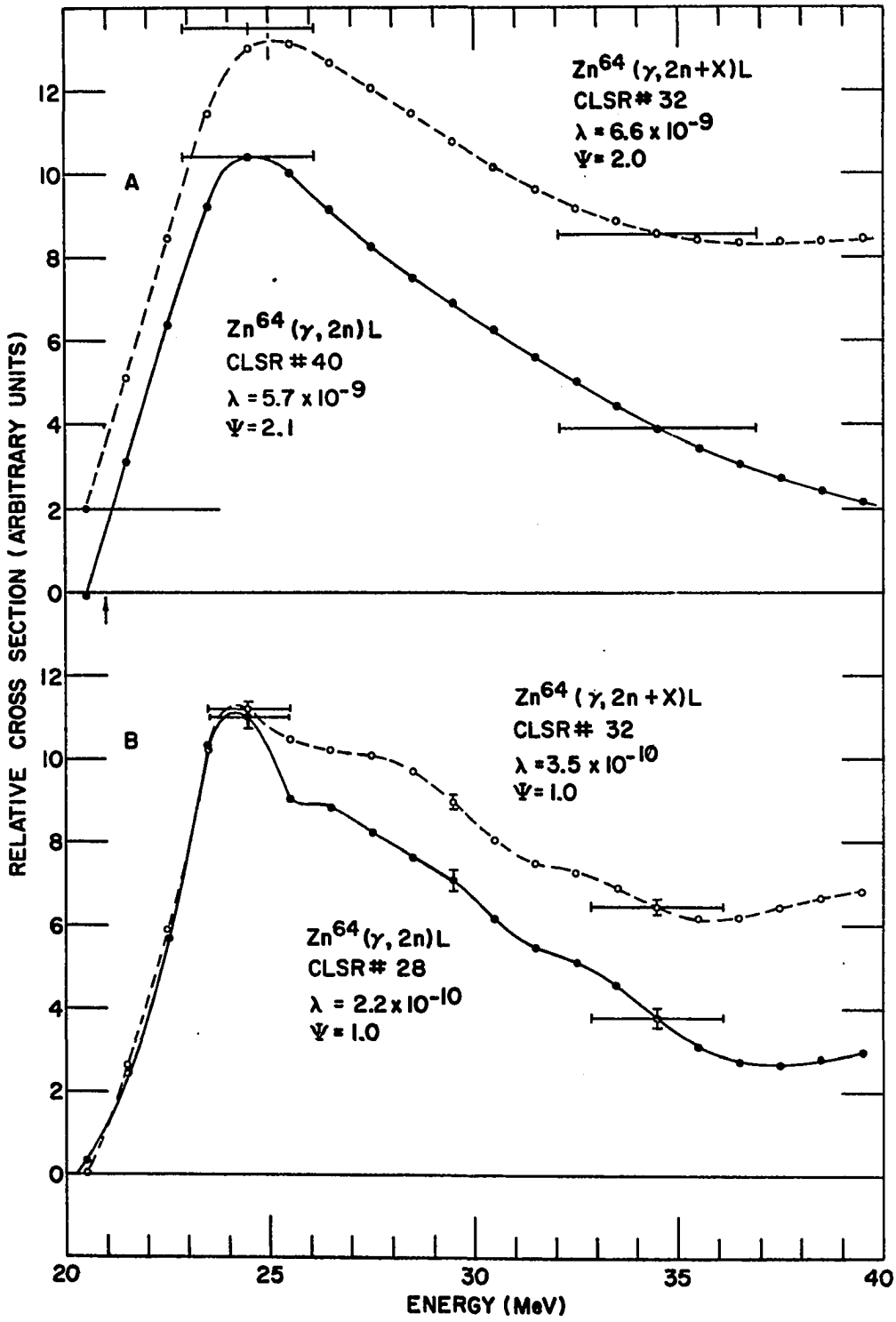
A
$Zn^{64}(\gamma, 2n+X)L$
CLSR# 32
$\lambda = 6.6 \times 10^{-9}$
$\Psi = 2.0$
$Zn^{64}(\gamma, 2n)L$
CLSR # 40
$\lambda = 5.7 \times 10^{-9}$
$\Psi = 2.1$
B
$Zn^{64}(\gamma, 2n+X)L$
CLSR# 32
$\lambda = 3.5 \times 10^{-10}$
$\Psi = 1.0$
$Zn^{64}(\gamma, 2n)L$
CLSR# 28
$\lambda = 2.2 \times 10^{-10}$
$\Psi = 1.0$
RELATIVE CROSS SECTION (ARBITRARY UNITS)
ENERGY (MeV)
0
2
4
6
8
10
12
20
25
30
35
40

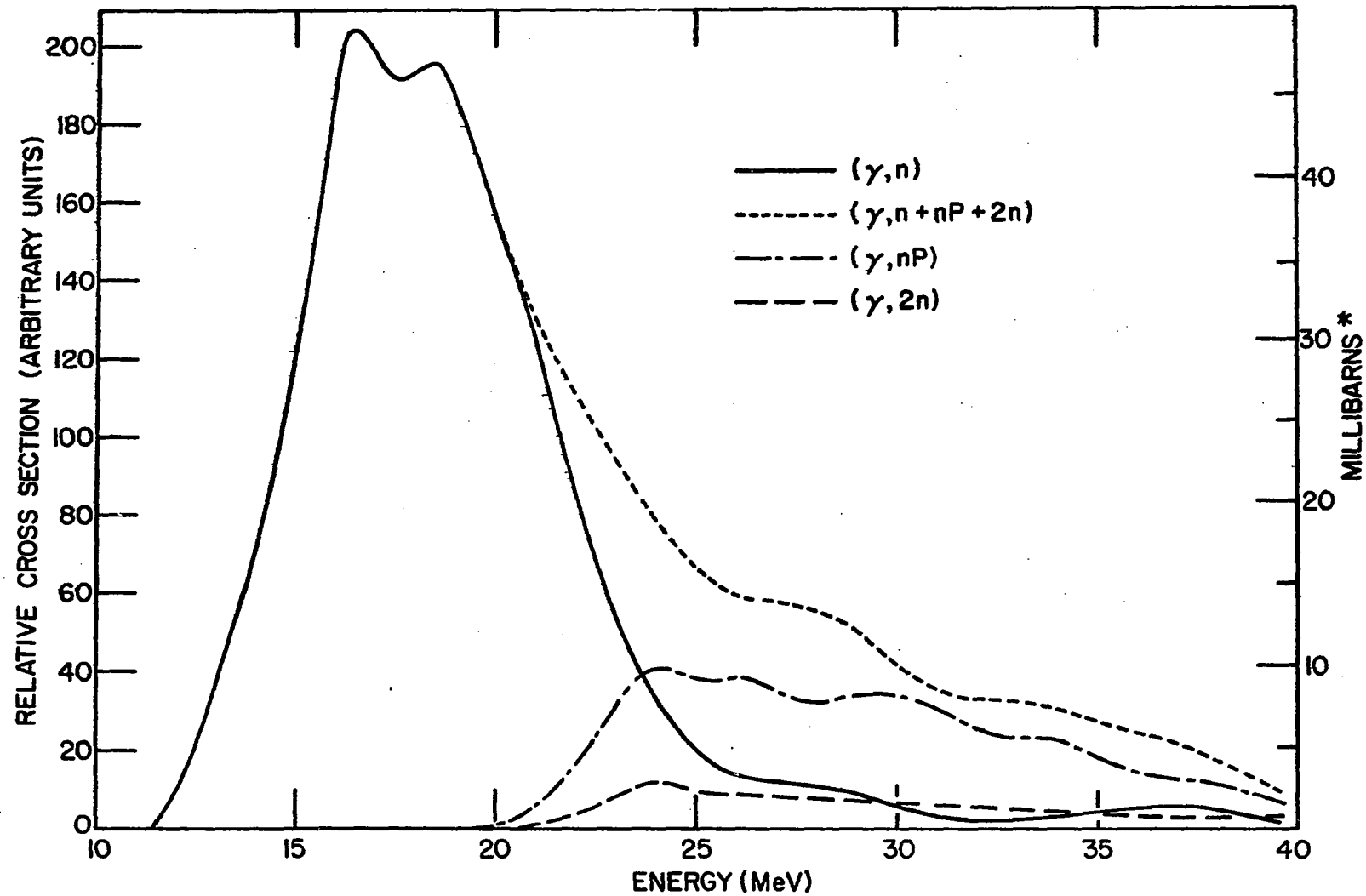

Figure 15. Normally smoothed Zn^{64} cross sections drawn to the same scale. The (γ,n+np+2n) curve has been analyzed by summing the yields for the three reactions. *(The absolute scale is estimated from reference 29.)

convenience, the amount of smoothing is indicated numerically by the quantity Ψ which has the following meaning:

$\Psi = 1$ normal smoothing,

$\Psi < 1$ undersmoothed,

$\Psi > 1$ oversmoothed.

The vertical error bars shown on the figures indicate the uncertainty in the cross section as computed by the CLSR routine. It is the nature of the least structure method that the smoothed solution is properly represented by a smooth curve passing through the values, not the smoothest curve which can be drawn through the error bars. Thus, the error bars indicate the overall, rather than the local, uncertainty in the solution. It will also be noted that the size of the error bars decreases with increased smoothing; that is, the error bars indicate the amount of uncertainty in the solution specific to the amount of smoothing. In the case of oversmoothed curves, for example, small error bars do not mean that larger local structure does not exist in the "true" solution but only that independent measurements, similarly oversmoothed, can be expected to fall within the limits indicated by the error bars.

The horizontal error bars do not indicate uncertainty in the position of structure, but rather, the full width at half maximum to which a delta-function resonance would be smoothed by the analysis.

Since the σ_i values represent an average over the energy interval $E_i - \Delta E$ to E_i (ΔE = 1 mev) all values are plotted in the center of the intervals; this is not rigorously accurate, but sufficient for presentation of the results.

The vertical scales of all of the cross sections are given in terms of

"arbitrary units: which are proportional to the units of the reduced yield measurements. No attempt was made in this experiment to obtain an absolute efficiency calibration of the detectors so that the absolute cross sections were not computed. The reduced yield curves, and hence, the computed cross sections are all proportional to an absolute scale with the same constant of proportionality. Thus the cross section amplitudes may be directly compared from the indicated scales of the figures.

Zinc 64 (γ,n) cross section

The Zinc 64 (γ,n) cross section is displayed in Figure 11a,b,c illustrating normal, undersmoothed, and oversmoothed treatment of the data respectively. In all three cases the reduced yield data is the same.

The (γ,n) yield curve was very precisely determined over the giant resonance region, as would be expected from the very small total errors of the yield curve measurement (less than .4% on the average, cf. Table 3). The excellent reproducibility of the (γ,n) measurement is indicated by the fact that the L, S, and T curves, when analyzed with $\lambda = 0$ (unsmoothed) all reproduced the same details of the (γ,n) cross section up to 23 mev. Above this energy, all three curves oscillate violently from point to point, as is typical of an unsmoothed analysis above the giant resonance. The negative-going oscillations in the undersmoothed curve of Figure 11b are also typical of undersmoothed analysis.

The splitting of the major resonance is almost certainly a reflection of structure in the giant resonance, but details of the splitting are averaged out over the intervals; more will be said in this regard later. The broad shelf from about 26 to 30 mev, which is indicated in Figure 11a, is apparently a true physical feature since it consistently appears in the

analysis of the L and S curves also. The broad peak at 37 mev also may represent a small amount of cross section strength in this region but the evidence is less conclusive. It should be noted at this point that "truncation effects" can cause non-physical distortion of the cross section at either extreme of the cross section curve. Such effects result because the end point data cannot be properly smoothed with adjacent data and small errors in the measured yield may thus generate deflections in the cross section. For this reason, features of the cross section near 40 mev and for the first few points of the curve cannot be directly interpreted as physical effects. The effect of such distortions should be negligible beyond the extent of a "smoothing width" (as indicated by the horizontal bars). Note that the least structure solution may also be distorted at the reaction threshold. This is a result of the internal smoothing -- the sharp "break" at threshold is smoothed into a gradual "bend" which may result in non-physical strength at threshold (cf. Figure 11c) or a negative going oscillation below threshold (cf. Figure 11a). For this reason, reaction thresholds are best determined from the yield curves themselves.

Zinc 64 (γ,np) cross section

The $Zn^{64}(\gamma,np)$ cross section results are displayed in Figures 12 and 13. Since the purpose of this measurement is only to determine the energy distribution and overall strength of the cross sections, consideration of the oversmoothed solutions is most appropriate to the discussion. Figure 12a is the oversmoothed least structure solution of the T (LONG and SHORT run) curve and Figure 12b shows the results of separate analysis of the L and S curves. Approximately the same value of λ (smoothing parameter) was used for the analysis of all three curves, which results in roughly the same

smoothed widths for all three curves. The agreement of the separate analyses is excellent as the shape and magnitude of the curves agree within the indicated errors. It should be emphasized that nowhere in analysis were the L and S curves "normalized" to each other so the excellent agreement of the curves is very strong evidence of the reliability of the measurement. The important features of the (γ,np) cross section are clearly observed in Figure 12:

a) the cross section rises rapidly to a broad maximum at 25 mev,

b) the amplitude of the (γ,np) cross section at maximum is about 20% of the (γ,n) giant resonance amplitude (cf. Figure 11c),

c) there is a shoulder at about 30 mev which falls off slowly to 40 mev.

The overall shape of the (γ,np) cross section strongly suggests a broad major resonance centered at 25 mev and a weaker secondary resonance which peaks at about 30 mev and then falls off slowly.

Although the oversmoothed results presented in Figure 12 are adequate for the purposes of this experiment, it is interesting to examine the data analyzed with less smoothing. Figures 13a,b,c represent the normally smoothed and undersmoothed results obtained from several data groupings. Figure 13a is the normally smoothed cross section obtained from the analysis of the (γ,np) T curve (all data). The undersmoothed L and S curves, separately analyzed are shown in Figure 13b. Figure 13c is composed of 3 curves, each of which is the average of one complete S curve and one L curve (recall that three complete yield curves were measured for both the LONG and SHORT run sequences); these three composite curves are labeled as L(1) + S(1),

L(2) + S(2), and L(3) + S(3) in a natural manner. The curves of Figures 13b and 13c were analyzed with the same λ as for 13a; this typically results in undersmoothed curves but the smoothed widths are then roughly equal.

It is necessary to make some further remarks about the relative precision of the L and S curves. Due to the smaller amount of activity created in the SHORT run bombardments, the statistical uncertainty in the separate S yield measurements is larger than for the L measurements. Since there are twice as many S as L measurements in the 18 to 25 mev region, the average errors (curve errors) are comparable for these energies. The curve error in the 26 to 39 mev region, where both sets have an equivalent number of runs, is considerably worse for the S than for the L curve (this difference is not obvious in the parameters quoted in Table 3 since $\sqrt{\epsilon}$, $\overline{\delta}$, and Q are formed by a weighted average and yield points with large curve errors are not weighted as heavily). Thus possible structure in the 26 to 39 mev region of the S curve is "smeared out" by the large statistical errors.

It is noted that for all the curves of Figure 13 the cross section now peaks at 24.5 mev and the single broad 25 mev resonance of Figure 12 now shows evidence of splitting. The splitting is evident in 13a, in the L curve of 13b, and the L(1) + S(1) and L(3) + S(3) curves of Figure 13c. As has been remarked above, the S curve of 13b is not well resolved above 25 mev, but the 24.5 mev peak is well resolved and there is indication of strength at 26 mev. The L(2) + S(2) curve of 13c is actually oversmoothed for this λ; when examined under normal smoothing, a very strong peak at 24.5 mev is seen and also a weaker peak at 26 mev. Obviously, the energy

increments of this experiment are too large to adequately resolve such structure and the splitting in the 24.5 to 26 mev region of Figure 13 can only be regarded as a gross indication of the physical behavior, but it appears quite likely that pronounced structure would be seen in this region if measured with smaller increments.

The inflection at 27 mev and shoulder at about 30 mev also seem to be consistently indicated within the precision of the measurements. There is an indication of additional structure in the "tail" of the curve, but the evidence is somewhat more tenuous.

The six individual curves L(1), L(2), L(3), S(1), S(2), S(3) were also analyzed (not shown) and again, within the limitations of the poor statistical situation for the individual curves, were consistent with the above discussion. Most notably, the 24.5 mev peak was clearly indicated in all cases.

A very significant result of the measurement is seen in the yield curve for the (γ,np) reaction (Figures 7 and 9) where it is observed that the reaction threshold occurs at approximately 21 mev, about 2.5 mev above the energetic threshold for the (γ,np) process.

Zinc 64 (γ,2n) cross section

The oversmoothed and normally smoothed Zn^{64}(γ,2n) cross section curves are given in Figure 14 (solid line) and the comparably smoothed Zn^{64} (γ,2n + x) cross section curves are also displayed (broken line) for reference. Only the L curves are shown since the uncertainty in the S curve measurement is too large for meaningful analysis (cf. Table 3). The normally smoothed S curve was analyzed and agrees with the oversmoothed (γ,2n) curve of 14a; in particular, the 24.5 mev peak is clearly seen. The

normally smoothed curves of Figure 14b both indicate a narrow peak at about 24.5 mev. For the $(\gamma,2n)$ curve the peak is especially pronounced. The sharpness of this peak could be a consequence of systematic error in the subtraction of the $Cu^{64}(Zn^{66}[\gamma,np])$ positron yield from the data, however the undersmoothed $Zn^{66}(\gamma,2n + x)$ curve shows an equally sharp peak for the same λ.

The important features of the $(\gamma,2n)$ cross section are:

a) the cross section rises sharply from the energetic threshold of 21 mev,

b) the maximum occurs at about 24.5 mev and is only about 28% (certainly less than 1/3) of the amplitude of the (γ,np) cross section at maximum amplitude,

c) the cross section falls relatively smoothly and slowly to 40 mev.

It should be noted that the accuracy of the above statements is not significantly affected by the degree of smoothing employed nor by the details of the subtraction of the competing (Cu^{61} and Cu^{64}) long-lived positron activities.

Comparison of the Zinc 64 (γ,n), (γ,np) and $(\gamma,2n)$ cross sections

The Zinc 64 (γ,n), (γ,np), $(\gamma,2n)$, and $(\gamma,n + np + 2n)$ cross sections are drawn to the same scale in Figure 15. Normally smoothed curves have been drawn in all cases to facilitate comparison. The $(\gamma,n + np + 2n)$ curve was obtained by analysis of the yield curve resulting from the sum of the reduced yield curves [$(\gamma,n)T$, $(\gamma,np)T$, and $(\gamma,2n)L$] used in the analysis of the individual reaction cross sections (the curve error was obtained by standard error addition of the separate curve errors). Essentially the

same curve is obtained if the cross section curves for the (γ,n), (γ,np), and $(\gamma,2n)$ reactions are added directly. The deflection at about 29 mev in the $(\gamma,n + np + 2n)$ curve is apparently caused by the relatively strong deflection in the (γ,n) curve at this energy. The (γ,np) cross section accounts for most of the strength above 24 mev.

The approximate cross section strength in millibarns is indicated in the right margin of Figure 15. This absolute scale was estimated from the recent $Zn^{64}(\gamma,n)$ cross section measurement by Owen, Muirhead, and Spicer (29).

Comparison with Other Experiments

Zinc 64 (γ,n)

The results of this measurement of the $Zn^{64}(\gamma,n)$ cross section are compared in Figure 16 with three absolute cross section measurements reported elsewhere. For this comparison the $\lambda = 0$ (unsmoothed) $Zn^{64}(\gamma,n + np + 2n)$ and $Zn^{64}(\gamma,n)$ cross sections have been given. As has been remarked earlier, the errors in the (γ,n) cross section are sufficiently small to give meaningful unsmoothed results up to about 24 mev and the same situation holds for the $(\gamma,n + np + 2n)$ curve. Each of the other measurements was performed to 23 or 24 mev, also using bremsstrahlung radiation.

The recent $Zn^{64}(\gamma,n)$ measurement by Owen, Muirhead, and Spicer (29) was by activation of natural zinc samples and detection of the positron activity. The bremsstrahlung energy was incremented in steps of 100 kev so that structure is well resolved. The analysis was performed using the Penfold, Leiss procedure and the curve shown in Figure 16 is a smoothed result as quoted by the authors. The integrated cross section to 23 mev was measured to be 360 mev-mb.

Figure 16. Comparison of the $Zn^{64}(\gamma,n)$ cross section as measured in this experiment and others. Open circles indicate the (γ,n) cross section and full circles indicate the $(\gamma,n+np+2n)$ result analyzed from the summed yields, both curves are unsmoothed for comparison. The result of Costa *et al.* is for natural zinc. The results of this experiment have been normalized to the integrated cross section reported by Owen *et al.*, the other curves are drawn to their absolute scale.

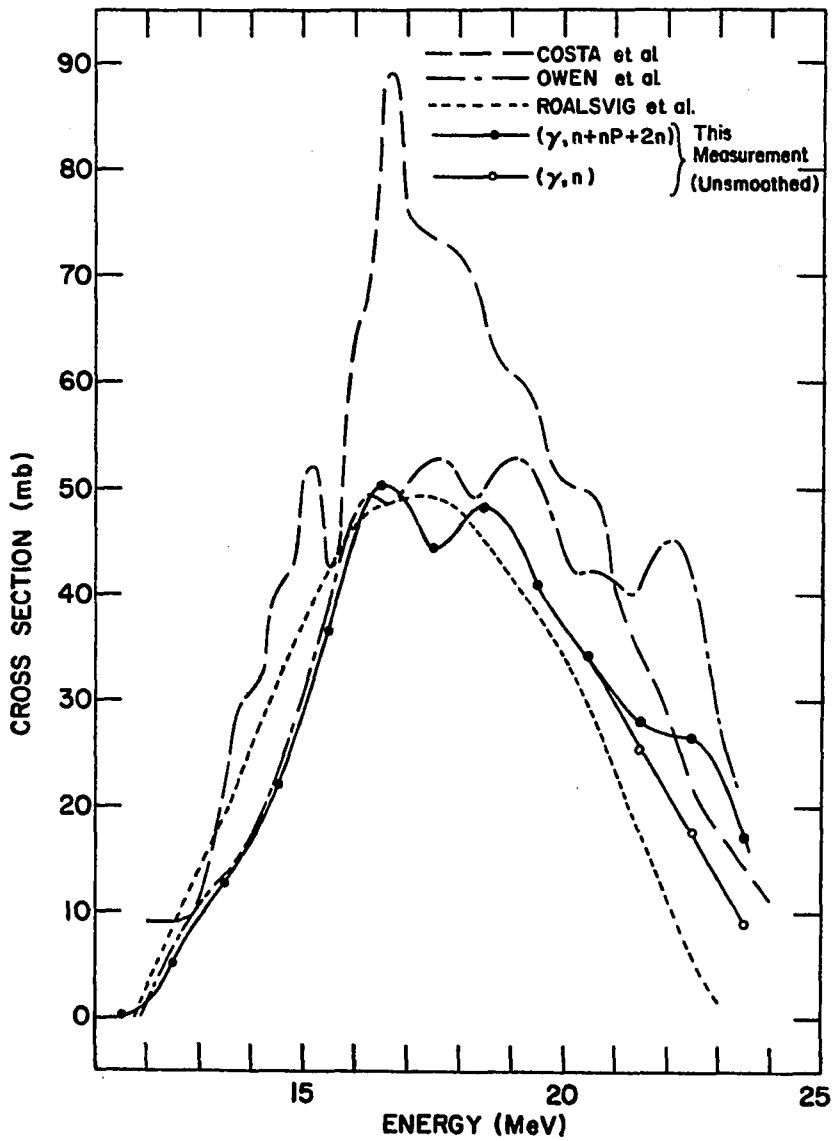
COSTA et al
OWEN et al
ROALSVIG et al.
(γ,n+nP+2n)
(γ,n)
This Measurement (Unsmoothed)
CROSS SECTION (mb)
ENERGY (MeV)
0
10
20
30
40
50
60
70
80
90
15
20
25

Costa et al. (30) have measured the total neutron cross section for natural zinc by direct neutron detection. The bremsstrahlung energy was varied in steps of 250 kev and the least structure method was used for the cross section solution. The measured cross section is $\sigma(\gamma,Tn) = \sigma(\gamma,n) + 2\sigma(\gamma,2n) + \sigma(\gamma,np)$. The neutron multiplicity of the $(\gamma,2n)$ reaction was corrected for on the basis of a statistical model and the curve shown represents the $(\gamma,n) + (\gamma,np) + (\gamma,2n)$ cross section for natural zinc (the results presented by Costa have been smoothed somewhat for Figure 16). Since all zinc isotopes contribute to this cross section, comparison with the Zn^{64} cross sections cannot be direct, but it is reasonable to expect that some of the features of the Zn^{64} cross section are also common to the other isotopes.

Roalsvig, Haslam, and Bergsteinsson (31) measured the $Zn^{64}(\gamma,n)$ yield by the activation method. The cross section was obtained by the Penfold, Leiss method. The integrated cross section to 23 mev is given as 330 mev-mb.

For purposes of comparison, the integrated $(\gamma,n + np + 2n)$ cross section for the present measurement has been normalized to the value of 360 mev-mb. as determined by Owen. Using this number, the normalization factor for (arbitrary) units to absolute cross section is estimated to be .24 mb/unit. The results of this experiment given in Figure 16 have been scaled by this factor.

On the leading edge of the giant resonance, this experiment shows excellent agreement with that of Owen. The measurement of Roalsvig gives reasonable overall agreement if his curve is shifted upwards by .5 mev. The peaks at 16.2, 17.5, and 19 mev in the curve of Owen are also indicated

by that of Costa but the relative strengths are considerably different. It is believed that this structure has been averaged in the present measurement to produce the observed splitting. A small resonance is observed at 20.5 mev in the data of both Owen and Costa and also appears as a small deflection in the present results. The strong peak at 27 mev in the results of Owen appears to be weakly reproduced in the data of Costa, but is not apparent in the $Zn^{64}(\gamma,n)$ curve from this measurement. This peak does appear to have an analog in the fairly large shoulder seen in the $(\gamma,n + np + 2n)$ curve. Owen states that no evidence of the 9.8 min. Cu^{62} (Zn^{64} $[\gamma,np]$) activity was observed following irradiation at 24 mev (28) and this activity was therefore not corrected for in the experiment. Indeed, the $Zn^{64}(\gamma,np)$ yield is seen to be only about 2% of the (γ,n) yield at 24 mev, but this small amount of activity could introduce such a resonance, particularly if the bombardment times were short and the activity was counted immediately after bombardment. Roalsvig waited 20 minutes before counting so the effect of the Cu^{64} activity would be minimized in his experiment.

The area of the cross section curve, as given by Owen, appears to be larger (about 400 mev-mb) than the 360 mev-mb value quoted and Owen's curve thus is considerably larger than the present result (normalized to 360 mev-mb) above 17 mev. This may be a consequence of the method of analysis if the technique does not preserve area under the curve.

In summary, the shape of the $Zn^{64}(\gamma,n)$ cross section obtained in this measurement appears to agree quite well with these other measurements when allowances are made for the large energy increments of this experiment.

There are also several earlier measurements of the (γ,n) cross

sections reported. Katz and Cameron (26) display a cross section curve to 24 mev which peaks at 18.5 mev with maximum cross section of 120 mb. Katz et al. (32) later recalculated this measurement by the photon difference method and report the peak to be at 18.7 mev and 124 mb. Marshall (33) measured the absorption cross section and gives an integrated cross section to 50 mev of 770 mev-mb. Montalbetti, Katz, and Goldemberg (34) measured the total photoneutron cross section for natural zinc by direct neutron detection and found the cross section to peak at 18.7 mev and 120 mb. Gavrilov and Lazareva (35) also employed direct detection of neutrons from natural zinc and observed a strong (82 mb) peak at 16.3 mev. The integrated cross section to 27 mev is reported as 660 mev-mb.

Several authors (36,37,38,39,40,41) report measurements of the Zn^{64} (γ,n) cross section using the gamma rays from the $Li^{7}(p,\gamma)$ reaction. Such measurements typically imply a cross section of about 50 mb at 17.6 mev. Since the spectrum of the Li^{7} gamma rays consists of only two lines (14.8 and 17.6 mev) and is thus better known than the bremsstrahlung spectrum, this method should in principle be more accurate for absolute cross section determination. It is thus encouraging to note that this value is in reasonable agreement with the bremsstrahlung measurements of both Owen and Roalsvig.

Cross section ratios

A few earlier measurements of the relative (γ,n), $(\gamma,2n)$, and (γ,np) cross sections are reported in the literature. There are also several reported measurements of the relative or absolute $Zn^{66}(\gamma,np)$ cross section.

Sagane (42) measured the relative cross sections of the $Zn^{64}(\gamma,n)$, (γ,np), and $(\gamma,2n)$ cross sections with bremsstrahlung. Few experimental

details are given but it can be inferred from similar measurements by the author (43,44) that the $Cu^{63}(\gamma,n)Cu^{62}$ reaction was used as a monitor reaction in lieu of direct measurement of the bremsstrahlung dose. The activities were apparently separated by halflife. Relative cross section curves are given and peak at 18.28, and 28 mev respectively, and the ratios of the cross section maxima are $(\gamma,np)/(\gamma,n)$ = 30% and $(\gamma,2n)/(\gamma,np)$ = 23% as compared to about 20% and 30% for the same ratios from this experiment. The relative integrated cross sections are given, presumably to 67 mev. The errors in this measurement are apparently quite large, ranging from 50% in the case of the (γ,n) measurement, to 20% in the case of the $(\gamma,2n)$ measurement.

El Sioufi, Erdös, and Stoll (45) and Hofmann and Stoll (46) report measuring the $Zn^{66}(\gamma,np)$ and $Zn^{64}(\gamma,np)$ absolute cross sections with bremsstrahlung. Again, copper reactions were used to monitor the reactions and obtain an absolute cross section scale. The Cu^{64} product of the zinc 66 reaction was separated chemically prior to counting. The integrated cross sections to 32 mev are given as 30 $\pm$ 10 mev-mb and 31 $\pm$ 8 mev-mb for the $Zn^{64}(\gamma,np)$ and $Zn^{66}(\gamma,np)$ reactions respectively. A cross section curve for the $Zn^{66}(\gamma,np)$ reaction is given which is in general agreement with the conclusions drawn regarding this reaction in Chapter III; in particular, the cross section peaks at about 28 mev and has nominal strength below 24 mev.

Strauch (47) measured transition curves with lead absorbers and 322 mev bremsstrahlung for the reactions $Zn^{64}(\gamma,n)$, (γ,np), and $(\gamma,2n)$ and $Zn^{66}(\gamma,np)$. The reactions were separated by halflife. Relative integrated cross sections were computed and are said to have uncertainty of about 25%.

Edwards and Macmillan (48) measured integrated cross sections with bremsstrahlung. The $C^{12}(\gamma,n)$ reaction was used as a monitor reaction. The activities were separated from the decay curve. The integrated cross sections are given as $Zn^{64}(\gamma,n)$ = 600 mev-mb, $Zn^{64}(\gamma,np)$ = 120 mev-mb, $Zn^{64}(\gamma,2n)$ = 34 mev-mb, and $Zn^{66}(\gamma,2n)$ = 310 mev-mb.

The ratios of the integrated cross sections from the above, as well as the present measurement are summarized in Table 4. The measurements of Sagane and Strauch are seen to give reasonable agreement with the present results when allowance is made for the size of the errors and the differences in endpoint energy. The results of Edwards and Macmillan seem to agree relatively well except that the $Zn^{66}(\gamma,np)$ cross section is much larger than the present experiment indicates. Estimating the absolute cross section scale for this experiment from the $Zn^{64}(\gamma,n)$ result of Owen implies a $Zn^{64}(\gamma,np)$ integrated cross section of about 82 mev-mb and about 35 mev-mb for $Zn^{66}(\gamma,np)$ (both taken to 32 mev). The latter is in fair agreement with that of Hofmann and Stoll but the difference in the $Zn^{64}(\gamma,np)$ cross section is quite large.

If the results of the various experiments are taken at face value, it can be inferred that the two (γ,np) integrated cross sections are increasing with energy, at least relative to the (γ,n) and $(\gamma,2n)$ cross sections. This is not inconsistent with the results of Van Hise, Meyer, and Hummel (49) who measured the integrated $Zn^{66}(\gamma,np)$ cross section from 50 to 300 mev and found that it smoothly increased from 128 to 400 mev-mb in this range.

As pointed out by Spicer (50) there is a regretable tendency for each laboratory to report different absolute cross section measurements and a

Table 4. Ratio of integrated cross sections

Author	Relative or Absolute	$\frac{Zn^{64}(\gamma,np)}{Zn^{64}(\gamma,n)}$	$\frac{Zn^{64}(\gamma,2n)}{Zn^{64}(\gamma,np)}$	$\frac{Zn^{66}(\gamma,np)}{Zn^{64}(\gamma,np)}$	E_{max}
Sagane (42)	Relative	.33	.23		67 mev(?)
Strauch (47)	Relative	.42	.18	.51	322 mev
Edwards and Macmillan (48)	Absolute	.20	.28	2.6	50 mev(?)
Hofmann and Stoll (46)	Absolute			1.0	32 mev
Schamber	Relative	.23	.24	.32	32 mev
Schamber	Relative	.30	.23	.41	40 mev

major part of the blame for this inconsistency can be given to the technique of obtaining absolute cross section scales from so called "standard" cross sections. In the case of several of the experiments discussed above, the cross section was calculated by inference from the copper cross sections. Such a procedure can result not only in erroneous absolute cross section values, but could also alter the relative magnitudes of the various reactions. For this reason, it is felt that direct measurement of the dose, as performed in this experiment, should be a more accurate method for obtaining the relative cross sections than the use of a "monitor" reaction.

Integrated cross sections

The relative integrated cross sections measured in this experiment are indicated in Figure 17 (the scale is logarithmic). The estimated absolute cross section scale, again based upon the value of Owen, Muirhead, and Spicer (29) is indicated in the right hand margin. The ratios of the (γ,n), (γ,np), and $(\gamma,2n)$ integrated cross sections to the $(\gamma,n + np + 2n)$ cross section to 40 mev are 73%, 22%, and 5% respectively. An upper limit on the integrated $(\gamma,2n)$ to $(\gamma,n + np + 2n)$ ratio is 7% [based on the $(\gamma,2n + x)$ integrated cross section].

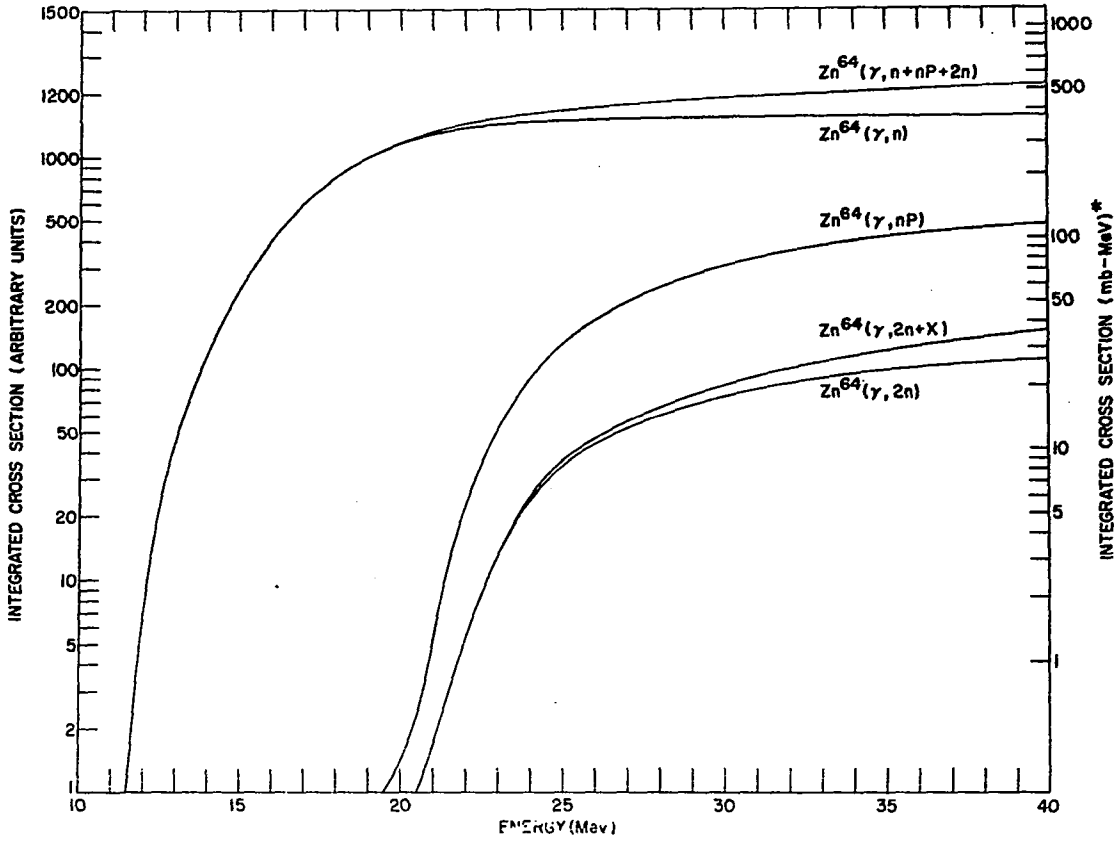

Figure 17. Relative integrated cross sections from this experiment. The scale is logarithmic. The $(\gamma,n+np+2n)$ curve was obtained by summing the yields. The $(\gamma,2n+x)$ curve represents $(\gamma,2n)$ strength plus strength from competing long activities. *(The absolute scale has been estimated from reference 29.)

CHAPTER V. CONCLUSIONS

In the preceding chapter, the results of this experiment were presented and the features of the cross sections discussed without reference to the reaction mechanism. In this chapter, the results of this experiment shall be considered as evidence of the isobaric spin splitting of the Zn^{64} giant resonance.

Review of Findings

The major results of this experiment are here summarized for reference:

1) The (γ,np) cross section amplitude is at least three times larger than the (γ,2n) cross section.
2) The (γ,np) cross section is segmented into a strong and distinct resonance centered at 25 mev and a smaller high energy tail.
3) The (γ,np) cross section is about 20% of the (γ,n) cross section at maximum amplitude.
4) The (γ,np) reaction accounts for about 20% of the integrated Zn^{64}(γ,n) + (γ,np) + (γ,2n) cross section to 40 mev and represents about 50% of this strength between 21 and 40 mev.

Evidence of Isospin Splitting of the Zn^{64} Giant Resonance

In Chapter II it was estimated that the $T_>$ giant resonance component should occur at about 25 mev, or about 7 mev above the $T_<$ giant resonance and account for something on the order of 20-40% of the total integrated cross section. It was also shown that, due to the effect of the isospin selection rules, a significant fraction of the $T_>$ strength should be

observed in the (γ,np) reaction channel. On this basis, it is then reasonable to postulate that the large and distinct cross section peak centered at 25 mev in the (γ,np) cross section is to be identified with the $T_>$ giant resonance component and the main resonance in the (γ,n) cross section represents the $T_<$ component alone. Evidence in support of this identification will now be discussed in detail.

Non-statistical strength in the (γ,np) channel

As discussed earlier, comparison of the relative (γ,np) and $(\gamma,2n)$ strengths is a major indicator of the probable reaction mechanism responsible for the (γ,np) cross section. In particular, a statistical evaporation process would imply that the (γ,np) and $(\gamma,2n)$ reactions compete on a roughly equal basis, the coulomb barrier favoring the two-neutron process. Since the (γ,np) threshold is somewhat lower than the $(\gamma,2n)$ threshold it might be assumed that the additional energy available for np decay might somewhat offset the coulomb barrier retardation. It is well known that in light nuclei, the large energy difference between (γ,n) and (γ,p) thresholds does indeed tend to compensate for the coulomb enhancement of the (γ,n) process, however, the coulomb barrier plays an increasingly dominant role as the atomic number is increased. Assuming that a somewhat analogous situation pertains for the (γ,np) and $(\gamma,2n)$ reactions, the coulomb barrier should be at least as important as the small np energy excess in determining the ratio of these reactions; in short, a purely statistical model cannot explain the greatly enhanced (γ,np) cross section observed in this experiment. Furthermore, the energy available for ground state decay does not appear to have any relation to the observed distribution of (γ,np) and $(\gamma,2n)$ strengths. Whereas the $(\gamma,2n)$ cross section rises rapidly to its

maximum within 4 mev of the $(\gamma,2n)$ threshold, there is no appreciable (γ,np) strength until about 2-3 mev above the (γ,np) threshold, moreover, the two reactions both achieve maximum amplitude at about the same energy and it is not until about 40 mev that their cross sections become comparable. It is thus quite clear that the (γ,np) cross section is dominated by a non-statistical process and a reaction sensitive to nucleon charge must be assumed to explain these results.

Shape of the (γ,np) cross section

The pronounced asymmetry of the (γ,np) cross section and the clear minimum at about 28 mev strongly suggest that the cross section for this reaction consists of two components. Even when drastically oversmoothed (cf. Figure 12) the (γ,np) cross section clearly indicates a dominant resonance centered at about 25 mev and a weaker, smoothly-varying component which rises on the trailing edge of the major resonance and extends beyond 40 mev. For less smoothing, the separation is very pronounced (cf. Figure 13) and there is indication of structure in the main peak. The major (γ,np) resonance peak has a shape which is very similar to the (γ,n) resonance peak. For comparison, the (γ,n) and (γ,np) curves have been superimposed in Figure 18. In this figure the (γ,n) curve has been arbitrarily reduced to 20% of its relative magnitude and shifted upwards in energy by 7.7 mev; for the comparison both curves have been slightly oversmoothed to the same smoothing width ($\simeq$ 2 mev) at maximum (ie. the curves are of equivalent resolution). There is seen to be a striking similarity when compared in this manner; the leading edges of the resonances are in excellent agreement, the resonances appear to be of the same width, and there is even a remarkable correlation of the averaged structure in the

Figure 18. Comparison of the $Zn^{64}(\gamma,n)$ and (γ,np) cross sections measured in this experiment. The open circles are the (γ,np) results and the solid curve is the (γ,n) curve shifted upward in energy by 7.7 mev and multiplied by .196. The similarity of these curves to 28 mev supports the identification of the 25 mev (γ,np) peak as due to the $T_>$ giant resonance.

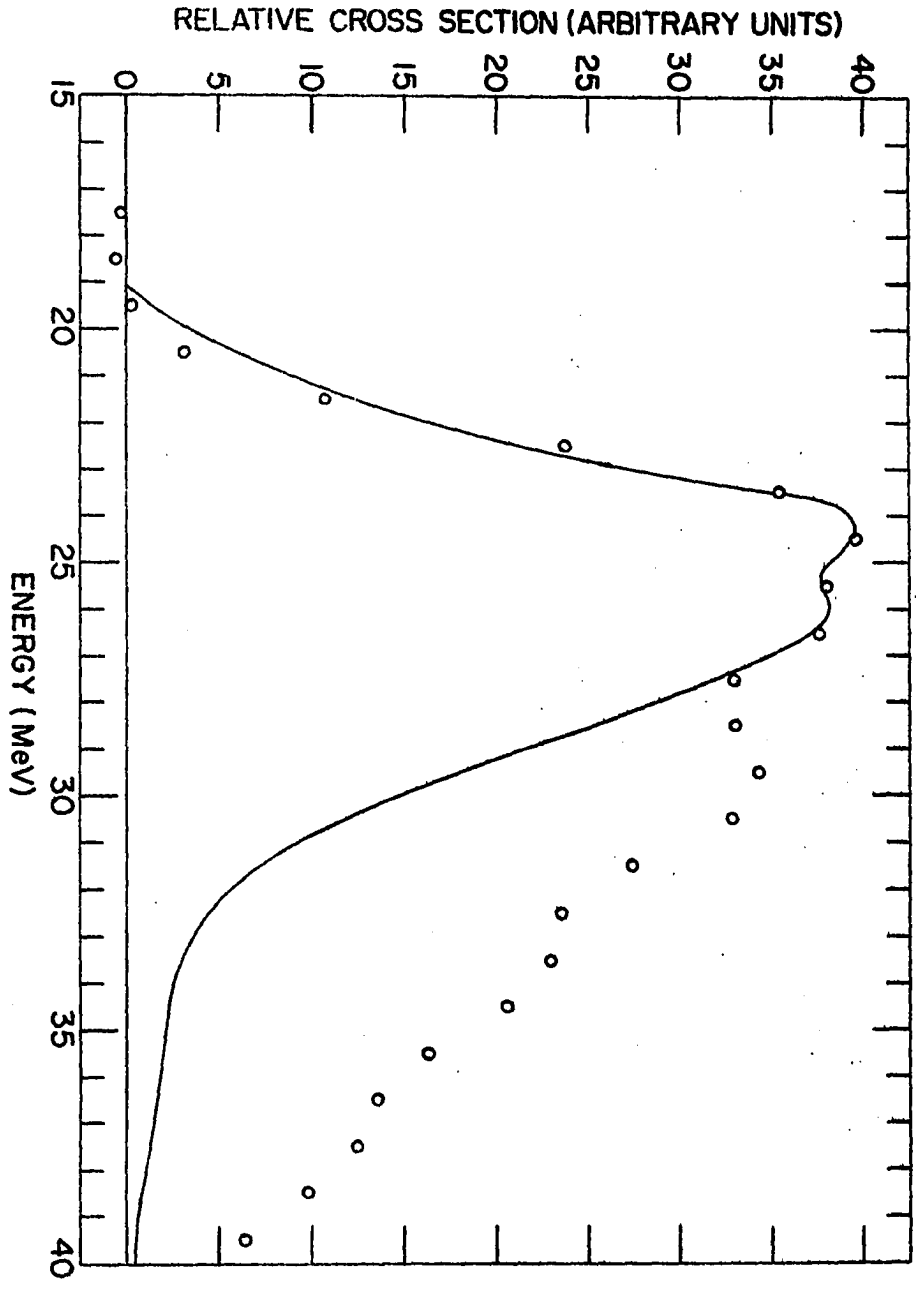
RELATIVE CROSS SECTION (ARBITRARY UNITS)
0
5
10
15
20
25
30
35
40
ENERGY (MeV)
15
20
25
30
35
40

peaks. It must be emphasized with respect to this latter observation that it is not intended to imply that the details of structure in the two peaks are identical. High resolution measurements of the (γ,n) cross section (29) indicate pronounced structure in this region but because of the large (1 mev) energy increments used in this experiment only the averaged structural effects can be seen; the fact that both the 25 mev (γ,np) and the major (γ,n) peaks are seen to be split is thus evidence only of unresolved structure.

The remarkable agreement in shape of these two curves would seem to be more than accidental and is difficult to explain in terms of completely independent (γ,n) and (γ,np) processes. On the other hand, $\Delta T = 0$ and $\Delta T = 1$ excitations are closely related and similar levels should be populated by the two isospin modes of the giant resonance excitation. Thus the striking similarity in distribution of the cross section strength in the (γ,n) and 25 mev (γ,np) resonances is strong evidence that these resonances are properly identified with the $T_<$ and $T_>$ giant resonance components.

It is again emphasized that interest is properly focused on the relative distribution of cross section strength rather than the structural details. In the Zn^{64} case, one is aware that not all of the $T = 5/2$ levels in the residual Zn^{63} nucleus can decay by proton emission and even assuming that the levels populated by the two isospin modes of giant resonance excitation are otherwise identical, completely equivalent (γ,n) and (γ,np) cross sections would not be expected. The important point in the interpretation of Figure 18 is that the envelopes of the two resonances appear to be very similar and thus equivalent gross distribution of cross section strength may be inferred; a high resolution study of the resonance

structure might or might not indicate further similarities.

It is thus not unreasonable to infer that the (γ,np) cross section strength under the solid curve of Figure 18 (20% of the (γ,n) cross section) is primarily due to the $T_>$ giant resonance. The relatively smooth component above the solid curve is then to be associated with some other reaction mechanism.

Other channels for decay of the $T_>$ component

As earlier stated, although the (γ,np) process is the most favorable channel for observation of the $T_>$ component in Zn^{64}, other channels are also possible. Notably, population of the lowest lying T = 5/2 level in Zn^{63} (17.28 mev excitation energy) followed by gamma-dexcitation gives rise to an isospin allowed (γ,n) mode for the $T_>$ giant resonance component. The broad shoulder to about 30 mev in the (γ,n) giant resonance may well be due to this process (cf. Figure 15). Of course, there is no way to determine from these results if such (γ,n) strength is due to isospin allowed (through T = 5/2 levels) or isospin forbidden (eg. ground state) neutron decay, and other excitation modes, such as nuclear quadrupole (E2) might also be considered. The important point is that some fraction of the $T_>$ excitations must populate the particle stable T = 5/2 levels in Zn^{63} and there must thus be some contribution to the (γ,n) cross section from the $T_>$ component. The fact that the (γ,n) cross section shows a significant strength in just the right energy region thus provides corroboration of the model.

The relatively sharp resonance seen at about 24 mev in the $(\gamma,2n)$ cross section (cf. Figure 14b) might be interpreted as due to isospin-forbidden neutron decay from the T = 5/2 levels in Zn^{63}. Such $(\gamma,2n)$

strength would not be totally unexpected since the coulomb potential does differentiate neutrons and protons and thus isospin cannot be a "good" quantum number. There is no clear evidence of increased $(\gamma,2n)$ strength above 26 mev where isospin allowed $(\gamma,2n)$ reactions are possible, but due to the ambiguities resulting from the competition of other long-lived activities and the crude method of correction for these activities, it is not appropriate to infer specific details of the $(\gamma,2n)$ structure from this measurement. It does seem clear, however, that if any of the $T_>$ component is proceeding through the $(\gamma,2n)$ channel it can account for very little (25% at the very most) of the total $T_>$ strength.

One must also remember that the (γ,p) channel is isospin allowed for both giant resonance components. Since the (γ,p) cross section was not measured in this experiment it is not possible to accurately estimate the strength of the $T_>$ component in this channel. It is nonetheless interesting to note the results of the (γ,p) measurement of Osokina and Ratner for natural zinc (51); this measurement indicated a strong resonance in the $Zn(\gamma,p)$ cross section for high energy (>9 mev) proton emission, centered near 24 mev. Since the protons observed had energies in excess of 9 mev they could not be the protons participating in the (γ,np) reaction. It is then tempting to consider this resonance as the $T_>$ component proceeding through the (γ,p) channel of Zn^{64}. Caution must be exercised in making such an identification, however, since all zinc isotopes are contributing to the observed resonance.

Strength of the $T_>$ component

The above identification of the 18 mev (γ,n) resonance and the 25 mev (γ,np) resonance with the $T_<$ and $T_>$ giant resonance components implies a

ratio of the integrated $T_>$ to $T_<$ cross sections as observed in these reactions to be no more than 20%. If one includes a possible 5-10% additional $T_>$ strength perhaps seen in the (γ,n) reaction in the neighborhood of 21-30 mev, an upper limit of about 30% is obtained for this ratio. Although this is considerably smaller than the upper limit of 53% estimated in Chapter II, it is possible that additional $T_>$ strength is proceeding through the (γ,p) and other channels. At any rate, the ratio of $T_>$ to $T_<$ strength inferred from this measurement is certainly consistent with the large effect predicted in Chapter II.

Other reaction mechanisms

There are two other mechanisms which might be postulated to result in a sizeable (γ,np) cross section; namely the statistical evaporation process and the quasideuteron effect. The first of these possibilities has been previously eliminated on the basis of the observed (γ,np) to $(\gamma,2n)$ ratio.

The quasideuteron model is more difficult to deal with but it is nevertheless an unlikely explanation of the strong (γ,np) resonance centered near 25 mev. First of all, this energy is rather low for the quasideuteron effect to be so large -- it is commonly thought to be relatively unimportant until excitation energies on the order of 40 mev (52). Secondly, and more significantly, the quasideuteron model predicts a smoothly varying (γ,np) cross section which is not at all consistent with the definite resonance peak observed to occur at about 25 mev. Furthermore, the (γ,np) cross section is observed to rise very rapidly and there is even evidence of unresolved fine structure in the vicinity of 25 mev; these features are difficult to reconcile with a quasideuteron model since it seems unlikely that the interaction of photons with correlated proton-

neutron pairs would depend so sharply on the energy of the incident photon. The quasideuteron effect is however known to be the dominant nuclear photoeffect for higher excitation energies and almost certainly accounts for the $Zn^{64}(\gamma,np)$ strength which has been observed above 40 mev (47,49) and is likely to be the process responsible for the (γ,np) strength above the solid line in Figure 18.

At present, there is not sufficient understanding of the single and multiple-nucleon decay modes in the region between 20 and 40 mev to completely rule out either the quasideuteron or other charge sensitive reactions, but the (γ,np) resonance observed in this measurement would seem to be anomolously large and sharp when associated with processes other than the $T_>$ giant resonance.

Summary of evidence

In summary, there is compelling evidence that the $T_>$ component is indeed observed in the $Zn^{64}(\gamma,np)$ cross section. The significant items are:

1) The (γ,np) cross section dominates the two-nucleon cross section for energies up to 40 mev.
2) The (γ,np) cross section indicates a definite segmentation into a strong resonance peak and a broad, seemingly continuous high energy component.
3) Both the relative strength and the mean energy of the (γ,np) peak are consistent with the isospin predictions for an independent particle model.
4) The (γ,np) resonance bears a striking resemblance to the (γ,n) cross section, consistent with the interpretation

that the T components of the giant resonance involve excitations to equivalent configurations.

5) A secondary (γ,n) channel for the $T_>$ resonance is predicted on the basis of known analog levels in Zn^{63} and there is some evidence of $T_>$ strength in this channel.

6) An earlier independent (γ,p) measurement in zinc also reports greatly enhanced strength in the 23-25 mev region.

7) Other possible (γ,np) mechanisms do not seem to reasonably account for the cross section characteristics observed for this reaction.

Taken together, these observations constitute strong evidence for the identification of the $T_>$ giant resonance component in this work. Although this evidence is not itself conclusive, it would appear to be one of the strongest experimental verifications of the validity of the isospin selection rules in the giant resonance phenomenon. Taken together with the results of other experiments, notably the Mo^{92} and Mo^{100} results of Gellie (11), one begins to develop confidence that the isospin selection rules are truly important in photonuclear reactions.

Related Work

Several interesting possibilities for verification of the isospin interpretation are suggested by the success of this experiment. The Zn^{64} nucleus presents a very "clean" (γ,np) channel for $T_>$ decay by virtue of the favorable energy distribution of the T = 5/2 levels in the neutron-residual nucleus, but this will not be the general situation. Most generally, this experiment suggests that the $T_>$ strength may be manifested

in several channels: (γ,p), (γ,n), (γ,np), $(\gamma,2n)$ and possibly others. Assuming isospin purity, the dominant channels can be predicted rather easily from known analog levels and reaction thresholds. Since the dominance of one or the other of these channels is very sensitive to the details of the $T_o + 1/2$ levels in the neutron-residual nucleus, the appearance or absence of strength in these channels provides a sensitive test of the validity of the isospin selection rules. In particular, it would be most interesting to study the (γ,n) and (γ,np) channels in nuclei for which most of the $T_o + 1/2$ levels of the neutron-residual nucleus are proton stable. Of particular interest is the other possibility of measuring the (γ,np) channel for nuclei in which the $T_o + 1/2$ levels of the neutron-residual nucleus are not energetically available for a significant part of the $T_>$ giant resonance but (γ,np) reactions are themselves energetically possible; the present interpretation would predict that the (γ,np) reaction would be nominal until the $T_o + 1/2$ levels become available.

As a means of experimentally separating the quasideuteron effect from the $T_>$ effect in the (γ,np) channel, it would be sufficient to measure the (γ,n) and (γ,np) cross sections for several isotopes of an appropriate element. The relative strength and energy of the $T_>$ component is quite sensitive to the neutron excess of the isotope whereas the quasideuteron cross section is expected to be proportional to NZ/A (53) and thus be quite constant for the isotopes of medium and heavy elements. Such a systematic study of the (γ,np) cross section trends would not have to be very detailed to be of utility and would shed light, not only on the isospin interpretation, but also on the quasideuteron model.

There is still a considerable amount of basic theoretical work

remaining to be done in the treatment of photonuclear isospin effects. Although the formalism of Leonardi and Rosa-Clot (12,52) supplies a useful vehicle for relating model dependent calculations to experimental observables, full exploitation of the relations is hindered by the lack of suitable calculations of the parameters. In particular, the treatment of the isotensor terms in equations II.18 and II.21 is not completely satisfactory. Also, the form of the isoscalar radius used in this work (equation II.19a) and apparently useful for $T \geq 2$ does not give reasonable values of the energy splitting for $T = 1/2$ nuclei.

There are also other sum rules which can be obtained from the formalism of Leonardi and Rosa-Clot; the formalism shows one how to write six sum rules (of which 4 are linearly independent), three of which relate the bremsstrahlung weighted cross sections to the quantities r_s^2, r_v^2, and r_t^2 and the other three relate the integrated cross sections to A_s, A_v, and A_t. Simply by requiring consistent predictions from these sum rules it should be possible to relate the parameters in greater detail, at the very least, these rules can be used to determine the consistency of a given set of calculated values.

The results of this experiment are then significant from several aspects: 1) The isotopic spin splitting of the giant resonance seems to be a reality for a medium weight nucleus, thus implying the rather complete isospin purity of the giant resonance excitation. 2) A new channel for isospin allowed decay of the $T_>$ component has been investigated in some detail; the apparent dominance of this channel suggests several interesting experiments and must be considered in the interpretation of previous experiments sensitive to multiple particle decay modes. 3) Recent

theoretical sum rules have been used to predict the features of the $T_>$ component; the reasonable success of this application provides impetus for further theoretical work.

In summary then, the success of the present investigation leads one to expect that the isospin selection rules will play an increasingly important role in the study of photonuclear reactions.

APPENDIX A. TREATMENT OF RADIOACTIVE DECAY IN THE ZINC 64 SYSTEM

In the present experiment, the yields are obtained from a least-squares fit to the measured decay curve. Since the decay curve involves several components, one of which is coupled to another via mother-daughter decay, it is necessary to carefully analyze the precise form of the equations governing the decay of the system, and which therefore define the experimental problem. The case of mother-daughter decay shall be treated generally in the first two sections and application to the Zn^{64} nucleus will be made in the third section.

Fundamental equations

The general differential equation for radioactive nuclei can be written as

$$\frac{dN_a(t)}{dt} = -\lambda_a N_a(t) + P_a(t) \qquad (A.1)$$

where $N_a(t)$ is the instantaneous number of nuclei in radioactive state "a" with decay constant $\lambda_a = \log_e(2.0)/T_a$, where T_a is the halflife of the state, and $P_a(t)$ is the instantaneous rate of production of nuclei in this state. The general solution of equation A.1 is written as

$$N_a(t_2) = N_a(t_1)e^{-\lambda_a(t_2-t_1)} + e^{-\lambda_a t_2}\int_{t_1}^{t_2} e^{\lambda_a t} P_a(t)\,dt \quad . \qquad (A.2)$$

Decay During Bombardment

During bombardment, assumed to occur from time $t_1 = 0$ to $t_2 = T$, photonuclear reactions occur which excite the radioactive state "a". The production rate due to photonuclear excitation is then $= I(t)Y_a$ where $I(t)$ is the instantaneous "dose current", $[I(t) = \frac{dD(t)}{dt}]$ and Y_a is the usual

photonuclear yield (a constant for given energy). D(t), the dosemonitor response to time t, is measured only at discrete times $t_i = i\Delta t$ (i = 0,1... n) where $\Delta t = T/n$. Thus the dose increments ΔD_i are known, where

$$\Delta D_i = D(t_i) - D(t_{i-1}) = \int_{t_{i-1}}^{t_i} I(t)dt \quad . \tag{A.3}$$

Mother state production

Since there is no other source of mother state nuclei, the total production is due to photonuclear excitation and

$$P_m(t) = I(t)Y_m \qquad (0 \leq t \leq T) \tag{A.4}$$

where the subscript "m" is used to designate the mother state. Assuming that there are initially no mother state nuclei ($N_m(t_1) = 0$, $t_1 = 0$), equation A.2 then gives for the number of radioactive nuclei at end of bombardment

$$N_m(T) = Y_m e^{-\lambda_m T} \int_0^T e^{\lambda_m t} I(t)dt \tag{A.5a}$$

$$= Y_m \sum_{i=1}^{n} e^{-\lambda_m[T-(i-1)\Delta t]} \int_{t_{i-1}}^{t_i} e^{\lambda_m(t-t_{i-1})} I(t)dt \quad , \tag{A.5b}$$

where the integral has been subdivided into the same intervals for which the dose is measured. Since I(t) is an unknown and rapidly varying (>>60hz) function, exact solution of this equation is not possible. However, $e^{\lambda_m(t-t_{i-1})}$ is a slowly varying function over the interval t_{i-1} to t_i so long as $T_m >> \Delta t$; assuming that Δt is sufficiently small then, it is

reasonable to approximate $e^{\lambda_m(t-t_{i-1})} \cong e^{\lambda_m(\Delta t/2)}$, the midpoint value. Making this replacement and employing A.3 one then obtains the approximation

$$N_m(T) \cong Y_m \sum_{i=1}^{n} \Delta D_i e^{-\lambda_m[T-(i-1/2)\Delta t]} \qquad (\Delta t = T/n) \quad . \tag{A.6}$$

Daughter state production

Daughter state nuclei are produced not only by photonuclear excitation, but also by decay from the mother state, thus

$$P_d(t) = \lambda_m N_m(t) + I(t)Y_d \qquad (0 \leq t \leq T) \tag{A.7}$$

where the first term represents the mother state decay rate, and the second is the rate of direct photonuclear production. Again assuming that no daughter nuclei are initially present, one obtains for the total number of radioactive daughter nuclei at the end of bombardment

$$N_d(T) = e^{-\lambda_d T} \int_0^T e^{\lambda_d t}[\lambda_m N_m(t) + Y_d I(t)]dt \tag{A.8a}$$

$$= \sum_{i=1}^{n} e^{-\lambda_d[T-(i-1)\Delta t]} \int_{t_{i-1}}^{t_i} e^{\lambda_d(t-t_{i-1})}[\lambda_m N_m(t) + Y_d I(t)]dt \ , \tag{A.8b}$$

where the integral has again been subdivided. Here $N_m(t)$ is the instantaneous number of mother state nuclei at time $0 \leq t \leq T$ and is given exactly by

$$N_m(t) = Y_m e^{-\lambda_m t} \int_0^t e^{\lambda_m x} I(x)dx \tag{A.9}$$

obtained in the same manner as equation A.5a.

One might think of approximating equation A.9 in the same manner as was used to obtain A.6, however, since the dose is only measured at the discrete times t_i, it is only possible to define discrete values $N_m(t_i)$ without making additional assumptions about $I(t)$;

$$N_m(t_i) \cong Y_m \sum_{j=1}^{i} \Delta D_j e^{-\lambda_m[t_i-(j-1/2)\Delta t]} \quad . \tag{A.10}$$

The integral of equation A.8b requires that $N_m(t)$ be a continuously defined function; approximation of the integral so that the discrete values $N_m(t_i)$ can be used may compound the errors of approximation already involved in equation A.10.

These difficulties are largely circumvented by use of the identity $\lambda_m N_m(t) = Y_m I(t) - dN_m(t)/dt$ (cf. equations A.1 and A.4), so that equation A.8b can be written

$$N_d(T) = \sum_{i=1}^{n} e^{-\lambda_d[T-(i-1)\Delta t]} \int_{t_{i-1}}^{t_1} e^{\lambda_d(t-t_{i-1})} [Y_d I(t) + Y_m I(t) - dN_m(t)/dt]dt \tag{A.11a}$$

and making the same assumptions as before, one then obtains

$$N_d(T) \cong \sum_{i=1}^{n} e^{-\lambda_d[T-(i-1/2)\Delta t]} [\Delta D_i(Y_d+Y_m) - N_m(t_i) + N_m(t_{i-1})] \quad . \tag{A.11b}$$

It is useful at this point to discuss the physical significance of the approximation. It will be noted that each of the terms in the summations of equations A.6 and A.11b involve the product of an exponential factor and a constant. The constant factor, in each case, can easily be seen to be

exactly equal to the total production of the desired state for the i^{th} interval. The exponential factor is the probability that an excited nucleus, produced at the center of the interval, will not have decayed by bombardment time T. Thus each term in the expansion represents the number of nuclei, produced during the interval, which will still be present at end of bombardment in the approximation that production occurs only at mid-interval. It is obvious that such an approximation is very good if all halflives are much greater than Δt; indeed, in the limit $\Delta t \to 0$, both results are exact. Of course, since approximation A.10 will ultimately be employed to evaluate equation A.11b, the production factor in the latter equation cannot be evaluated exactly. For the zinc case T_m = 9.12 hours (Zn^{62}) and for $\Delta t \leq 10$ secs., as used in this experiment, the approximation error is negligible.

Corrected dose

It is useful to define the quantity $D_c^a(T)$, the "corrected dose", such that

$$Y_a = \bar{N}_a(T)/D_c^a(T) \tag{A.12}$$

where $\bar{N}_a(T)$ is the number of nuclei, produced solely by photonuclear excitation, which remain at the end of bombardment. That is

$$D_c^a(T) = e^{-\lambda_a T} \int_0^T e^{\lambda_a t} I(t)dt \tag{A.13a}$$

and is well approximated by

$$D_c^a(T) \cong \sum_{i=1}^{n} \Delta D_i e^{-\lambda_a[T-(i-1/2)\Delta t]} , \qquad (\Delta t = T/n) \quad . \tag{A.13b}$$

In the case of the mother nucleus, this definition is an obvious one since

$$N_m(T) = \bar{N}_m(T) = Y_m D_c^m(T) \quad . \tag{A.14a}$$

In the case of the daughter nucleus there is a contribution not due to photonuclear excitation and from equation A.11b

$$N_d(T) \cong \bar{N}_d(T) + \sum_{i=1}^{n} e^{-\lambda_d[T-(i-1/2)\Delta t]} [\Delta D_i Y_m - N_m(t_i) + N_m(t_{i-1})] \tag{A.14b}$$

$$= Y_d D_c^d(T) + Y_m D_c^{m-d}(T) \tag{A.14c}$$

where

$$D_c^{m-d}(T) = \sum_{i=1}^{n} e^{-\lambda_d[T-(i-1/2)\Delta t]} \{\Delta D_i - [N_m(t_i) - N_m(t_{i-1})]/Y_m\} \quad . \tag{A.14d}$$

The new quantity $D_c^{m-d}(T)$ is here referred to as the "corrected mother-daughter dose" since it has the dimensions of a dose and $Y_m D_c^{m-d}(T)$ is the number of nuclei, produced by mother-daughter decay, which remain in the daughter state at end of bombardment. By employing equation A.10 to evaluate $N_m(t_i) - N_m(t_{i-1})$ one finally obtains after some manipulation

$$D_c^{m-d}(T) = (1-1/\theta) D_c^d(T) + \sum_{i=1}^{n} (\theta - 1/\theta) e^{[\lambda_m - \lambda_d][T-(i-1/2)\Delta t]} \sum_{j=1}^{i-1} \Delta D_j e^{-\lambda_m[T-(j-1/2)\Delta t]} \tag{A.15}$$

where

$$\theta = e^{\lambda_m \Delta t/2} \quad .$$

In the actual computation of the corrected doses, it is convenient to perform the summations term-by-term, simultaneously accumulating all of the corrected doses. The above form for $D_c^{m-d}(T)$ is then particularly convenient since for given i, the summation over j which appears in equation A.15 is just the "previous" value of $D_c^m(T)$ (cf. equation A.13b).

Decay Following Bombardment

The dose current is zero following bombardment, so there is no further photonuclear production. Thus the production rates are $P_m(t) = 0$, $P_d(t) = \lambda_m N_m(t)$, $(t > T)$. Applying equation A.2 one then obtains

$$N_m(t) = N_m(T)e^{-\lambda_m(t-T)} \qquad (t > T) \tag{A.16}$$

and

$$N_d(t) = N_d(T)e^{-\lambda_d(t-T)} + e^{-\lambda_d t}\int_T^t e^{\lambda_d x}\lambda_m N_m(x)dx \tag{A.17a}$$

$$= N_d(T)e^{-\lambda_d(t-T)} + \frac{\lambda_m N_m(T)}{\lambda_d-\lambda_m}\left[e^{-\lambda_m(t-T)} - e^{-\lambda_d(t-T)}\right], \quad (t > T). \tag{A.17b}$$

The measured counts

In a time interval t_j to $t_j + w_j$, the total number of nuclei of type "a" which will decay is given by the integral from $t = t_j$ to $t = t_j + w_j$ of the decay rate $N_a(t)\lambda_a$. Not all of the decays may be detected however, even for a 100% efficient detector, since the excited nucleus may have several modes of decay, not all of which may involve emissions to which the detector is sensitive. In the present case, the detector is designed to be sensitive to positron emission only and only those decays which involve positron emission can be counted. Let ϵ_a be the probability that the

excited state "a" will decay via positron emission; the number of counts detected in the interval t_j to $t_j + w_j$ is then given by

$$C_{aj} = \epsilon_a \int_{t_j}^{t_j+w_j} \lambda_a N_a(t)\,dt = \text{counts in } j^{th} \text{ interval from } a^{th} \text{ activity.} \quad (A.18)$$

(In the present case, the absolute calibration of the detector is not important, so the detector efficiency has been taken to be 100%.) Using the compact notation

$$f_{aj} = (1 - e^{-\lambda_a w_j}) e^{-\lambda_a (t_j - T)} \qquad (t_j > T) \quad (A.19)$$

one then finds

$$C_{mj} = \epsilon_m N_m(T) f_{mj} = \text{counts due to mother state decay} \quad (A.20a)$$

and

$$C_{dj} = \epsilon_d \left[N_d(T) f_{dj} + \frac{N_m(T)}{\lambda_d - \lambda_m} (\lambda_d f_{mj} - \lambda_m f_{dj}) \right] = \text{counts due to daughter decay.} \quad (A.20b)$$

The total counts, C_j, due to decays from both states is then written

$$C_j = A_d f_{dj} + A_m f_{mj} = \text{total counts in } j^{th} \text{ interval} \quad (A.21a)$$

where

$$A_d = \epsilon_d \left[N_d(T) - \frac{\lambda_m N_m(T)}{\lambda_d - \lambda_m} \right] , \quad (A.21b)$$

$$A_m = \left[\epsilon_m + \frac{\epsilon_d \lambda_d}{\lambda_d - \lambda_m} \right] N_m(T) \quad . \quad (A.21c)$$

It is thus seen that the decay of the mother-daughter system can be treated as a simple two-component decay with coupled coefficients.

Least-squares fit

In the most general activation experiment, there may be several activities excited, some of which may be coupled by a mother-daughter relationship, as well as a constant background activity. For the general case of n observable activities plus a background, the observed number of counts in the j^{th} interval is given by

$$C_j = \sum_{a=0}^{n} A_a f_{aj} = \text{total counts in interval } t_j \text{ to } t_j + w_j \qquad (A.22)$$

where $f_{aj}(a > 1)$ is defined by equation A.19, $f_{0j} = w_j$, and A_0 is the background counting rate. Note that for an activity which decays to a stable daughter state ($\lambda_d = 0$), equation A.21c gives $A_m = \epsilon_m N_m(T)$. The functions f_{aj} are collectively known as the "fitting functions" and the A_a are the "coefficients of the fit" which are to be determined from the least-squares analysis.

The method of least-squares fitting is a well known technique and is only summarized here for reference.

If a set of experimental values $\bar{C}_j$ (the measured counts) are known for the above counting intervals, one then defines the statistical variable χ^2 in terms of the residuals $\bar{C}_j - C_j$ and the uncertainty σ_j of the measured $\bar{C}_j$. Thus

$$\chi^2 = \sum_j (\bar{C}_j - C_j)^2/\sigma_j^2 = \sum_j (\bar{C}_j - \sum_{a=0}^{n} A_a f_{aj})^2/\sigma_j^2 \quad . \qquad (A.23)$$

Minimizing χ^2 with respect to the b^{th} coefficient one obtains

$$\frac{\partial \chi^2}{\partial A_b} = 0 = \sum_j (\bar{C}_j - \sum_{a=0}^{n} A_a f_{aj}) f_{bj}/\sigma_j^2 \qquad (A.24a)$$

which when reorganized yields the matrix equation

$$G_b = \sum_{a=0}^{n} A_a Z_{ab} \qquad \text{(A.24b)}$$

where

$$G_b = \sum_j \bar{C}_j f_{bj}/\sigma_j^2 \qquad \text{(A.24c)}$$

and

$$Z_{ab} = \sum_j f_{aj} f_{bj}/\sigma_j^2 \qquad \text{(A.24d)}$$

Equation A.24b can be inverted to give the minimum χ^2 solution:

$$A_a = \sum_{b=0}^{n} Z_{ab}^{-1} G_b \qquad \text{(A.25a)}$$

and it can be shown that the uncertainty in the fitted coefficients A_a is given by

$$\Delta A_a = (Z_{aa}^{-1})^{1/2} \quad . \qquad \text{(A.25b)}$$

It is common to refer to the Z matrix, defined as above, as the "curvature matrix" and Z^{-1}, the matrix inverse of Z, as the "error matrix".

Calculation of the yields

Since the fitting coefficients A_a can be obtained from a least-squares fit to the measured decay curve, it is then possible to solve for $N_a(T)$, the number of radioactive nuclei remaining at end of bombardment. From equations A.21b and A.21c one then obtains

$$N_m(T) = A_m/\gamma \qquad \text{(A.26a)}$$

and

$$N_d(T) = A_d/\epsilon_d + \frac{\lambda_m}{\lambda_d - \lambda_m} (A_m/\gamma) \qquad \text{(A.26b)}$$

where

$$\gamma = \epsilon_m + \frac{\lambda_d \epsilon_d}{\lambda_d - \lambda_m} \quad . \tag{A.26c}$$

Note that the daughter state decay increases the effective fraction of positron decay for the mother state (γ) above its physical branching ratio ϵ_m. This is a direct consequence of the fact that every mother state decay is followed by a daughter state decay, thus the mother state decay may be counted more than once. If $\lambda_m \ll \lambda_d$, as it is for the mother-daughter system of Zn^{62} - Cu^{62}, then $\gamma \cong \epsilon_m + \epsilon_d$.

Finally, by equating equations A.26a and A.26b with equations A.14a and A.14c respectively, one obtains expressions for the yields in terms of the fitted coefficients and the corrected doses.

$$Y_d = \frac{1}{D_c^d(T)} \left[\frac{A_d}{\epsilon_d} + \left(\frac{\lambda_m}{\lambda_d - \lambda_m} - \frac{D_c^{m-d}(T)}{D_c^m(T)} \right) \frac{A_m}{\gamma} \right] \tag{A.27a}$$

$$Y_m = \frac{1}{D_c^m(T)} \frac{A_m}{\gamma} \quad . \tag{A.27b}$$

For convenience, the important results and definitions of this section are summarized in compact notation in equations A-29. It should be noted that the fitted coefficients A_a as used above, are referenced to the end of bombardment time, t=T (cf. equation A.19). If the counting intervals are referenced to a different time, say time t = T + S, then in order to obtain proper scaling the coefficients A_d and A_m must be multiplied by the factors $e^{\lambda_d S}$ and $e^{\lambda_m S}$ respectively.

Application to Zinc 64 System

For the present experiment, the experimental constants are listed below for the reactions $Zn^{64}(\gamma,n)Zn^{63}$, $Zn^{64}(\gamma,np)Cu^{62}$ and $Zn^{64}(\gamma,2n)Zn^{62}$ respectively where the latter two reactions are coupled by mother-daughter decay. In the case of the (γ,n) reaction, Zn^{63} decays to stable Cu^{63} and there is thus no coupling involved.

1) Cu^{63}: $T_1 = 2306.5$ sec., $\epsilon_1 = .93$
2) Cu^{62}: $T_2 = 582.6$ sec., $\epsilon_2 = .972$
3) Zn^{62}: $T_3 = 32940$ sec., $\epsilon_3 = .152$.

The yields are then given by:

$$Y(\gamma,n) = \frac{1}{D_c^1(T)} \frac{A_1}{\epsilon_1}$$

$$Y(\gamma,np) = \frac{1}{D_c^2(T)} \left[\frac{A_2}{\epsilon_2} + \frac{A_3}{\gamma} (\beta - R_{32}) \right]$$

$$Y(\gamma,2n) = \frac{1}{D_c^3(T)} \frac{A_3}{\gamma}$$

where $\gamma = \epsilon_3 + \lambda_2\epsilon_2/(\lambda_2-\lambda_3) = 1.142$ and $\beta = \lambda_3/(\lambda_2-\lambda_3) = .018$. For constant dose current $I(t) = D/T$, where D is the total dosemonitor response for a bombardment of length T, the corrected doses can be evaluated exactly to obtain:

$$\overline{D}_c^a(T) = \frac{D}{T\lambda_a} (1 - e^{-\lambda_a T}) \qquad \text{(A.28a)}$$

$$\overline{D}_c^{m-d}(T) = \frac{D}{T} \left\{ \frac{1}{\lambda_d} (1 - e^{-\lambda_d T}) - \frac{1}{(\lambda_D-\lambda_m)} (e^{-\lambda_m T} - e^{-\lambda_d T}) \right\} \qquad \text{(A.28b)}$$

and thus the ratio $R_{32} = \bar{D}_c^{3-2}(T)/\bar{D}_2^3(T)$ can then be evaluated to obtain $R_{32}(58\ \text{min}) = 0.014$ and $R_{32}(8\ \text{min}) = .0042$ for the LONG and SHORT run configurations respectively. Then the mother-daughter coupling term = $(1/\gamma)(\beta - R_{32})$ is found to be 0.4% and 1.2% for the two configurations used. For either run configuration, it is found that the fitting coefficients A_2 and A_3 (9.7 min.and 12 hr. coefficients) are of the same order of magnitude, so the mother-daughter correction to the (γ,np) yield is a minor contribution to the strength observed. In particular, the mother-daughter correction to the (γ,np) yield typically amounts to an increase of .4% for the LONG configuration and .5% for the SHORT configuration. Since this contribution is about the same magnitude as the uncertainty due to statistical considerations, the mother-daughter correction is not a significant factor in the computed (γ,np) yield.

Summary of Radioactive Yield Equations

For convenient reference, the results and definitions of this appendix are summarized below. A somewhat more general notation has been used to clarify the relations of the various quantities: "m" refers to mother state nucleus, "d" to corresponding daughter state nucleus, "s" to nucleus decaying to stable daughter state ($\lambda_d = 0$), "a" is an arbitrary nuclear state.

Yields

$$Y_m = \frac{1}{D_c^m(T)} \frac{A_m}{\gamma} = \text{yield for excitation to mother state} \qquad \text{(A.29a)}$$

$$Y_d = \frac{1}{D_c^d(T)}\left[\frac{A_d}{\epsilon_d} + \frac{A_m}{\gamma}(\beta - R_{md})\right] = \text{yield for excitation to daughter state} \qquad \text{(A.29b)}$$

$$Y_s = \frac{1}{D_c^s(T)} \frac{A_s}{\epsilon_s} = \text{yield for excitation to state "s" (no daughter state decay)} \quad \text{(A.29c)}$$

Definitions of dose quantities

$$D_c^a(T) \cong \sum_{i=1}^{n} \Delta D_i e^{-\lambda_a [T-(i-1/2)\Delta t]} = \text{corrected dose for excitation to state "a"} \quad \text{(A.29d)}$$

$$D_c^{m-d}(T) \cong D_c^d(T)(1-1/\theta) + \sum_{i=1}^{n} e^{(\lambda_m-\lambda_d)[T(i-1/2)\Delta t]} (\theta-1/\theta) \sum_{j=1}^{i-1} \Delta D_j e^{-\lambda_m [T-(j-1/2)\Delta t]} =$$

corrected mother-daughter dose (A.29e)

$$R_{md} = \frac{D_c^{m-d}(T)}{D_c^m(T)} = \text{fractional mother-daughter dose} \quad \text{(A.29f)}$$

Derived constants

$$\theta = e^{\lambda_m \Delta t/2}, \quad \beta = \frac{\lambda_m}{\lambda_d - \lambda_m}, \quad \gamma = \lambda_m + \frac{\epsilon_d \lambda_d}{\lambda_d - \lambda_m}$$

Physical constants

ϵ_a = fraction of decays from excited state "a" which proceed by positron emission

λ_a = decay constant for radioactive nucleus (= $\log_e(2.0)$/halflife)

Fitted coefficients

A_a = coefficient of radioactive component with decay constant λ_a, referenced to time T.

Measured quantities

$\bar{C}_j$ = total counts accumulated in time interval t_j to $t_j + w_j$ ($t_j > T$)

ΔD_i = net dosemonitor response during time interval t_{i-1} to t_i

($t_i = i\Delta t$, $i = 1,2,\ldots,n$)

Experimental parameters

T = total length of bombardment (time of end of bombardment).

Δt = width of time interval at which dosemonitor response is read

($\Delta t = T/n$).

APPENDIX B. ACCIDENTAL AND DEADTIME CORRECTIONS

The block diagram of a coincidence counting system is given in Figure 19. The total rate of radioactive decay in the sample is $N_T = N_p + N_G$ where N_p is the rate of positron decays and N_G is the rate of gamma-emitting (only) decays. A fraction ρ of the total decays are observed in the radiation detectors resulting in N observed events. Because of dead-time τ in each of the detector electronics only m pulses are generated. The pulses from each detector are coincidence analyzed in the coincidence unit with coincidence resolving time T_c. The measured number of coincidence events for the system is m_c. The efficiency ρ of the radiation detectors is assumed to be a constant and will be of no interest in this discussion. The problem will be to relate the observed coincidence counting rate m_c to N_p, the rate of positron emission. It is useful to define the quantity N_c, the "true" coincidence rate, as the coincidence rate which would be observed if $T_1 = T_2 = T_c = 0$. That is, $m_c = N_c$ if no counting rate distortions are introduced by the electronics. N_c is thus proportional to the positron rate N_p with a constant of proportionality determined entirely by the detection efficiencies ρ. It will be shown that the "true" and observed counting rates are approximately related by

$$m_c = N_c (1 + \alpha N_c) \qquad \text{(B-1)}$$

where α is referred to as the "slope correction constant".

A possible sequence of counting events is shown in Figure 20 and illustrates the important features of the problem. Five positron emission events P1 - P5 are indicated but due to the inefficiency of the detectors, not all are detected by either detector. However, gamma emissions, not

Figure 19. Block diagram of coincidence circuit with deadtimes T_1 and T_2 and resolving time T_c.

Figure 20. Illustration of deadtime losses and accidental coincidence effects in a coincidence counting system. C_1 is a true coincidence event and C_2 is an accidental coincidence. Positron events P_2,P_3,P_4, and P_5 do not result in measured coincidences because of efficiency and deadtime losses. Single gamma rays (γ) are also observed in each detector.

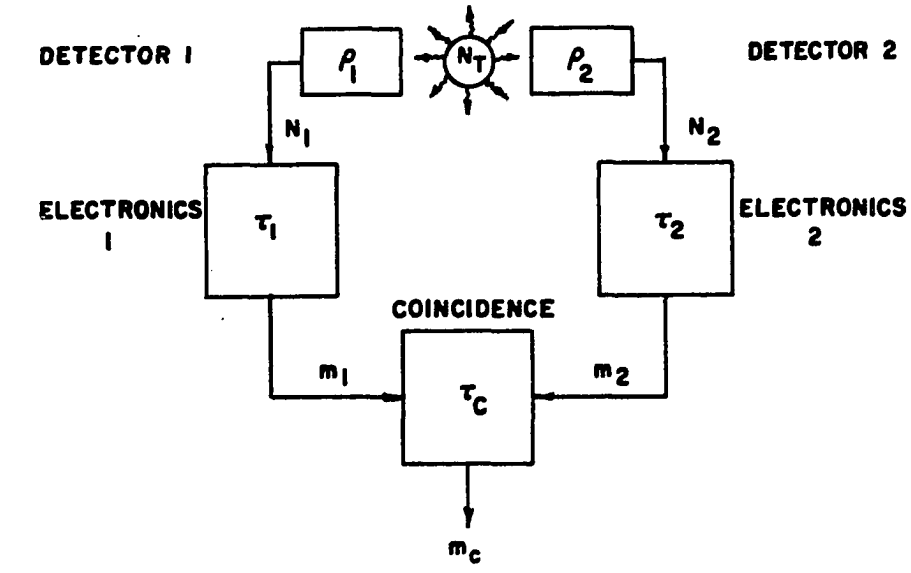
DETECTOR 1
ρ_1
N_T
ρ_2
DETECTOR 2
N_1
N_2
ELECTRONICS 1
τ_1
τ_2
ELECTRONICS 2
COINCIDENCE
m_1
τ_C
m_2
m_c

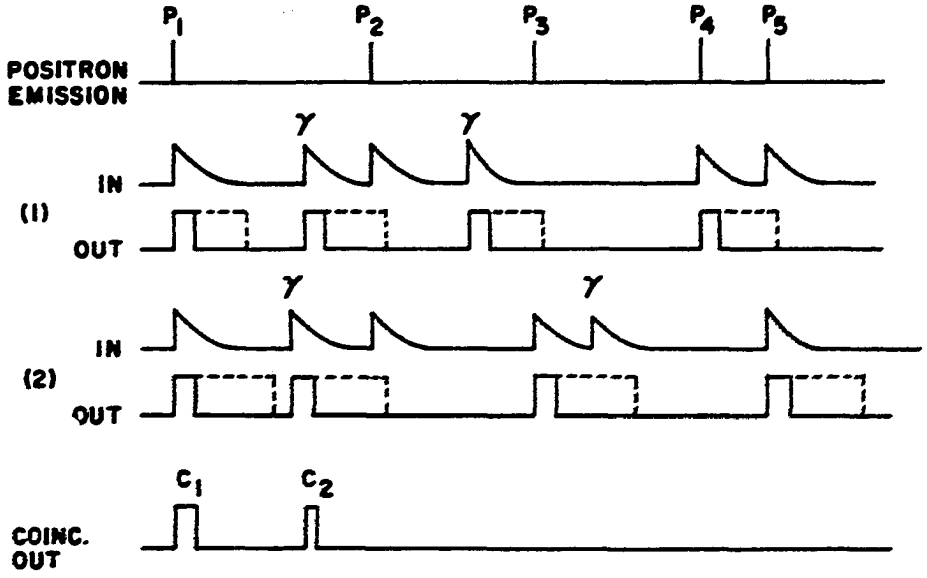
P_1
P_2
P_3
P_4
P_5
POSITRON EMISSION
γ
γ
IN
(1)
OUT
γ
γ
IN
(2)
OUT
C_1
C_2
COINC. OUT

correlated with positron emission, are also detected and lead to detector pulses. The pulses entering the separate electronics are the series labelled "in" and consist of some pulses due to positron emission as well as pulses due to uncorrelated gamma rays (labelled "γ"). Output pulses, indicated by solid lines, are generated by the electronics but some pulses are lost because they fall within the deadtime (indicated by dashed line) of the electronics. Pulses from the two detectors which overlap in time result in coincidence output pulses. It is seen in the figure that the C_1 coincidence pulse results from detection of a positron emission, but the second pulse, C_2, results from the "accidental coincidence" of two uncorrelated gamma rays. For the purpose of this discussion an accidental coincidence will be taken to be any coincidence resulting from uncorrelated events (thus gamma-positron coincidences are also accidental coincidences). Only the positron events P_1, P_2, and P_5 contribute to N_c (the "true") coincidence rate) since only these events produce pulses in both detectors.

Deadtime effects

For each detector, every output pulse is accompanied by a deadtime period of length T during which the circuit is insensitive to other input events. Thus, the fractional deadtime for the circuit is mT and of the N input pulses, NmT are lost per unit time so that the observed "singles" rate m is given by

$$m = N - N mT \quad . \tag{B.2}$$

Although N input pulses are detected, we are here concerned only with the N_c counts which are due to positron emission (note that $N \geq N_c$ for

each detector, by the previous definition). Considering only the effect on the true coincidence pulses, the rate of deadtime losses is then $N_c mT$ for either detector. It is easily seen that if a count is lost within either detector, it can not result in a coincidence output pulse. Thus, although positron event P_5 in Figure 20 is detected by both circuits, it is lost through deadtime in circuit 1, and thus does not lead to an observed coincidence. If one circuit, say circuit 1, has $T_1 = 0$ then the system deadtime loss is $N_d = N_c m_2 T_2$, due only to circuit 2. If however, both circuits have deadtimes, and the deadtime periods for the two circuits never occur simultaneously, then $N_d = N_c(m_1 T_1 + m_2 T_2)$, the sum of the losses. This latter form, however, neglects the fact that some pulses are deadtime-lost in both circuits (eg. pulse P_2 in Figure 20) and these losses are counted twice in the above relation. If the positron emission rate is a major fraction of the total "singles" rate then the deadtime periods of the two detectors will be highly correlated and a significant fraction of the losses will occur in both circuits.

It is convenient to assume that one of the detectors (the "worse" detector) dominates the system deadtime and the other ("better") detector's deadtime is included as a correction. The form used is then

$$N_d = N_c(m_w \tau_w + \bar{P}_w m_b \tau_b) = \text{rate of deadtime losses for system} \quad (B.3)$$

where the subscripts "w" and "b" refer to the worse and better detector respectively. $\bar{P}_w$ is the probability that an event is not deadtime-lost in the worse detector. All events deadtime-lost in the worse circuit are given by the first term and those events lost only in the better circuit are included in the second.

Accidental coincidence effect

Each pulse into the coincidence unit has a width t_c and two pulses can overlap over a total time interval $T_c = 2t_c$, the coincidence resolving time. Then the probability of random overlap of two uncorrelated pulses is proportional to T_c and the rate of accidental coincidences is approximately

$$N_a = m_1 m_2 T_c \tag{B.4}$$

where correlation of pulses from the two sources if neglected. Because of deadtime losses (a relatively small effect), efficiency losses, and the detection of extraneous gamma rays, the assumption of non-correlation is an acceptable approximation.

Observed counting rate

The observed counting rate is then given by

$$M_c = N_c - N_d + N_a \tag{B.5}$$

where N_d is the deadtime loss given by equation B.3 and N_a is the accidental coincidence rate given by equation B.4. Since the singles counting rates m_1 and m_2 are not known, it is now necessary to eliminate them from the equations. It is reasonable to assume that the singles rates are proportional to the true coincidence rate and it is assumed that constants e_1 and e_2 can be determined such that

$$N_c = m_1/e_1 = m_2/e_2 \quad . \tag{B.6}$$

This approximation is valid so long as most of the singles rate is due to the same reactions as are producing the positrons (i.e. background contributions are not excessive) and the deadtime corrections to m_1 and m_2

are not too large. Equations B.3, B.4, B.5, and B.6 can now be combined to obtain equation B.1 with

$$\alpha = e_w e_b T_c - e_w T_w - (1 - 1/e_w)\, e_b T_b \quad . \tag{B.7}$$

Here $\bar{T}_w$ has been taken to be $(1-1/e_w)$ since $1/e_w$ is the probability that a given singles count in the worse detector is a true coincidence count.

The above expression for α is of limited usefulness since it is usually difficult to measure the necessary quantities to sufficient accuracy, however, it is convenient as a means of estimating the count rate distortion. The constants e_i can be estimated by observing that $m_c \to N_c$ as $m_c \to 0$; a plot is made of m_c/m_i (both quantities suitably corrected for background) and the intercept at $m_c = 0$ is then taken to be e_i. For this experiment, the e_i values measured in this manner are typically 2.5 and using $\bar{T} = 1\mu s$ and $T_c = 400$ ns a value $\alpha \cong -1 \times 10^{-6}$ is obtained.

The major importance of this discussion is that it leads to a convenient functional form for correcting the observed counting rates for the accidental coincidence and deadtime effects. Equation B.1 can be inverted to obtain the useful form

$$N_c = m_c(1 - \alpha m_c + 2(\alpha m_c)^2 - 5(\alpha m_c)^3 + \ldots) \quad . \tag{B.8}$$

The higher order terms approach zero rapidly for small αm_c and can usually be neglected. In the present case $\alpha m_c = -10^{-2}$ for an extreme rate $m_c = 10{,}000$ counts/sec. and the higher order terms contribute little.

APPENDIX C. COMPUTER PROGRAMS

A number of computer programs have been employed in the accumulation and reduction of the data for this experiment. Four of the computer programs (MULTIFACTORY, PMF, APU, CLSR) are major routines and warrant at least a general description. The CLSR routine is adequately described in a previous publication (25) and the discussion of the other routines shall be confined to factors of significance to the experimental method and/or design features which might be applicable to related work.

The MULTIFACTORY Routine

Yield curves for many photonuclear reactions are conveniently measured by the activation method. In the simplest case (one radioactive product and known or negligible background) it is sufficient to measure only the total number of decays in a definite time interval and the corrected dose; for very constant beam intensity or halflife much longer than the bombardment period the corrected dose is just the total accumulated dose or analog networks can also be devised whose output corresponds to the corrected dose when these conditions do not hold. The more general situation involves one or more competing activities and it is necessary to separate the halflife components from the total decay curve. In such a case, it is necessary to perform a more complicated experiment: 1) The decay curve must be measured using a large number of suitably chosen intervals. 2) The activities must be separated from the decay curve using a statistical separation method (such as the method of least-squares fitting). 3) The corrected doses must be measured separately for each activity; this is most conveniently done by measuring the beam intensity

as a function of time and calculating the corrected doses from this data.

A general on-line computer program has been developed at this laboratory for use with the SDS computer installation; this routine, designated FACTORY, is capable of measuring decay curves from three counting houses simultaneously, monitoring and recording the beam intensity, and computing the corrected doses for up to three activities. A compact routine for performing the least squares fit on-line has been developed by this author and is incorporated in the FACTORY routine.

For the purposes of the present experiment, the FACTORY routine was inadequate and hence the MULTIFACTORY program was developed. The specific criteria involved in the design of the MULTIFACTORY routine were: 1) provision for a mother-daughter decay scheme; 2) increased "through-put" using available experimental equipment; 3) increased supervisory and control functions to minimize manual operations and reduce human error; 4) full on-line analysis of the data; 5) greater flexibility in the choice of counting schedules.

Features of the MULTIFACTORY routine

Some of the interesting features of the MULTIFACTORY routine are stated below.

Interleaved counting from several sources By defining an appropriate counting schedule, it is possible to interleave the counting schedules of up to four separate decay curves in a single counting house. Three counting houses are utilized simultaneously, allowing up to 12 runs to be active at a given time.

Variable counting interval specification Each period of counting activity is broken into one or more "blocks" of basic counting intervals

and the width and the number of intervals in a block are variable. Five general purpose and two special purpose blocks are provided.

Accurate experimental timing Through the use of multiple priority interrupts, synchronous operations, and self compensating "clocks" it has been possible to maintain a short term timing resolution of about 1 ms or better and accuracy of better than 1 second over a month of continuous operation.

Buffered output routines An inclusive package of buffered output routines has been incorporated in MULTIFACTORY. The output devices are supplied at maximum rate under a time-sharing scheme, thereby freeing the user from output timing considerations and resulting in increased output rates. Both pre-formatted and stream modes are incorporated and output destined for the paper tape punch is automatically blocked in labeled card-records.

Dynamic CRT graphic display The attendant is specifically informed of his tasks and the current experimental status by messages generated on a long-persistence display oscilloscope. Warning messages are displayed when error conditions are detected and correct responses are verified.

Extensive control capability Only such functions as require human dexterity or involve safety considerations are required of the human attendant. Specifically, all operations apart from changing and transporting the samples, turning on and maintaining the synchrotron beam, and setting up the source for dose monitor checks are performed by the computer. The tasks of the attendant are clustered at definite, well-separated intervals and a warning buzzer system is used to inform of impending duties, thereby freeing the attendant for other tasks between calls.

Error control The attendant is required to verify his activities before affected data is accumulated. Critical operations are protected by "locking out" spurious responses.

On-line data reduction An essentially complete analysis of the general photonuclear activation experiment is incorporated in MULTIFACTORY. Specifically, a linear least-squares fit is performed (up to 4 halflives plus background) and the corrected doses are computed (4 activities with one mother-daughter pair). Basic data corrections are applied ("slope" correction of the counting data, and application of house and sample normalization factors), and the radioactive yields are computed, together with their statistical uncertainties.

Standard output formats All significant data related to the experiment is output, both on the teletype as a running experimental log, and on paper tape for later conversion to punched cards. The numerical values are output in standard integer and floating point formats (I format and E12.6 format) and are compatible with Fortran and PL/1 input requirements.

Flexibility The control and data parameters may be set up and modified from the teletype console. A complete listing of the variable parameters is produced for documentation and the parameters may be dumped on paper tape for later read-in. Later modification of the routine has been facilitated by use of standardized subroutines, functional code-blocks, the use of "list-oriented" data access and control operations, and the consolidation of data, parameter and constant storage, control flags, and joint work areas into two major "common" storage arrays.

The SDS 910 computer and interface

The SDS 910 computer is a relatively small (8192 word memory) general purpose digital computer which has been interfaced to a large number of experimental and control devices at this installation. All internal word lengths (data and instruction) are 24 bits plus parity bit and three 24 bit programmable registers are provided (two arithmetic registers and one index register). The hardware-supported instructions represent a basic set of memory access, logical, register change and register shift, arithmetic, branch, test-and-skip, and internal and external control instructions. Although only single-word integer addition and subtraction are fully hardware supported (twos complement), full fixed-point (single word) and floating-point (double word) arithmetic operations are software supported in the form of programmed operators (POPs). Indexing and indirect addressing are supported for most instructions. The basic machine cycle is 8 μs and typical machine instructions require 1-3 cycles. A Fortran compiler is provided but the basic language employed for on-line programs is SYMBOL, an assembler source language provided by the manufacturer.

Basic peripheral devices include a fast paper tape punch and high speed photo-reader, a Teletype model 35 ASR console with auxiliary paper tape reader-punch, a card reader, and a MAGPAK incremental magnetic tape-cartridge unit. All of the above devices are interfaced through a 24 bit I/O buffer and two priority I/O interrupts (I31 and I33) are available. A programmable "interlace" register may be used to program the I/O buffer for time-sharing input/output operations.

A set of 16 priority interrupts are presently available for experimental usage and the source may be selected by wiring a removable patch

panel. One of these interrupts is permanently wired as a single-instruction interrupt (I200) and the others (I201-I211) are used in conjunction with branch-and-mark-place instructions to enter interrupt subroutines. For the present experiment, three interrupts are wired to the internal 1/10 second clock pulses (I200, I210, I216), two were activated by the beam interlock (I214-beam on, I215-beam off), and two could be manually activated from momentary pushbuttons by the operator (I211-IGO, I213-ISTOP).

A number of 24 bit parallel input lines are interfaced to experimental equipment and may be PINned (Parallel INput) directly to memory. Devices so interfaced for this experiment include three 100 mhz scalers, two DVMs (Digital VoltMeter), and two six digit sets of decimal thumbwheels. Data may also be POTted (Parallel OuTput) from memory to two 9 bit DACs (Digital to Analog Converters) which are used to provide X-Y displays on a point-plotter, storage oscilloscope, or standard X-Y CRT (Cathode Ray Tube). (This latter facility is used to generate a dynamic graphics display on a long persistence CRT screen; to enhance legibility, the CRT screen is televized with a closed circuit camera and displayed on a monitor above the synchrotron's control desk). In addition to the full-word data transmission capabilities, a variety of single-bit external control lines are employed. These are divided into EOM lines (Energize Output "M") and SKS lines (Skip-if-Set). EOM lines are used to turn on and off the synchrotron beam, to gate the beam injector, to control the discharge solenoid for the ionization chamber, and to zero the scalers. The SKS lines are used to test the ready status of experimental devices and the state of several operator activated sense switches and sense lights.

Method of operation

The mathematical framework of the least-squares fit and dose correction approximations are detailed in Appendix A. The concern here shall primarily be the functional and operational aspects of the program. A block diagram of the program transfer paths is given in Figure 21, the major flowlines of data transmission and communication are illustrated in Figure 22. Simplified flowcharts, indicating major functions of the subprograms are given in Figures 23 to 29.

For purposes of clarity, it is desirable to define some operational terminology and discuss the design concepts associated with these terms.

Clocks and timing All critical timing is derived from the I200 (single instruction) interrupt. It will be recalled that this is a 1/10 second interrupt and has the highest priority of all of the experimental interrupts; it is programmed here to increment a counter location TSCLK (tenth second clock). A number of other "clocks" are serviced in the CLK 210 routine and the timing for these clocks is always based on 1 second intervals defined by TSCLK. Rather than reseting TSCLK to zero each second, the clock is instead decremented by 10, thus a "lost" interrupt of the CLK 210 routine (caused by the unlikely possibility that CLK210 activities exceed 1/10 second) will be "caught up" on succeeding occurrences. Since there is negligible probability of the I200 interrupt being lost, the integrity of the timing is thus ensured.

Real-time MULTIFACTØRY maintains running clocks of seconds, minutes, hour (0-24), and day which are initially correlated with standard (wall clock) time and are thereafter used for logging and run identification purposes.

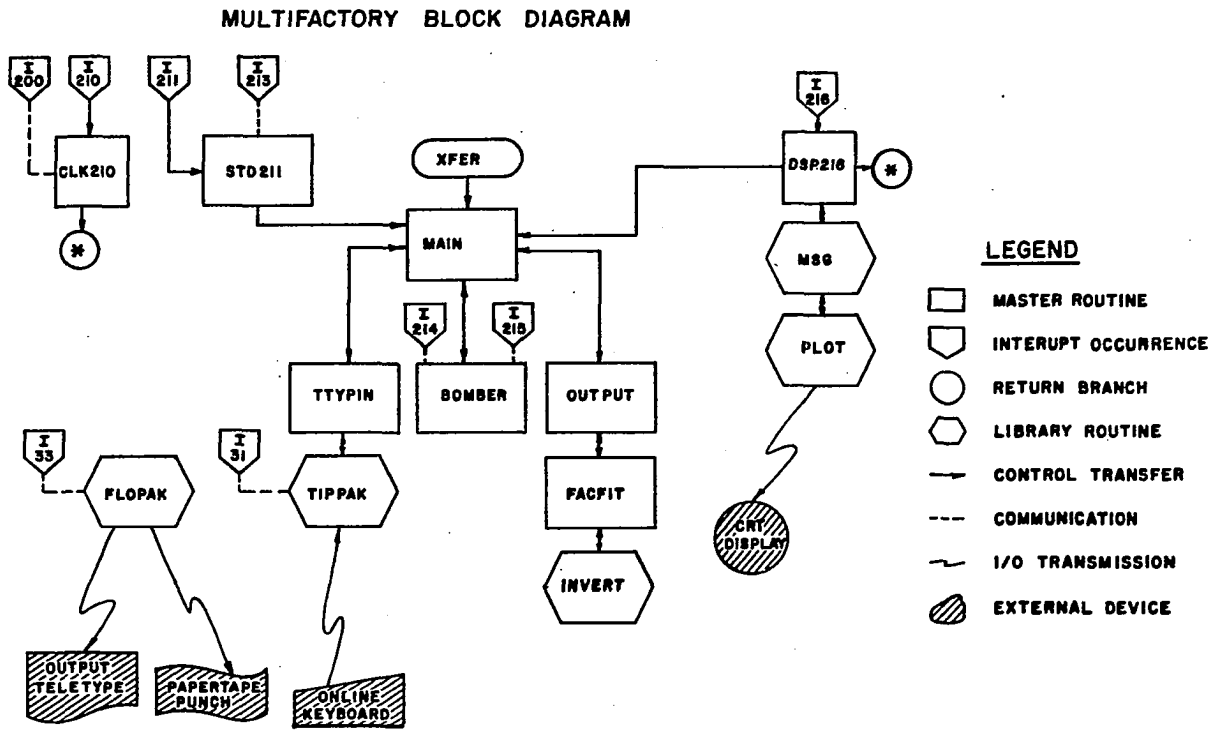

Figure 21. Block diagram of MULTIFACTORY routine indicating control transfers.

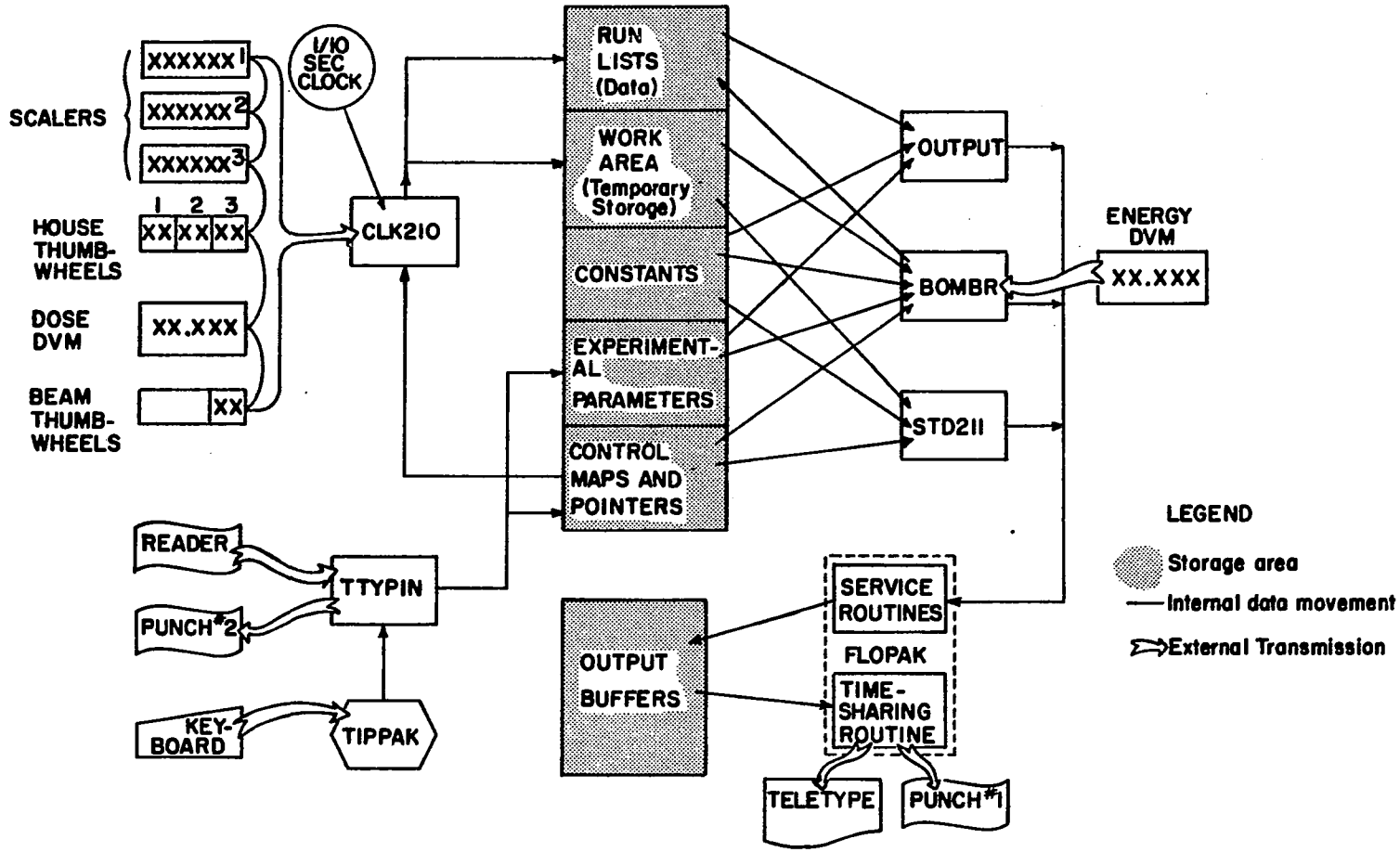

Figure 22. Schematic of internal and external data transmission in the MULTIFACTORY routine.

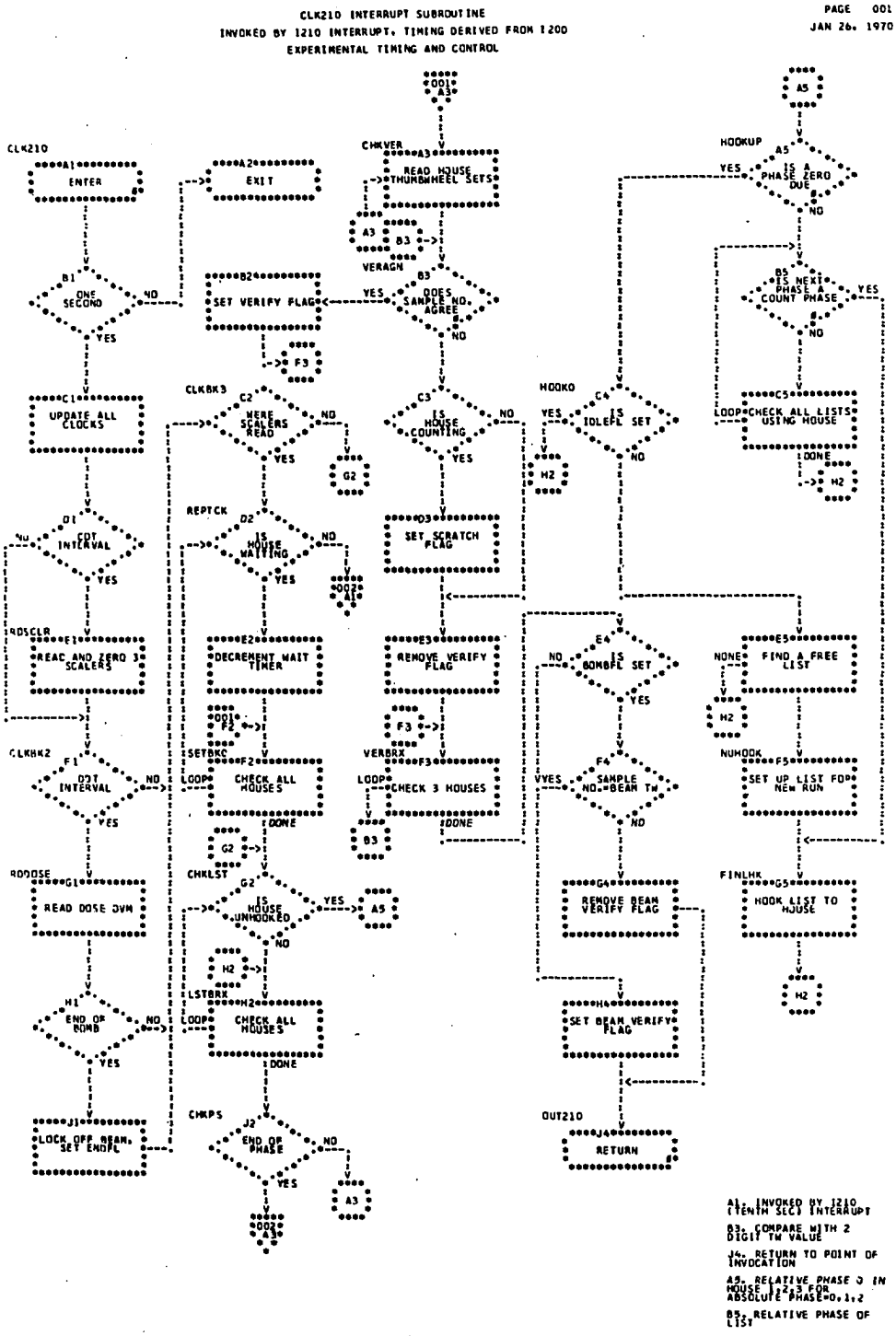

Figure 23. Flowchart for the CLK210 interrupt subroutine, Part 1.

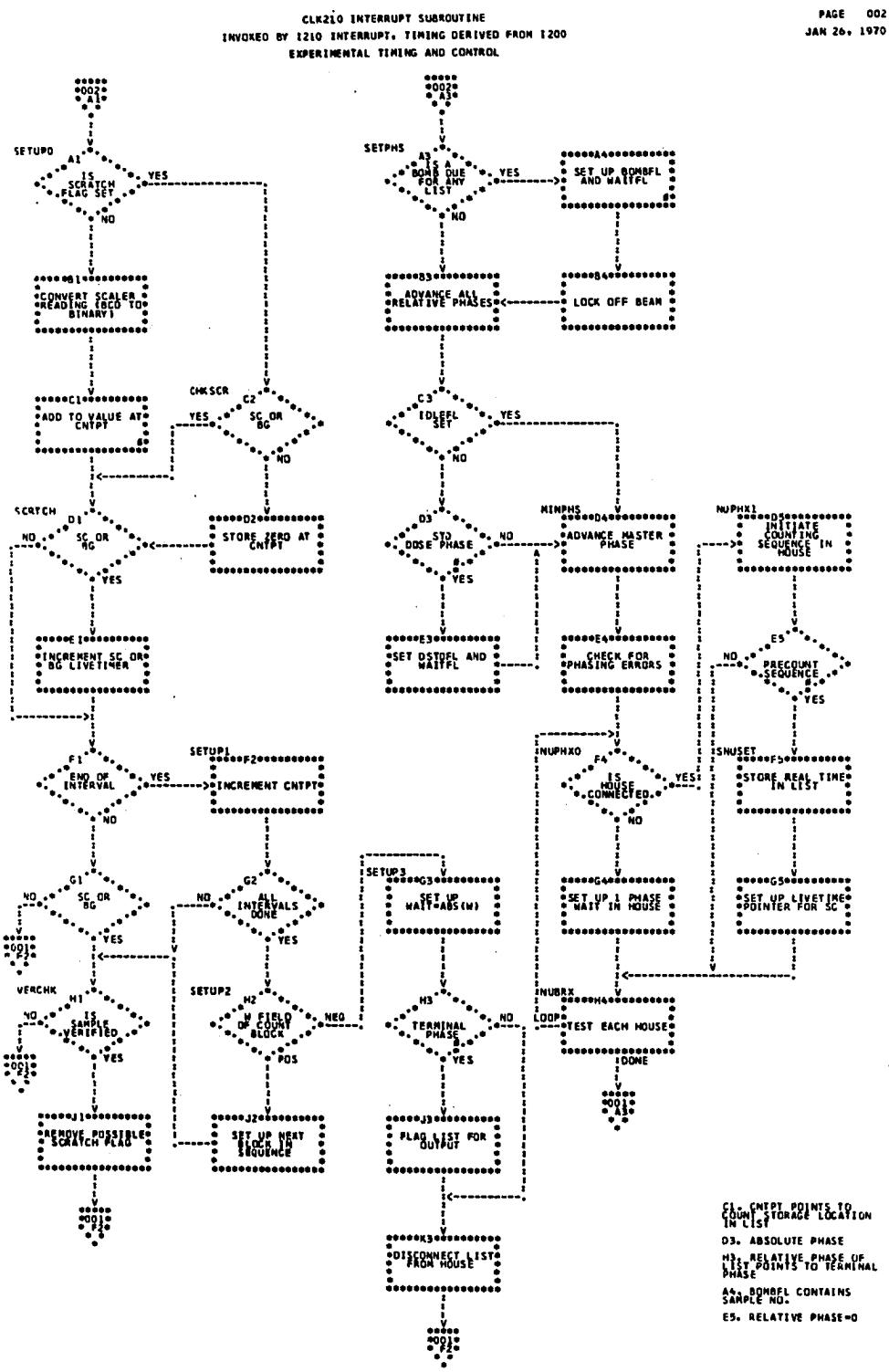

Figure 24. Flowchart for the CLK210 interrupt subroutine, Part 2.

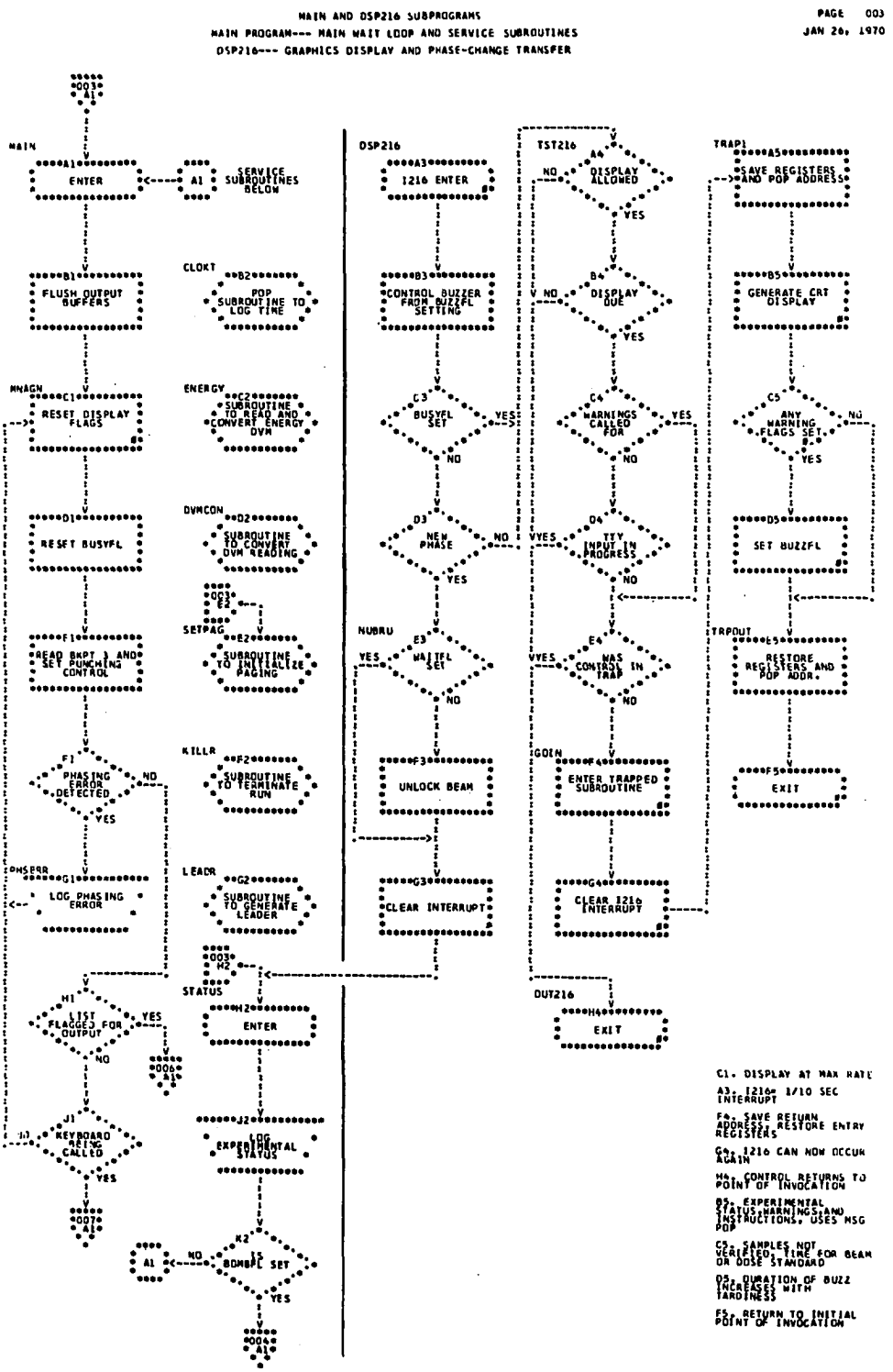

Figure 25. Flowcharts for the MAIN subprogram and the DSP216 interrupt subroutine.

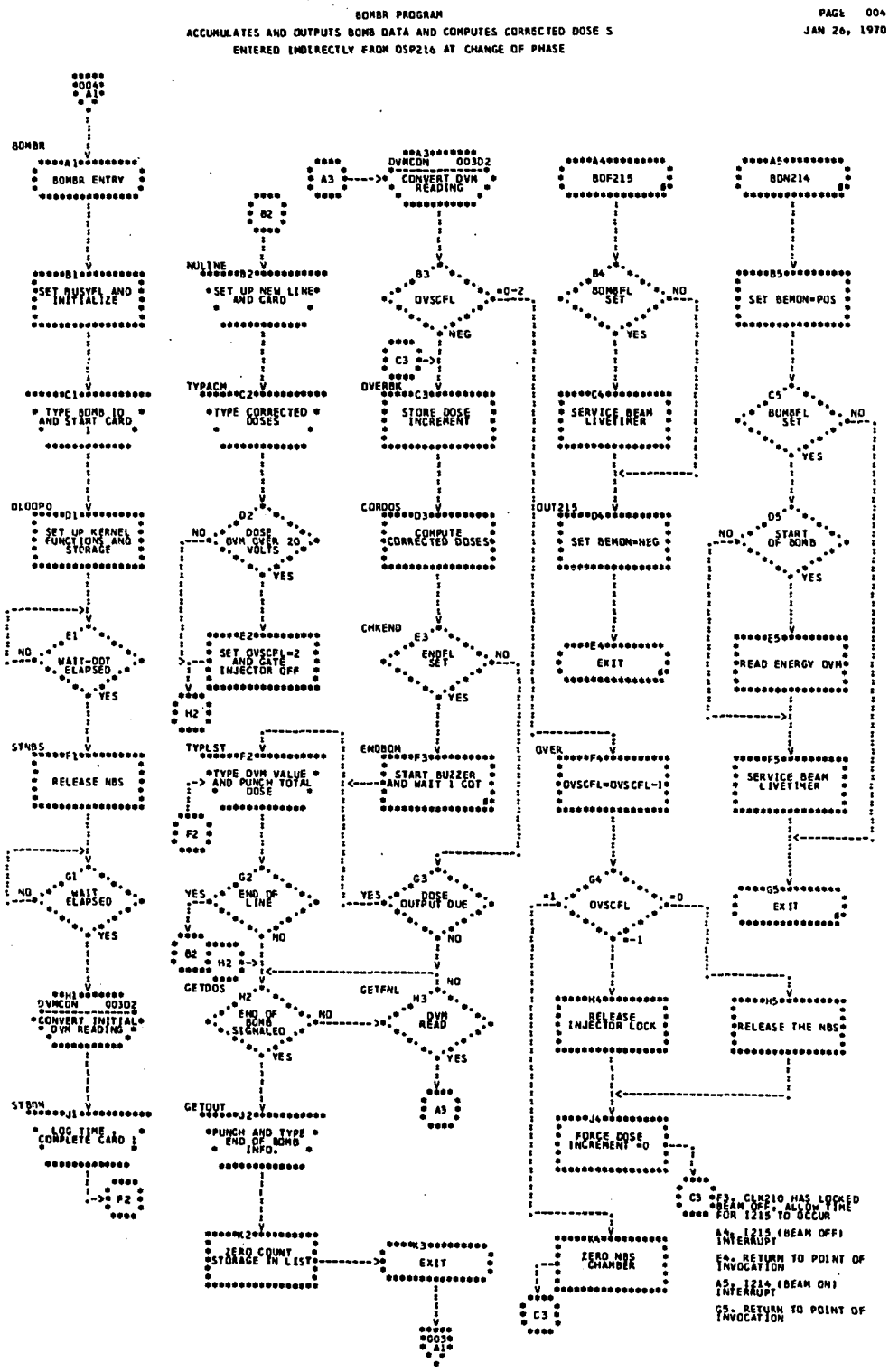

Figure 26. Flowchart for the BOMBR subprogram.

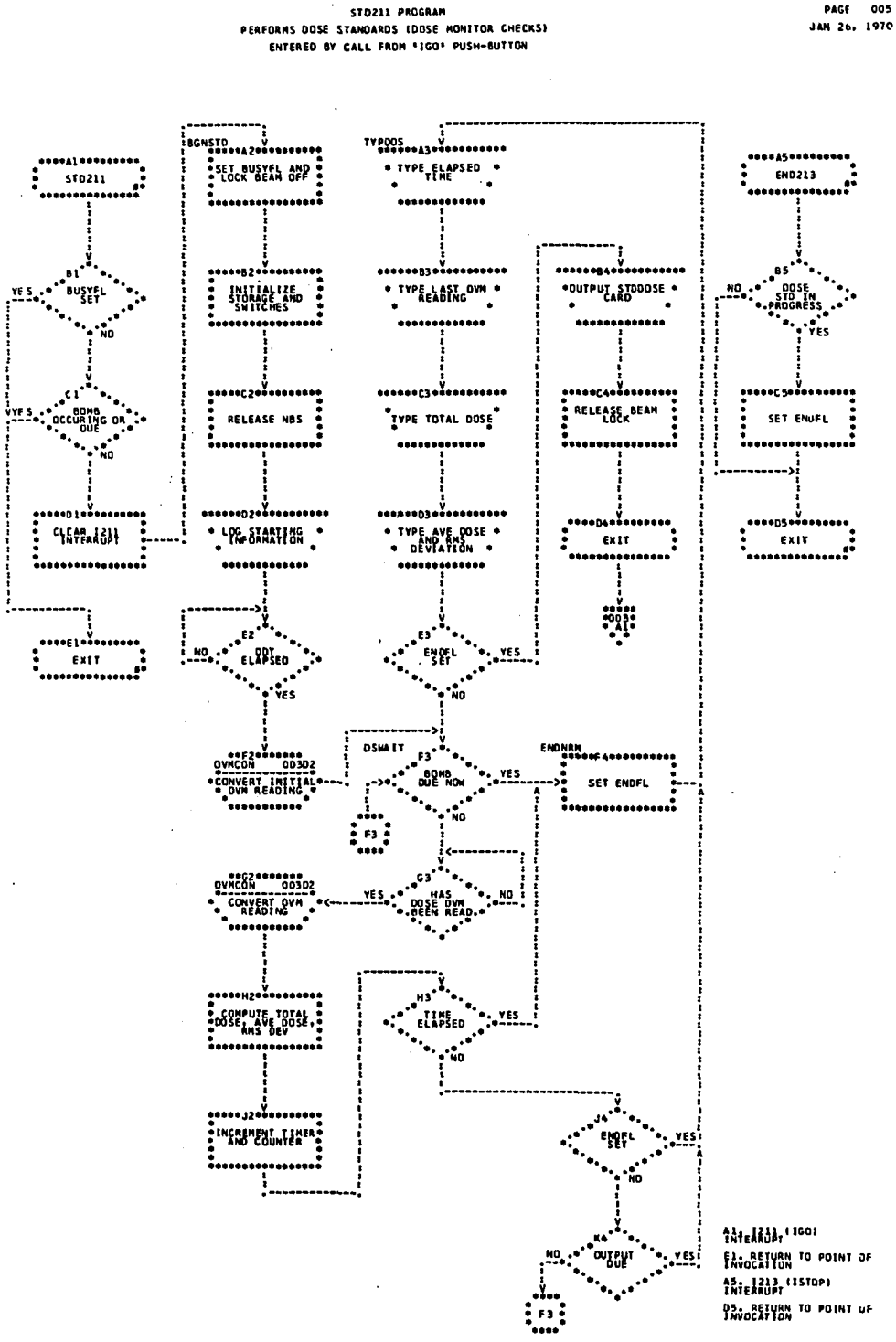

Figure 27. Flowchart for the STD211 subprogram.

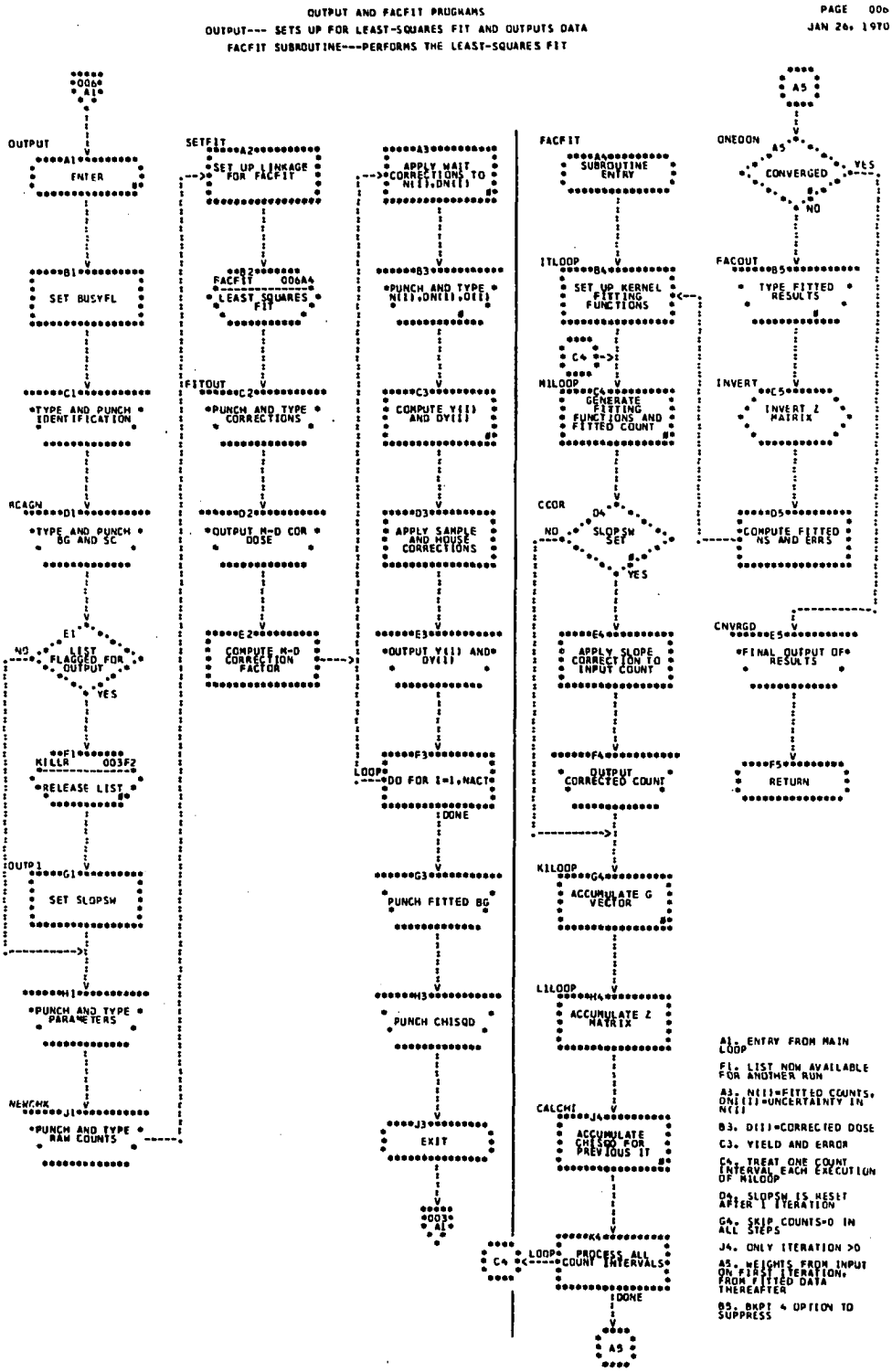

Figure 28. Flowcharts for the OUTPUT and FACFIT subprograms.

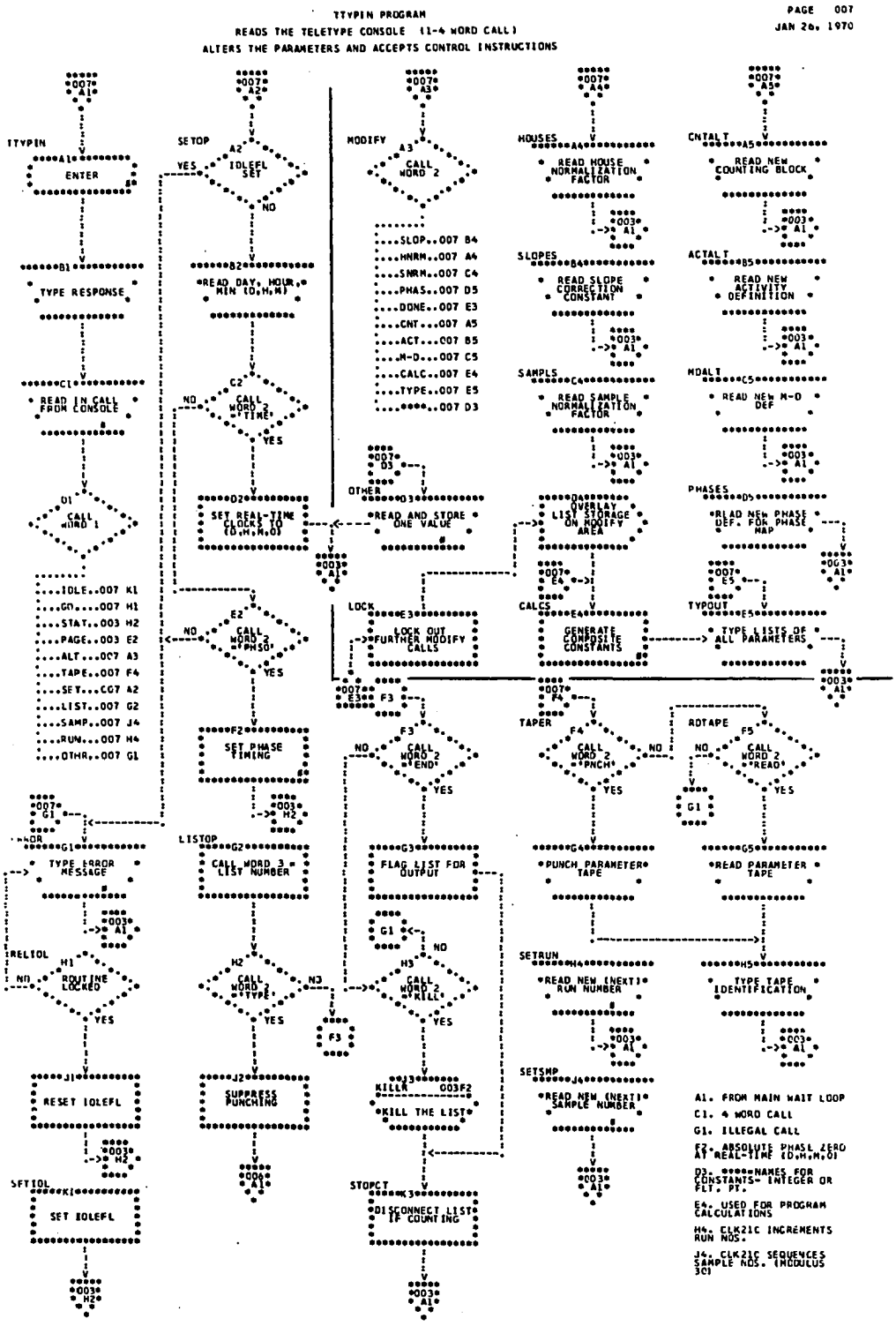

Figure 29. Flowchart for the TTYPIN subprogram. The MODIFY section is overlay-defined as data storage when set-up has been completed.

Delta-clocks Two interval clocks are maintained for experimental event timing and are referred to as CDT (Counting-Delta-Time) and DDT (Dose-Delta-Time) respectively. The scalers are read and reset each CDT interval (typically 15-30 seconds) and the dose DVM is read every DDT interval (typically 2-5 seconds). Nearly all other experimental timing units are defined as integral numbers of CDT or DDT units.

Phase The phase is the gross unit of time used for program control. Initiation and termination of major operations is defined with respect to the phase boundaries. The length of the phase is an arbitrary parameter defined by the user but it is usual to specify the phase length and initialization to correspond to convenient real-times (eg. phase change concurrent with wall clock hour or quarter hour). The (absolute) phase counter is a modulus counter and the modulus (PHSREP) is user specified (eg. PHSREP=8 implies that the absolute phase runs from 0-7). The delta-time intervals are required to be integral subdivisions of the phase interval (but otherwise arbitrary) and the delta-time clocks are initialized with respect to the phase boundaries. The integrity of the three clocks (phase, CDT, and DDT) is thereafter tested at the phase boundaries and error messages are logged if discrepancies are noted (no errors have ever been observed).

Cycle The interval phase-time=0 to phase-time=0 is defined as a cycle. Basically, the cycle is the largest control interval of the MULTIFACTORY routine; the program functions are identical from cycle-to-cycle.

Experimental control The sequence of experimental operations is defined by the user by the creation of a phase map. This map is a sequence of 30 words stored in memory, each word (numbered zero through 29) is coded

to specify the action(s) to take place during a phase.

Relative phase Each run has associated with it a relative phase "pointer" stored in memory. This pointer is initialized to the phase-zero position in the phase map when the run is initiated and thereafter incremented at each phase boundary. The location of this pointer in the phase map is thus the relative phase of the run (actually, the phase pointer precedes the current relative phase of the run so that activities scheduled to occur in the next phase can be anticipated), and each location in the phase map (30 locations numbered 0 to 29 are currently available) is coded to indicate the run activities during that phase. Three relative-phase operations are defined: 1) count phase (the run is "hooked-up" to the appropriate counting house), 2) bomb phase (bombardment of the sample is scheduled), 3) terminal phase (the accumulated data is processed and the run is terminated).

Absolute phase The absolute phase is the phase specified by the modulus-PHSREP phase counter, and specifies the status of the entire experiment with respect to the current cycle. The first three locations (0,1,2) of the phase map are permanently coded to specify that runs are to be initiated for houses 1, 2, and 3 during these phases. Thus, three runs (each in a different house) are initiated (and terminated) during each cycle. The user may also specify that a dose monitor check (STD dose) is to be called for during one or more phases of a cycle. The distinction should clearly be noted between the absolute phase and the relative phase of a run; the first specifies experimental activities to be performed on a cycle basis, the second specifies the actions to be performed for a specific run during a given phase. Since the absolute phase defines the initiation

of relative phase acitivites, every relative phase function will be performed three times for each cycle, but functions are performed in successive phases for houses 1 to 3.

Count accumulation Each run has an associated count storage location in which the counting information is stored. Using the interleaved counting scheme, the data accumulation process is broken into periods of counting activity and "cooling" periods. During a counting period, the sample is in the counting house and the radioactive decays are detected and counted. During the cooling periods, the sample is removed from the counting house and "cools" until the next counting period. Interleaved counting implies that the counting and cooling periods of samples using the same house are defined such that one sample is counting while the others are cooling. In practice, this means that, although the total counting activity (counting schedule) can span several cycles, the counting activity for a run can involve each absolute phase only once (cf. Figure 6).

Counting interval A counting interval is specified as an integral number of CDT intervals. The counts accumulated during the one or more CDT intervals are added and the accumulated total is stored in the appropriate count storage location at the end of the counting interval. The counts accumulated during the counting intervals are thus the "data points" which will be fitted to by the least-squares fit.

Counting block A counting block is defined as a series of N counting intervals, each of width I (in CDT units), and followed by a "wait" of width W(also in CDT units). Operationally, the block is defined by a set of 3 adjacent memory locations (N,I,W) and the W field also is coded to indicate subsequent action. If W is positive, the next block in sequence

will be executed following the wait, if negative, counting activity for this run is discontinued and a run scheduled for counting during the next phase is hooked-up; if the current relative phase of the discontinued run is the terminal phase, the run is then flagged for output, if not, it becomes inactive until the next counting phase is reached. A -W field thus defines a wait period for performing the sample change -- no sample change occurs during a +W wait. Five general purpose counting blocks (A-E) and two special purpose blocks (+,√) are available to the user. The latter two blocks are permanently specified as single interval blocks (I=1) but are otherwise arbitrarily defined by the user. These blocks are used to define the SC (Standard Count) and BG (BackGround) precount intervals.

Counting Sequence A counting sequence is defined as a series of one or more counting blocks linked together by +W fields and terminated by a -W field. The sequence is initiated by the occurrence of a counting phase in the phase map (coded to specify the first block) and is terminated only when a -W field is accessed. A given block or set of sequential blocks may be used in more than one sequence; the starting point of the sequence is the block specified by the phase map. The only constraint is that sequences are required to be defined so that their total length (sum of all counting intervals and waits) is an integral number of phases; that is, the sequence must begin and end on a phase boundary but may span several phases. A distinction is drawn between the time that a sequence is "hooked-up" and the time that it is "activated". The sequence is hooked-up (set up for counting from a given house for the appropriate run) whenever the routine detects that the subsequent relative phase of the run is a count phase and no other run is currently hooked-up to the

required counting house. The sequence does not become active until execution of the counting sequence actually begins. Since runs are unhooked (disconnected) at the occurrence of a -W field, the hook-up will occur prior to the phase boundary whereas activation occurs precisely on the phase boundary. (In some cases, a run is not using the house during the preceding phase and the hook-up occurs a full phase before activation.)

Counting schedule The term "counting schedule" is used to refer to the complete set of counting sequences and cooling periods which define the count accumulation process for a run. The first phase(s) of the schedule is always a precount sequence (SC and BG intervals) and a bomb phase is typically scheduled shortly after the precount sequence. The schedule is always terminated by a terminal phase.

Sample verification Associated with each counting house there is a two digit thumbwheel set (the three sets comprise a single 24 bit PIN line) which is used to verify the physical status of a counting house. Counting data is not accumulated unless the thumbwheel setting agrees with the sample number (01-30 for samples, 00 for the Na^{22} source) requested by MULTIFACTORY. For the A-E blocks, non-verification during any part of a counting interval causes the interval to be flagged as a "scratch" interval. The storage location associated with a scratch interval is forced to be zero and all such intervals are skipped in the subsequent least-squares fit. In the case of the SC and BG intervals, counts are accumulated only while the sample number is properly verified and associated "livetime" locations record the accumulation times. A similar thumbwheel pair is used to verify the placement of the sample in the beam position -- the beam is locked off whenever the thumbwheel setting is incorrect.

Data storage Each run in progress has associated with it a storage area referred to as a "run-list" (or simply, "list"). All data accumulated for a run (corrected doses, counts, SC and BG livetime, bombardment energy, seconds of beam time, etc.), run identification (run number, house number, sample number, phase-zero time), and control information (relative phase pointer, current position in count storage) are stored in this list. A total of 12 such lists are currently used and each list has a length of 122 words, of which 100 are reserved for count storage (an additional 4 are used for the precount block counts and livetimes) and 10 are used for the corrected doses (4 corrected doses plus a mother-daughter corrected dose). The first word of each block (LISTSW -- the relative phase pointer) is coded to indicate whether the block is busy or free, the counting house used, and termination (call for output). All control and identification information is set up at the time of the initial hookup (in CLK210) but the dose and count storage is not cleared until the bomb phase; at termination the OUTPUT routine frees the block for further use as soon as the initial information has been output so that the list may be hooked up for a new run during the least-squares fit and final output of the old data.

Library subroutines

A number of standardized SYMBOL subroutines have been developed by this author to facilitate the construction of experimental programs. Most of these are of the POP (Programmed OPerator) variety, and thus are particularly convenient. (The essential feature of a POP subroutine is that it is invoked in the same manner as a hardware instruction; the POP instruction may have an operand and the operand address may be indexed or indirectly addressed). The library routines used in MULTIFACTORY are briefly described

below.

MADDOT The MADDOT package contains two POP subroutines which facilitate the manipulation of matrices and vectors. MAD (Matrix ADdressing) allows the user to access the elements of rectangular matrices and vectors in a simple and concise manner. A simple matrix descriptor is used to define each array storage area; overlayed arrays and array "sections" may be employed. DOT (DO Terminator) allows Fortran-like "DO-loops" to be simply programmed. DOT loops may be nested to any level and may share indices.

INVERT The INVERT subroutine is used to invert square matrices of any dimension. The Gauss-Jordan method is used with double-precision arithmetic (39 bit mantissa). Matrices are defined by the MAD format conventions.

FLOPAK An inclusive set of buffered output subroutines are included in the FLOPAK package. Output devices currently supported by the FLOPAK routines are the high-speed paper tape punch and the Teletype printer, the device is selected by a normally unused bit in the instruction word.

FLO The FLO (POP) routine is the central routine used by the entire package and is available to the user for outputting lengthy standardized messages. The operand of the FLO call specifies the address of a formatted output block and bit 0 of the call specifies the device. Control words are formed from the input information and placed in an output queue. Occurrence of the I33 (End of transmission) interrupt activates an interrupt subroutine which supplies the interlace register with a new control word from the queue. The output of each message block is handled entirely by the interlace register on a hardware time-sharing basis.

Stream output A number of routines are provided which allow

the user to output unformatted words and strings. The output is packed in 20 word (80 character) blocks and placed in the FLO queue when filled. Separate blocks are maintained for the output devices and partially filled blocks may be placed in the output queue upon demand. Several of the routines perform data conversion (internal to graphic) prior to storage.

Service routines These routines provide for a variety of conversion and output-related operations. Spacing and paging operations are supported (paging is automatic) and punched records may be labelled.

TIPPAK The TIPPAK package is written to allow convenient input from the Teletype console. Three POP subroutines are used to input the data types: AIN reads variable length alphanumeric input strings and performs no conversion. NIN accepts 1-8 character integers in standard integer format and converts to internal integer (1 word fixed-point) form. FIN accepts both integer and standard floating point (F or E format) input formats and converts to double-precision floating-point internal form (39 bit mantissa, 9 bit exponent). The input formats are very flexible for each of the routines, but obvious syntax errors and read-parity errors are detected.

Plotting package Two subroutines, PLOT and LINPLT are used to support X-Y plotting (point plotter or CRT device). The first positions a single point and the latter draws the best fit to a straight line segment (any length and orientation) on the 512 x 512 display grid.

MSG The MSG POP is used to generate graphics for plotting on the point plotter or CRT tube (uses PLOT and LINPLT). The device is selected internally and the scaling of the display can be selected from external sense switches or determined by the program. A 61 character graphic set

plus 5 special control characters is supported. The input uses formatted messages with the same format conventions used for the FLO routine. Character and line spacing is automatic.

The POST-MULTIFACTORY (PMF) Routine

The PMF routine is a special purpose routine, written in the PL/1 language, for the IBM 360/65 computer. The program utilizes a private disk pack on an IBM 2314 disk drive for data storage. The program consists of 15 separately compiled operational subroutines and a compact main routine which routes the program control. The subroutines are overlay-defined and use controlled storage areas to enable the routine to run in a 128k (byte) memory area. The PMF routine itself is stored on disk and is invoked by the JCL (Job Control Language) cards supplied by the user.

Direct-Access files

A number of data storage and temporary work files are defined as files on the disk pack. All files are "keyed direct" (Regional (1) organization) and thus the records contained in a file may be accessed in random sequence by specification of an integer key. All data is stored in internal form.

Data files The four data files each contain one record for each run number; the n^{th} run is associated with the j^{th} record in each data file. The run number and key are related by j=n-IDISP, where IDISP is the smallest run number (IDISP=25 in this case). Two of the data files (CRDFILE,PREFILE) are permanent and, with only minor exception, are opened only as DIRECT INPUT files by PMF. The other two files (TMPFILE,RESFILE) are temporary files altered by PMF and are declared as DIRECT UPDATE.

CRDFILE All of the data associated with a MULTIFACTORY run is

stored in one of the CRDFILE records. Specifically, each record contains the run identification, precount data, counting information (data and parameters), dose information (dose increments and MULTIFACTORY corrected doses), all fitting parameters used by MULTIFACTORY, and the MULTIFACTORY fitted results. The records also contain a number of identification and warning flags supplied by the input routine (MFEDIT).

PREFILE The precount information for each run (SC and BG counting information) is duplicated as a record in the PREFILE file. The records of this file are used to link the sample decay for the run currently being fitted (from a CRDFILE record) to the subsequent precount data.

TMPFILE The TMPFILE records are used for storage of the PMF fitting parameters and fitted results.

RESFILE The PMF fit for each run is used to generate residual activity information which is stored in a RESFILE record. The record associated with a given run contains the residual activity information (residual BG, and activity amplitude of each half-life component) extrapolated from the PMF fit of the preceding run which used the same sample. The records are flagged with an identification string (supplied by the user) which identifies the record as having been obtained with a specific set of fitting parameters; the RESFILE flag must be found to agree with the current flag before the record can be used.

Access files Two access files are used to access the data files in proper sequence. Both files are permanent and are opened by PMF only as DIRECT INPUT files.

MASTER There are four records in the master file, each is an ordered list containing one entry for each run. Each entry is composed of

five data items: the run number, sample number, counting-house number, bombardment energy, and access "key" number. The four lists are each sorted in ascending sequence on one of the first four items.

SMPFILE Thirty records, one for each sample, are contained in the SMPFILE file. Each of the records contains entries identifying the runs which used that sample. The entries are sequential by run number.

Setup

The punched paper tape output from the MULTIFACTORY routine is converted to punched cards. The MULTIFACTORY output for a run consists of two "decks" of punched cards: 1) BOMB deck -- the total dose values for the bombardment plus identification and timing parameters; 2) RUN deck -- the accumulated counts, identification, experimental parameters, corrected doses, and fitted results. All of the experimental information accumulated for a run is explicitly stated by the two decks and all of the experimental parameters (timing information, correction factors, etc.) are stated or may be inferred. Since the BOMB deck is output during the BOMB phase of a run and the RUN deck following the terminal phase, the two types of deck are generally not sequential in the MULTIFACTORY output stream.

A separate input routine (MFEDIT) is used to read in the MULTIFACTORY decks and store the information in the permanent files. The input is accepted in arbitrary sequence, the BOMB and RUN decks being treated separately, but both are merged in the same CRDFILE record. MFEDIT performs a number of editorial functions and consistency checks; specifically, all timing information (defined by MULTIFACTORY in delta-time and phase units) is converted to seconds and the cards of each deck are sequence checked. Any errors, either in card syntax or input sequence cause the entire deck

to be rejected but do not destroy the information already accumulated from the other deck associated with the run. The access files are initially accumulated in order of deck appearance and after all decks have been read are then sorted and stored. Several "marginal" conditions are tested and warnings are generated when discrepancies are noted in the input data (eg. dose increment amplitudes outside of reasonable limits). Following the final sorting operations, a library listing is generated for documentation.

Operation control and parameter definition

A number of functions are performed by the PMF routine, these include output and editorial functions in addition to the basic fitting operation. All of the PMF parameters and operations are specified by a set of control cards. Seven basic types of control cards are used, each is identified by the appearance of a keyword followed by a colon as the first string appearing on the card; the remaining control card items may appear in any order in a free-form format. Unspecified parameters are assigned default values.

PARM The PARM keyword specifies that basic fitting parameters will be specified on the card. The item keywords are:

NACT = number of activities to be fitted.

MOTHR = the serial number of the mother activity.

DAUTR = the serial number of the daughter activity.

TAG = a 20 char string used to identify the fitting configuration.

CONV = the fitting convergence condition, specified as the ratio of change between iterations to

five data items: the run number, sample number, counting-house number, bombardment energy, and access "key" number. The four lists are each sorted in ascending sequence on one of the first four items.

SMPFILE Thirty records, one for each sample, are contained in the SMPFILE file. Each of the records contains entries identifying the runs which used that sample. The entries are sequential by run number.

Setup

The punched paper tape output from the MULTIFACTORY routine is converted to punched cards. The MULTIFACTORY output for a run consists of two "decks" of punched cards: 1) BOMB deck -- the total dose values for the bombardment plus identification and timing parameters; 2) RUN deck -- the accumulated counts, identification, experimental parameters, corrected doses, and fitted results. All of the experimental information accumulated for a run is explicitly stated by the two decks and all of the experimental parameters (timing information, correction factors, etc.) are stated or may be inferred. Since the BOMB deck is output during the BOMB phase of a run and the RUN deck following the terminal phase, the two types of deck are generally not sequential in the MULTIFACTORY output stream.

A separate input routine (MFEDIT) is used to read in the MULTIFACTORY decks and store the information in the permanent files. The input is accepted in arbitrary sequence, the BOMB and RUN decks being treated separately, but both are merged in the same CRDFILE record. MFEDIT performs a number of editorial functions and consistency checks; specifically, all timing information (defined by MULTIFACTORY in delta-time and phase units) is converted to seconds and the cards of each deck are sequence checked. Any errors, either in card syntax or input sequence cause the entire deck

to be rejected but do not destroy the information already accumulated from the other deck associated with the run. The access files are initially accumulated in order of deck appearance and after all decks have been read are then sorted and stored. Several "marginal" conditions are tested and warnings are generated when discrepancies are noted in the input data (eg. dose increment amplitudes outside of reasonable limits). Following the final sorting operations, a library listing is generated for documentation.

Operation control and parameter definition

A number of functions are performed by the PMF routine, these include output and editorial functions in addition to the basic fitting operation. All of the PMF parameters and operations are specified by a set of control cards. Seven basic types of control cards are used, each is identified by the appearance of a keyword followed by a colon as the first string appearing on the card; the remaining control card items may appear in any order in a free-form format. Unspecified parameters are assigned default values.

PARM The PARM keyword specifies that basic fitting parameters will be specified on the card. The item keywords are:

NACT = number of activities to be fitted.

MOTHR = the serial number of the mother activity.

DAUTR = the serial number of the daughter activity.

TAG = a 20 char string used to identify the fitting configuration.

CONV = the fitting convergence condition, specified as the ratio of change between iterations to

uncertainty in the fitted coefficient.

DRIFT = the dosemonitor drift per second to be subtracted from the dose increments.

ITS = the maximum number of iterations to be performed.

AVEMR = the serial number of the storage location from which the average mother activity is to be obtained for the daughter correction (if zero, the fitted mother activity is used).

ACT(X) The values to be associated with the X^{th} activity will be specified on this card. The item keywords are:

HL = the halflife (in seconds) of the activity.

EPS = the fraction of positron emission for this activity.

NAME = an 8 character name to be associated with the activity.

THRESH = the threshold (in mev) for the reaction creating the activity.

JOINT = the serial number of another activity; when specified the program computes, in addition to the fitted coefficient and statistical error of the X^{th} activity, the sum of the X^{th} activity and the activity specified and the uncertainty in this value.

FREE the appearance of the word FREE specifies that the program is to fit for the halflife, as well as the coefficient, of the X^{th} activity (when not specified, the halflife is assumed fixed by default).

SLOPE(H) The slope correction constant(s) to be used for the H^{th} counting house are specified on this card. The general form is

SLOPE(2): FROM=val_1, TO=val_2, BY=val_3

which specifies that the least-squares fit for each run using house 2 is to use the slope correction constant values running from val_1 to val_2 in increments of val_3. If the TO and BY values are not specified, only the FROM value is used.

SELECT The access sequence and range of runs to be treated are selected by this card. Up to four SELECT cards are used to specify the run number, sample number, house number, and bombardment energy limits. A typical set of cards might be

SELECT: RUN_NO FROM=30 TO=400

SELECT: ENERGY MAJOR FROM=15 TO=30

SELECT: HOUSE FROM=2 TO=2

This selection specifies that all runs (within the other limits) with bombardment energy of 15 mev will be accessed first, then those with energy=16 mev and so forth to energy=30 mev. The minor limits are specified to be runs in house 2 with run numbers from 30 to 400. Since sample numbers are not specified, by default the limits are samples 1 to 30. The minor sequence of access is always run number (and if a MAJOR sequence is not specified, the default is RUN_NO).

OUTPUT The data to be output during a LIST operation (explained below) is specified by this card. The possibilities are:

DATA print the (MULTIFACTORY) data for the run (CRDFILE data).

RSLTS print the fitted results obtained by PMF (TMPFILE and RESFILE data).

YLDS print only the yields and uncertainties obtained by PMF (stored in TMPFILE).

PREC list the precount information (PREFILE data).

SMPL list the sample usage (SMPFILE information).

LIB list the entries in each of the MASTER records.

ALL list all of the above.

SPARE controls the paging.

OPTIONS The least-squares fitting options will be selected on this card. The option keywords are:

OP1 use the raw BG value in the least-squares fit as a data point at "infinite" time.

OP2 use the BG value of the next run using this sample as a data point in the least squares fit.

OP3 use the residual BG point (see MODE option below) as a data point at infinity and also subtract the extrapolated components from the fitted coefficients.

OP4 extrapolate the residual activity information and store in RESFILE.

OP5 use the activity subtraction option (see SUBTR and MODE below).

OP6 store the residual activity data regardless of convergence (if not specified, the residual activity information is flagged when there is not convergence, and the subsequent run will not use this information).

OP7 calculate new corrected doses (if not specified, the MULTIFACTORY corrected doses are used).

OP8 output the counting data at the end of the least-squares fit.

SUBTR=XXXXX (each X=0 or 1) if OP5 is specified, the average activity value stored in the position corresponding to an X=1 is subtracted from the count data prior to fitting.

MODE = several modes of computing the residual BG value may be specified. The modes are: N-normal, subtract extrapolated fitted activity from BG; X - subtract the average activities specified by the SUBTR item from the raw BG value; F - use the fitted background as the residual BG value; B - apply both N and X modes to BG; Z - force the residual BG value to be zero; S - special mode which causes the X-mode BG values to be calculated and stored in RESFILE and suppresses the least-squares fit.

OPER This card specifies that a particular operation is now to be performed; no further control cards are read until the operation is completed. The operations are:

FIT - perform the least-squares fit and yield computation for all runs selected. The user may also specify FROM=nlow TO=nhigh on this card (nlow= serial number of first counting interval, nhigh= serial number of last interval), if not specified,

all counting intervals are fitted.

DECK - punch APU cards for the runs selected. The name of the activity to be punched must be specified by NAME= a current activity name as specified on the ACT(X) card. The user may also specify CURVE= the curve number to be punched on the cards, and LABEL= a four character label to identify the APU deck (punched in columns 77-80).

ALTR - accept alteration cards and alter the contents of the "permanent" files (the possible alterations will be discussed later).

LIST - print the information specified by the selection limits and the OUTPUT options.

STOP - terminate the PMF run.

Alteration of data files

Although the permanent data files are initially set up by the MFEDIT routine and are thereafter normally used only for input, PMF allows the user to perform limited modifications of the permanent data. In the main, the user is restricted to altering the warning and control flags and the "average activity" storage areas, but he may also alter the values of the count and dose increment storage locations (this option is provided for dealing with incorrect values resulting from experimental equipment malfunction).

The "average activity" storage area is a set of five entries in each CRDFILE record which the user can employ to specify average activity values of known components. The user specifies the halflife of the

activity to be stored and the storage location to be used. He then specifies a yield value for each bombardment energy. When all yield values have been read in, the routine then computes the corrected dose (using the specified halflife) for each of the runs. The total activity corresponding to the corrected dose and yield is computed and stored as the specified item. Using the SUBTR option, the user may then request that subsequent fitting operations subtract this activity from the counting data prior to the least-squares fit. This option allows the user to eliminate "known" contaminating activities from the least-squares fit. When used with the AVEMR parameter, it allows the mother-daughter correction to be based upon the average mother-activity yield.

The ANTEPENULTIMATE (APU) Routine

The APU routine is a general purpose Fortran routine which is used to convert "raw" experimental data into reduced yield curves suitable for processing by the CLSR (least structure) routine. A number of data listing and curve plotting functions are also supplied for the convenience of the user. The routine (in the version used for this experiment) operates in 128K (bytes) on the Iowa State University IBM 360/65 computer.

Input deck

The input to the APU routine consists of a set of punched cards or "deck", each card of which contains a group of 10 data items which describe a single yield measurement, that is, one activity obtained for a given run. In the present case, the APU decks were obtained from the PMF routine and a separate deck was punched for each of the reactions of interest. The data items which are input for each run include:

1) E_i - the bremsstrahlung peak energy of the bombardment.

2) V_i - the reference voltage used by the energy control system to determine the energy E_i.

3) N - the fitted number of radioactive nuclei present at end of bombardment due to the current reaction.

4) ΔN - the uncertainty in N as obtained from the least squares fit.

5) D - the corrected dose for this reaction.

The APU routine can deal with only one reaction at a time, and it is implicitly assumed that all cards in the input deck refer to the same reaction.

In addition to the data deck, two control cards are used to select the options to be used and additional correction decks may be required for the selected operations.

Final data corrections

The APU routines provides for the application of several user-defined data corrections. These corrections are independent of the type of reaction, being related only to the experimental equipment and technique. All of these corrections are applied as multiplicative corrections to the N or D values and are applied in such a way as to maintain the initial value of the ratio $\Delta N/N$.

Betatron dose correction It is necessary to make a small correction to the measured doses to account for the small amount of the electron beam which is accelerated during the betatron phase but which leaves the

orbit during the RF acceleration phase. The electrons which do not achieve RF orbit are spilled out and create a small amount of bremsstrahlung radiation as they strike the walls and target of the accelerator cavity. Since the maximum energy of the betatron acceleration is less than the threshold energy for the (γ,n) reaction, reactions are not induced in the sample but the dosemonitor does respond to this radiation. A multiplicative correction of the form $(1-(V_o/V_i)^3B)$ is applied to the measured doses to correct for this spurious "betatron dose". Here V_i is the reference voltage (roughly 1.4 volts/mev) and B is the measured fraction of betatron dose at reference voltage V_o. For this experiment B = .0404 and V_o = 14.423 which gives a correction of roughly 4% at 10 mev. This correction falls off very rapidly with energy and is only significant for low bombardment energies.

Dependence corrections APU allows the user to correct the experimental data for systematic dependence on several experimental quantities. Specifically, corrections are available for time-dependence, dose-dependence, count-dependence, energy-dependence, and sample-dependence. All of these corrections require the user to specify multiplicative correction values for values of the "dependent-on" quantity (argument). When the argument is continuously defined, as for time-dependence, dose-dependence, and count-dependence, the user specifies the vertex values defining a series of straight lines; the routine then interpolates the correction for the appropriate value of the argument. Further discussion shall here be limited to those corrections used in the present experiment.

Time dependent corrections The time dependent corrections are used to compensate for slow drifts of the counting system as a function

of time. In practice, the corrections are specified as values of the house normalization factors so that the correction actually represents a time-dependent normalization factor. A set of 8 line segments was adequate to describe the time dependence over the approximately 600 hours spanned by the present experiment.

Sample corrections The sample correction factors are actually the sample normalization factors which have been spoken of previously.

Energy dependence The energy dependent corrections are the dosemonitor response corrections, $F_M(E_i)$ defined by equation III.8. In terms of these corrections, the reduced yields are defined as

$$y_i = F_M(E_i)N/D \tag{C.1}$$

and the statistical uncertainties as

$$s_i = F_M(E_i)N/D \quad . \tag{C.2}$$

The set of F_M values is calculated from experimental values and the Schiff spectrum (cf. equation III.8) and the F_M curve is then smoothed repeatedly to ensure that spurious structure is not introduced into the yield curve. The same F_M curve is used for every data set.

Yield error analysis

The least structure method of solving for the cross section requires that the total random error of each yield measurement be known. In particular, the error d_i assigned to a yield measurement should reflect the reliability of the measurement and be a reproducible characteristic of the measurement. (For the following discussion the individual reduced yields and statistical errors will be written as y_{ij} and s_{ij} respectively, where

the subscript "i" always refers to the energy E_i of the bombardment and the "j" subscript is introduced to differentiate the n_i separate runs bombarded at energy E_i.)

As has already been mentioned, the statistical error s_{ij} is the random error of the reduced yield y_{ij} associated with the uncertainty in the least squares fit used to obtain y_{ij}. There are additional sources of random error which result in non-reproducibility of the yields y_{ij} (hereafter, reduced yields shall be referred to simply as "yields"). Such error will be referred to as "experimental error" and designated as e_{ij} so that the total random error in a measured value y_{ij} is written as

$$d_{ij} = (e_{ij}^2 + s_{ij}^2)^{1/2} \quad . \tag{C.3}$$

Stating the above in a different manner s_{ij} is the total random error of a yield measurement for a "perfect" experiment where measurement systems did not drift, samples are identical and always precisely positioned, all half-lives and parameters of the fit are precisely known, and so forth for all possible sources of error in the determination of the yields. For such a perfect experiment $e_{ij} = 0$ and $d_{ij} = s_{ij}$ (though proof of this statement is not attempted, experience indicates that the s_{ij} do indeed have this property -- that is they represent the minimum uncertainty of the results).

The standard deviation of the n_i yield measurements for energy E_i is defined as

$$\delta_i = \left[\frac{\sum_{j=1}^{n_i} (\bar{y}_i - y_{ij})^2}{n_i - 1} \right]^{1/2} \tag{C.4}$$

where

$$\bar{y}_i = \sum_{j=1}^{n_i} y_{ij}/n_i = \text{the average yield at energy } E_i. \qquad (C.5)$$

If n_i is sufficiently large, then $d_i \cong \delta_i$ but for the small number of measurements possible in any actual experiment, the uncertainty in the determination of δ_i is so large that it is not a satisfactory measure of the total error.

If e_{ij} can be expressed as a known function of the yield, then it is possible to use the entire set of yield measurements (for all E_i) to estimate the e_{ij} from the complete set of observed δ_i. An assumption which seems to be valid for most experiments is that

$$e_{ij}^2 = \epsilon y_{ij}^2 \qquad (C.6)$$

so that equation C.3 becomes

$$d_{ij} = (\epsilon y_{ij}^2 + s_{ij}^2)^{1/2} \quad , \qquad (C.7)$$

where $\sqrt{\epsilon}$ is the fraction of experimental error in a typical yield measurement and is a constant for the measurement. The basic assumption here is that the typical experimental error is a constant fraction of the yield, independent of the energy. In practice, ϵ is computed as the weighted-average fraction of non-statistical deviation for all yield points

$$\epsilon' = \frac{\sum_i \left[\frac{\delta_i^2 - S_i^2}{\bar{y}_i^2} \right] W_i}{\sum_i W_i} \qquad (C.8)$$

where S_i is the RMS (Root-Mean-Squared) average of the statistical errors

at energy E_i,

$$S_i^2 = \sum_{j=1}^{n_i} s_{ij}^2/n_i \quad , \tag{C.9}$$

and the weights W_i are taken to be

$$W_i = (\bar{y}_i/\bar{d}_i)^4 n_i(n_i-1) \tag{C.10}$$

where

$$\bar{\bar{d}}_i = \left[\frac{\epsilon\bar{y}_i^2 + S_i^2}{n_i}\right]^{1/2} = \text{the total error of the average yield } \bar{y}_i \ . \tag{C.11}$$

(The weights are approximately the inverse of the uncertainty in the quantity in brackets in equation C.8.) Because equation C.8 is a function of ϵ through equations C.10 and C.11, it is necessary to solve for ϵ iteratively; on the first iteration ϵ is set = 0 and the d_i are calculated, then equation C.8 can be solved for ϵ which is used to obtain a new set of $\bar{d}_i$ etc. until the solution achieves a constant value. Through equations C.7 and C.11 the expected total error can be obtained for the individual yields y_{ij} and the average yields $\bar{y}_i$.

The quantity ϵ is a convenient measure of the average fraction of experimental error involved in the yield curve measurement and it is also convenient to define the quantity $\bar{\delta}$ which is computed from

$$\bar{\delta}^2 = \frac{\sum_i (\delta_i/\bar{y}_i)^2 W_i}{\sum_i W_i} \tag{C.12}$$

analogously to equation C.8. $\bar{\delta}$ is thus a measure of the fractional error

of the yield curve averaged over all measurements. Referring to equation C.8 it can be seen that the square root of the difference of $\overline{\delta}^2$ and ϵ is the average fraction of statistical error in the yield curve.

CLSR deck

The average yields and errors (defined by equations C.5 and C.11 respectively) are punched in a deck suitable for CLSR input. By appropriate choice of control instructions, the user may obtain separate decks for average yield curves, defined as subsets of the total data set.

Other APU functions

In addition to the basic functions described above, the APU routine provides for a number of listing and display features for the convenience of the user.

Sorted lists A central and essential part of the APU processing involves the sorting of the run data by run number, curve number, time, bombardment energy, etc. The sorting functions are performed via a pointer list, created by a modified Bucharest-sort. The user may request that APU output the data after each stage of sorting, thus providing a convenient table for inspection of the data.

Data correlations The APU routine correlates the yield deviations with several of the experimental parameters. In particular, the deviations are correlated with the sample and house numbers and the experimental time. The user may use the tables of correlations, printed by APU, as a means of eliminating systematic dependencies on these parameters.

Plotting The user may call for plotting of several of the APU computed results. Specifically, the routine currently supports plotting of the yield curves (three options: all yield points, all curve points, and

average yield curve with error bars), plotting of the yield deviations versus time (one plot for each house), and plotting of an error histogram indicating the distribution of yield deviations and a standard Gaussian error distribution. These plots are useful for rapid inspection of the experimental results and as a means of locating runs with large deviations.

REFERENCES

1. E.P. Wigner, Phys. Rev. 51, 106 (1937).

2. J.E. Anderson, C.Wong, J.W. McClure, Phys. Rev. 126, 2170 (1962).

3. E.K. Warburton, in Isobaric Spin in Nuclear Physics, edited by J.D. Fox and D. Robson (Academic Press Inc., New York, 1966), p.90.

4. S. Fallieros, B. Goulard, and R.H. Venter, Phys. Letters 19, 398 (1965).

5. R.E. Segel, in Isobaric Spin in Nuclear Physics, edited by J.D. Fox and D. Robson (Academic Press Inc., New York, 1966), p.194.

6. E. Hayward, Photonuclear Reactions, (Mimeographed lecture notes, University of Melbourne, 1969), p.83.

7. P. Axel, D.M. Drake, S. Whetstone, and S.S. Hanna, Phys. Rev. Letters 19, 1343 (1967).

8. K. Shoda, M. Sugawara, T. Saito, and H. Miyase, Phys. Rev. Letters 23, 800 (1969).

9. S. Costa, F. Ferrero, S. Ferroni, and L. Pasqualini, Nucl. Phys. 72, 158 (1965).

10. B.L. Berman, J.T. Caldwell, R.R. Harvey, M.A. Kelly, R.L. Bramblett, and S.C. Fultz, Phys. Rev. 162, 1098 (1964).

11. R.W. Gellie, Aust. J. Phys. 21, 765 (1968).

12. R. Leonardi and M. Rosa-Clot, Phys. Rev. Letters 23, 874 (1969).

13. J. O'Connell, Phys. Rev. Letters 22, 1314 (1969).

14. H. Verheul, Nuclear Data Sheets for A=62,63, and 64, Nuclear Data, B2-3-1 (1967).

15. J. Jänecke, Nucl. Phys. 73, 97 (1965).

16. L.I. Schiff, Phys. Rev. 83, 252 (1951).

17. H.W. Koch and J.W. Motz, Rev. Mod. Phys. 31,920 (1959).

18. A.S. Penfold and J.E. Leiss, University of Illinois Report, 1959 (unpublished).

19. S.C. Pancholi, K. Way, Nuclear Data Sheets for A=65, Nuclear Data, B2-6-1 (1968).

20. Nuclear Data Sheets, (Printing and Publishing Office, National Academy of Sciences-National Research Council, Washington 25, D.C., 1959), NRC 59-2-23.

21. F. Everling, L.A. Koenig, J.H.E. Mattauch, and A.H. Wapstra, 1960 Nuclear Data Tables, (U.S. Government Printing Office, National Academy of Sciences-National Research Council, Washington 25, D.C., 1961), Part 1.

22. J.E. Griffin and C.L. Hammer, U.S. Atomic Energy Commission Report IS-676, 1963 (unpublished).

23. J.S. Pruitt and S.R. Domen, National Bureau of Standards Monograph 48, 1962.

24. J. Goss, F. Riffle, D. Parsignault, and J.C. Harris, Bull, Am. Phys. Soc. 12, 535 (1967).

25. B.C. Cook, Nucl. Instr. Methods 24, 256 (1963).

26. L. Katz and A.G.W. Cameron, Can. J. Phys. 29, 518 (1951).

27. B.C. Cook, J.E.E. Baglin, J.N. Bradford, and J.E. Griffin, Phys. Rev. 143, 724 (1966).

28. D.W. Anderson, thesis, Iowa State University of Science and Technology, Ames, 1965 (unpublished).

29. D.G. Owen, E.G. Muirhead and B.M. Spicer, Nucl. Phys. A122, 177 (1968).

30. S. Costa, F. Ferrero, C. Manfredotti, L. Pasqualini and G. Piragino, Nuovo Cimento 48, 460 (1967).

31. J.P. Roalsvig, R.N.H. Haslam, and J.L. Bergsteinsson, Can. J. Phys. 38, 320 (1960).

32. L. Katz, H.E. Johns, R.G. Baker, R.N.H. Haslam, and R.A. Douglas, Phys. Rev. 82, 271 (1951).

33. L. Marshall, Phys. Rev. 83, 345 (1951).

34. R. Montalbetti, L. Katz, and J. Goldemberg, Phys. Rev. 91, 659 (1953).

35. B.I. Gavrilov and L.E. Lazareva, J. Exptl, Theoret. Phys. 30, 855 (1956) [English transl.: Soviet Phys.-JETP 3, 871 (1957)].

36. T. Nakamura, K. Takamatsu, K. Fukunaga, M. Yata, and S. Yasumi, J. Phys. Soc. Japan 14, 693 (1959).

37. G.E. Coote, W.E. Turchinetz, and I.F. Wright, Nucl. Phys. 23 468 (1961).

38. D. St. P. Bunbury, Proc. Phys. Soc. 671, 1106 (1954).

39. H. Wäffler and O. Hirzel, Helv. Phys. Acta, 21, 200 (1948).

40. W.H. Hartley, W.E. Stephens, and E.J. Winhold, Phys. Rev. 104, 178 (1956).

41. B.D. McDaniel, R.L. Walker, and M.B. Stearns, Phys. Rev. 80, 807 (1950).

42. R. Sagane, Phys. Rev. 85, 926 (1952).

43. R. Sagane, Phys. Rev. 83, 174 (1951).

44. R. Sagane, Phys. Rev. 84, 586 (1951).

45. A. El Sioufi, P. Erdös, and P. Stoll, Helv. Phys. Acta, 30, 264 (1957).

46. A. Hofmann and P. Stoll, Helv. Phys. Acta, 31, 591 (1958).

47. K. Strauch, Phys. Rev. 81, 973 (1951).

48. L.S. Edwards and F.A. Macmillan, Phys. Rev. 87, 377 (1952).

49. J.R. Van Hise, R.A. Meyer, and J.P. Hummel, Phys. Rev. 139 (1965).

50. B.M. Spicer, Nuovo Cimento (1), 2, Suppl., 243 (1964).

51. R.M. Osokina and B.S. Ratner, J. Exptl. Theoret. Phys. 46, 1157 (1964) [English transl.: Soviet Phys.-JETP 5, 1 (1957)].

52. R. Leonardi and M. Rosa-Clot, Nuovo Cimento 41, 100 (1969).

53. J.S. Levinger, Phys. Rev. 84, 43 (1951).

ACKNOWLEDGEMENTS

I am deeply indebted to many people whose interest, encouragement, suggestions, and participation have made this effort possible. Although a full enumeration of all those who assisted and cooperated in this experiment is not possible, I would like to thank the following people for their contributions: Dr. B. C. Cook, my major professor, whose guidance and suggestions have contributed to the success of this experiment and have been greatly appreciated. Dr. R. C. Morrison, for many hours of fruitful discussion and his interest and unfailing encouragement. Mr. George Holland, who attended to many of the operational details, and who together with Mr. Bill Glass kept the synchrotron operational. Mr. Les Severeide, Mr. Jim Sayre, Mr. Bob Pritchard and the other synchrotron operators, for their careful and conscientious labors. Mr. Ron Johnson, Mr. Jon McCarthy, Mr. Gary Clark, Mr. Harold VanderMolen, Mr. Robert Centner, Mr. Stan Kocimski, and Mr. Wayne Jung who volunteered to assist with the data taking. Mr. George Covert for many useful suggestions in the design of the computer programs. Mr. John Linderblood and the computation center staff, whose cooperation greatly expedited the data analysis. Mrs. Glenda Shearer for her care and patience in typing the thesis.

I particularly wish to thank my wife, Julie, for her patience and encouragement; her labors as breadwinner and wife have sustained us through my graduate program.

I wish to dedicate this effort to my daughter, Pamela, whose impending arrival lent impetus to this work.